Communication Mechanisms in Dynamically Seeded Cumulus Clouds

by
Gad Levy

Department of Atmospheric Science
Colorado State University
Fort Collins, Colorado

Colorado State University

Department of Atmospheric Science

Paper No. 357

COMMUNICATION MECHANISMS IN DYNAMICALLY SEEDED CUMULUS CLOUDS

by

Gad Levy

Research Supported by the

National Science Foundation
Grant No. ATM-8113082

and

National Oceanic and Atmospheric Administration
Contract No. NA81RAH00001

Department of Atmospheric Science

Colorado State University

Fort Collins, Colorado

August, 1982

Atmospheric Science Paper No.

ABSTRACT OF THESIS

COMMUNICATION MECHANISMS IN DYNAMICALLY SEEDED CUMULUS CLOUDS

Twelve clouds are simulated by perturbing FACE 8.25.75 and FACE 8.13.75 field soundings employing the CSU 3-D cloud model. After a cloud similar to the observed one is initiated, experiments are designed to study the reaction of the cloud to certain modifications. Eight such experiments are performed to study the communication mechamisms to the subcloud boundary layer and the dynamic response to seeding, mesoscale flow modification and increased loading. Results reinforced by theoretical scaling arguments show that the hydrostatic pressure communication, the vertical dynamic communication and the pressure buoyancy are present but are secondary to loading, temperature buoyancy, water vapor buoyancy and the horizontal dynamic forces on a single deep convective cloud scale. Dynamic response to seeding is seen, but acts always to reduce rainfall. Mesoscale modification on the cloud scale is very strong. The influence of early weather convection in dry days is crucial to moisten the sounding needed for later deep convection.

Gad Levy
Department of Atmospheric Science
Colorado State University
Fort Collins, CO 80523
Fall, 1982

ACKNOWLEDGEMENTS

I would like to thank Dr. William R. Cotton for his support. I am also grateful to Mr. Greg Tripoli for his invaluable assistance and to Mr. John Cunning and Dr. Wayne H. Schubert for fruitful discussions. The good humored moral support of Dr. Avraham Huss is greatly appreciated. The efforts of Brenda S. Thompson in the preparation of the manuscript, of Judy A. Sorbie in the drafting of the figures and of Julie L. Cotton in typing and preparation of the figures are gratefully acknowledged.

This research was supported by the National Science Foundation Grant No. ATM-8113082 and the National Oceanic and Atmospheric Administration Contract No. NA81RAH00001. Computations were performed at the National Center for Atmospheric Research, which is sponsored by the National Science Foundation.

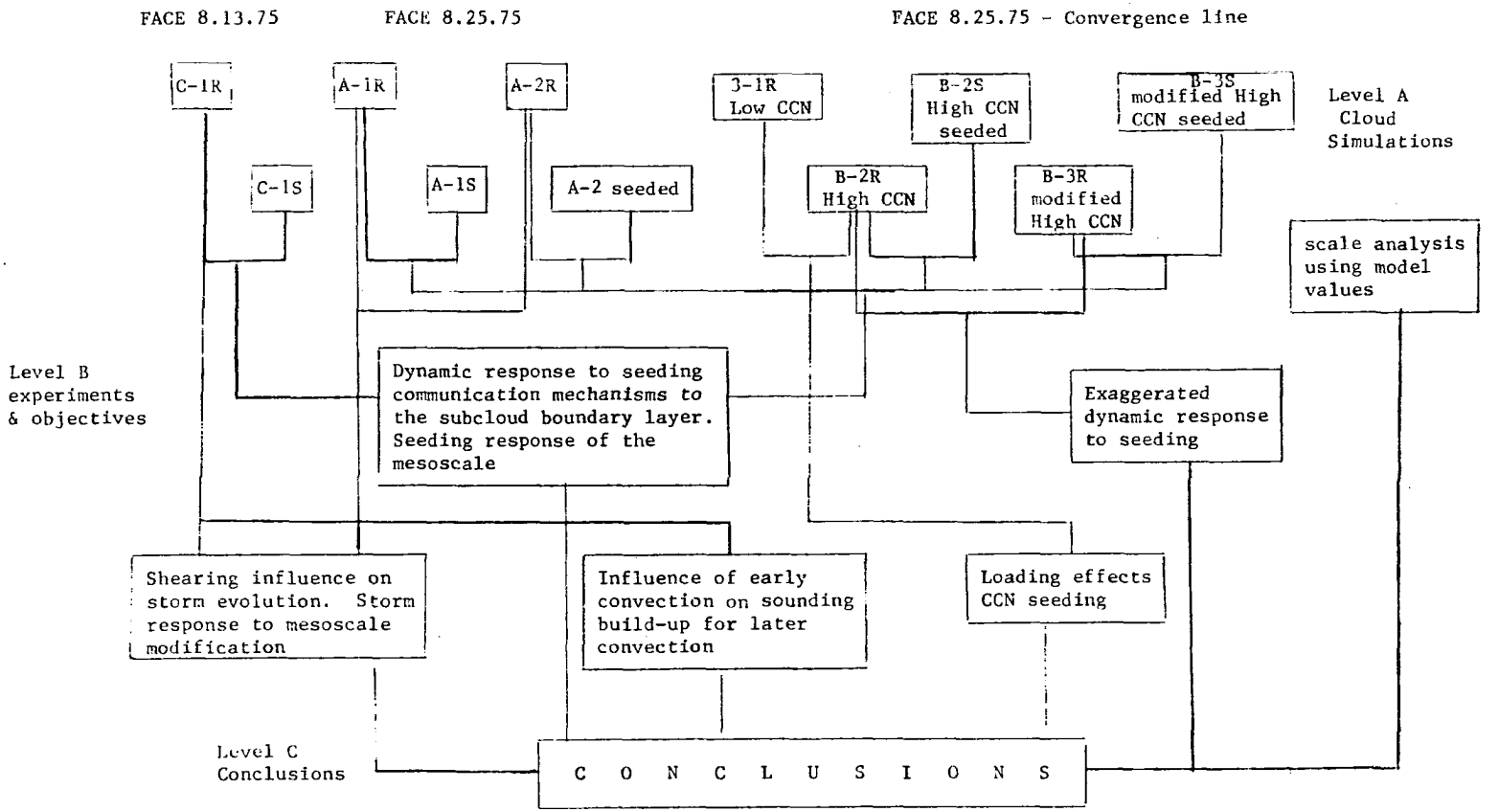

Diagram 1: Thesis flow chart.

TABLE OF CONTENTS

LIST OF FIGURES

The following contouring intervals are used in all figures:

1 P_a (0.1 mb) for isobars

1°C for isotherms

1 ms^{-1} for isotachs

1 g kg^{-1} for mixing ratio isotherms

Triangles represent graupels and circles represent rain water in mixing ratios figures.

Thick lines outline the cloud (where mixing ratios of cloud water and crystal ice exceed 10^{-3} g kg^{-1})

Solid lines are positive perturbations, dashed lines are negative perturbations

LIST OF SYMBOLS

Symbol	Explanation
A	Any time dependent variable
AC	Tendency due to accretion
ADV	Advective operator
CL	Tendency due to collection
CN	Tendency due to conversion
c_p	Specific heat capacity of air at constant pressure
c_v	Specific heat capacity of air at constant volume
F	Any general function
F_Q	Water loading force
FR	Tendency due to freezing
g	Acceleration of gravity
H	Height of the model domain, scale height
L	Horizontal length scale
L_{iv}	Latent heat of fusion
$L_{\ell v}$	Latent heat of condensation
ML	Tendency due to melting
NU	Tendency due to nucleation
p	pressure
p_H	Hydrostatic part of pressure perturbation
p_{drag}	Drag induced pressure perturbation
p_{dyn}	Dynamic part of pressure perturbation

Symbol	
p_o	Basic state pressure
p_{oo}	Reference pressure (100 kPa)
PR	Tendency due to fallout
p_r	Precipitation rate
R_d	Gas constant of dry air
r_c	Mixing ratio of cloud water
r_g	Mixing ratio of graupel
r_i	Mixing ratio of crystal ice
r_{ice}	Mixing ratio of ice water
r_ℓ	Mixing ratio of liquid water
RM	Tendency due to melting
r_r	Mixing ratio of rain water
r_t	Mixing ratio of total water
r_v	Mixing ratio of water vapor
r_w	Mixing ratio of condensate
t	Time
T	Time scale
T_o	Basic state temperature
T_H	Homogeneous nucleation temperature (233 K)
TURB	Turbulence operator
u	X-component of velocity
U_i	i-component of velocity
v	Y-component of velocity
v_T	Terminal velocity of hydrometeor
w	Z-component of velocity

Symbol	
x,y,z	Cartesian coordinates
x_*,y_*,z_*	Transformed coordinates
Z_s	Height of surface
γ	Ratio of c_p/c_v
δ_{i3}	Kronecker's delta
δ	Total hydrostatic part of vertical equation of motion
θ	Potential temperature
θ_e	Equivalent potential temperature
$\theta_{i\ell}$	Ice water potential temperature
θ_v	Virtual potential temperature
ρ_o	Basic state density
ρ_a'	Perturbation dry air density

1.0 INTRODUCTION

While considering the scientific basis for enhancing rainfall from convective clouds, Braham et al. (1957) concluded that:

"There are no clear cut models which would support the contention that cloud treatment will yield an increase in rainfall from clouds that are already precipitating, or that will soon precipitate, as a result of purely natural causes. Nevertheless, there are certain possibilities, which have been suggested, which merit consideration, even though they are not sufficiently well understood to constitute an acceptable physical model. Two ways in which cloud treatment may increase precipitation are, by increasing the precipitation efficiency of the precipitation processes in a cloud already raining, and by changing the scale of magnitude of the cloud system from which precipitation falls through purely natural processes."

The two approaches indicated by Braham et al., were tested experimentally and referred to later as seeding for microphysical effects, or "static seeding" for the first approach, and seeding for dynamic effects, or "dynamic seeding" for the second.

Practically the "static seeding" is aimed to increase precipitation through the formation of hydrometeors with terminal velocities large enough to reach the ground. That can be done by enhancing cold rain processes by applying an optimum concentration of artificial ice nuclei or dry ice to a layer of supercooled water in cold clouds.

It can also be accomplished in warm clouds by seeding with salt solution to enhance warm rain processes. Several orographic and convective cloud seeding experiments based on the "static seeding" concept have been carried out. Among those are the Sierra Project in the west coast of the U.S. (Marwitz et al., 1979), the Climax experiment in the Rocky Mountains (see Grant and Kahan, 1974), and the first and second Israeli Rainfall Enhancement Experiments (see Gagin and Neuman, 1974). Though the concepts behind static and dynamic seeding are different, total separation between the two is practically impossible, as "static seeding" would still result in the release of latent heat, and hence, may have some dynamic effects as was shown in the North Dakota Pilot Project (Dennis et al., 1975). Vice versa, Parungo and Nagamoto, 1982 report that the latent heat can release water vapor from freezing drops, which later recondenses on AgI particles to form more ice crystals by condensation freezing nucleation. They claimed to have inferred this from observations and measurements in the FACE 7.24.80 case study.

The "dynamic seeding" approach, as it was being performed in the Florida Area Cumulus Experiment (FACE) (Woodley and Sax, 1976), rests on the assumption that seeding of actively growing towers will lead to the conversion of supercooled liquid water to ice and subsequent "explosive growth" due to the latent heat release. The accelerated growth of rising towers is then hypotehsized to lead to strengthened low-level flow, subcloud layer convergence and possibly even merger of neighboring clouds. It is still an unresolved question how or if the buoyancy aloft is communicated to the subcloud layer. A better understanding of the dynamic response to seeding is essential

in determining the effectiveness, feasibility and optimal procedures in convective cloud seeding operations.

This study employs the CSU Three Dimensional cloud model in a series of numerical experiments. The experiments are designed in an attempt to verify theories for the cloud response to seeding, to verify conclusions from past simulations (Nehrkorn, 1981) and to explore the response of clouds to seeding under different shear regimes as well as to check other possible mechanisms and concepts. In the experiments, seeding is parameterized by introducing extra ice nuclei at the seeding level.

The first set of experiments is focused on the response of a cloud that was actually seeded on 25 August 1975 as a part of the FACE program. This cloud is the subject of observational study employing Doppler radar and surface mesonet data (Cunning et al., 1979). This cloud was simulated previously (Nehrkorn, 1981). A set of simulations (experiments A-1R, A-1S, A-2R and A-2S) is run to investigate the dynamic response of a cumulus cloud to seeding (A-1R vs. A-1S, A-2R vs. A-2S) and at different shear regimes (A-1 vs. A-2). This series of experiments reveals also the dominant role of precipitation in communication to the subcloud pressure field. This mechanism, which at least in our simulations is overwhelmingly important, seems to have been ignored in the past in most theories.

In an attempt to delay the premature warm rain that tends to obscure subcloud pressure lows by creating early mesohighs in the boundary layer below the cloud, the Cloud Condensation Nuclei (hereafter referred to as CCN) number concentration was raised from 300 to 1000 cm^{-3} in the second and third sets of experiments. As reported by Sax and

Hudson (1981) this CCN number concentration is very realistic in South Florida summer clouds and measurements taken during FACE in 1975 and 1976 show a similar order of magnitude of CCN. The second and third sets of experiments initiate the cloud by a perturbation somewhere along the convergence line depicted by the surface mesonet at the simulated time. The sensitivity of the model clouds to varying CCN raises the question whether or not clouds can be modified by CCN seeding with or without subsequent IN* seeding. This question is addressed in view of the results.

The third set of experiments addressing the same above mentioned problems is designed as another case study and attempts to simulate the actual natural cloud observed at FACE on 13 August 1975 and its response to seeding. This cloud was observed and surface mesonet data, Doppler radar data and time lapse are available. The day was chosen for a case study as a one dimensional model run showed a great potential for seeding (large difference in height between the seeded and non-seeded clouds, termed as "dynamic seedability"). August 13, 1975 was a "non seeding day" and seeding is only simulated, but no observations of response to seeding exist.

Diagram 1 shows a flow chart of the different simulations, experiments and objectives.

---

* IN - Ice Nuclei

2.0 BACKGROUND AND LITERATURE SURVEY

The first experiments employing the dynamic seeding concept were performed in Australia by Kraus and Squires (1947). During the 1960's more experiments were performed in the Caribbean in 1963 and 1965 (Simpson et al., 1965 , 1967). Isolated, oceanic cumulus clouds were seeded with silver iodide. The silver iodide was released by aircraft in the form of pyrotechnics, released in actively growing towers as they reach the $-10^{o}C$ level (see Woodley and Sax, 1976). A statistically significant increase in cloud top height compared to a control sample was inferred from the study. These changes in cloud height were also predicted by a one dimensional cloud model which was used as part of the experiment and evaluation scheme. Another effect of seeding which was not expected was a substantial lateral growth following seeding. This finding, as well as those of Davis and Hosler (1967), raised the possibility of increasing rainfall through seeding and led to the "single cloud" experiments in 1968 and 1970 over South Florida and to the Florida Area Cumulus Experiment (FACE). Cotton (1972) in one dimensional modelling studies, noticed sensitivity of model clouds to the presence of supercooled rain and to warm rain processes. Sax and Hudson (1981) measured the CCN concentration over the FACE area during the summers of 1975 and 1976. They found the CCN concentration to be highly variable as a function of the time of day and the prevailing surface wind. Concentrations ranged from 250 cm^{-3} (typical to

modified maritime aerosol) to 2500 cm^{-3} (typical to continental aerosols). They offered the explanation that air masses with long continental trajectories would have "well aged" continental aerosols while those air masses with long maritime trajectories prior to brief continental exposures would have "fresh" continental aerosol spectrum. It appears from these data that localized sources are strongly influencing the character of South Florida summer CCN aerosols. The exact nature of the causes of such localized effects is not known at this time. However, Sax and Hudson speculate that different crops are responsible for the local changes. As warm rain processes are highly dependent on the nature of the aerosols and the CCN concentrations, further investigation of the problem is needed. Takahashi (1981) simulated a Hawaiian warm cloud with a three dimensional anelastic cloud model with detailed microphysics. In his simulation a change of 35% in CCN concentration (increase from 100 cm^{-3} to 135 cm^{-3}) delayed the warm rain processes, but the general profiles of both the dynamics and microphysics remained the same.

The hypothesized chain of physical and dynamic responses to seeding is summarized in Table 1. Simpson (1980) hypothesized that downdrafts are the dominant means of communication between seeded cloud towers and events near and below cloud base. Cunning and DeMaria (1981), pointed out that another mechanism, the hydrostatic and non-hydrostatic pressure response within the boundary layer to developing convection ahead, may be equally as important as the downdraft mechanism. A modified summary of the dynamic seeding hypothesized chain, which includes the role of downdrafts and pressure response in the boundary layer is described in Table 2.

Table 1. Summary of dynamic seeding hypothesis chain

1) Silver iodide is introduced at approximately the -10°C level in the cumulus clouds, i.e., in a region where there is believed to be a significant amount of supercooled liquid water.

2) This seeding results in conversion of water to ice, with resultant release of latent heat of fusion (~80 cal g^{-1}), producing increased buoyancy. Additional buoyancy is believed to be produced by depositional heating (~680 cal g^{-1}) associated with the deposition of water vapor directly onto ice crystals, resulting from the fact that the saturation vapor of ice is less than that of water.

3) This buoyancy produces an increase in the updraft, which is transferred all the way down to the bottom of the cloud.

4) This produces an increase in the inflow of moist air into the bottom of the cloud.

5) This increased inflow of moisture eventually results in more rainfall.

6) By appropriate seeding, neighboring clouds can be caused to merge.

7) The increased size of the merged cloud systems results in increased total rainfall.

The communication mechanisms in the dynamic seeding conceptual chain (tables 1,2) are still unclear. Though one dimensional cumulus models have been useful in identifying suitable conditions for dynamic seeding and in understanding and predicting the early stages of cloud response, they give very little insight in the missing links in the conceptual chain leading from vertical tower growth to a larger, longer lived cloud producing more rain at the ground. Woodley and Sax (1976) formulated the question of how the enhanced buoyancy at seeding level is "communicated" all the way down to cloud base to increase the inflow of subcloud air so that seeded clouds process more water. Three major mechanisms are proposed: 1) A subcloud layer pressure fall caused by accelerated tower growth, enhancing low level convergence at early stages following seeding; 2) Downdrafts formed and enhanced by midlevel inflow of potentially cool air due

Table 2. Modified summary of dynamic seeding hypothesis chain

Stage I: Initial growth

1) Rapid glaciation of the updraft regions of supercooled convective towers by silver iodide pyrotechnic seeding.

2) Invigoration of the updrafts through the release of latent heats of fusion and deposition, the latter occurring as the cloud air approaches saturation relative to ice.

3) Enhanced tower growth is associated with a pressure fall below cloud, resulting in low-level inflow. At about the same time strengthened dynamic entrainment (Simpson, 1976) into the cloud occurs just below the invigorated rising tower. The increased inflow of drier air increases evaporation of the liquid water falling from the rising seeded tower, which in turn accelerates and strengthens downdraft processes. This combination of events comprises the initial stage of explosive cloud growth.

Stage II: Enhanced downdrafts and secondary growth(duration 30-50 min)

4) Enhanced downdrafts below the invigorated seeded tower as the precipitation and the evaporatively cooled air entrained into the tower moves downward. This results in convergence at the interface between the downdraft and the ambient flow, in the growth of secondary towers (which in turn might be seeded) and in the expansion of the cloud system. This is the second stage of explosive cloud growth.

The second stage of explosion involves gust front forcing of new growth and major explosion on the downshear flank. Location of main expansion/new tower growth may differ depending on the wind profile.

Stage III: Interaction with neighboring clouds

5) Seeding of secondary towers in the parent cloud results in their growth, followed by expansion and intensification of the downdraft area which then moves outward to interact with outflows from neighboring clouds (which also might have been seeded). With the proper ambient conditions, carefully timed seeding might encourage merger by capitalizing on the tendency of two cumulinimbus in different life cycle stages to approach each other.

6) Accelerated/increased merging, together with larger merged systems, increases the mesoscale convergence, resulting in new cloud growth available for seeding.

Stage IV: Increased area rainfall

7) Augmented and more efficient processing of the available moisture from the larger, more organized seeded cloud systems results in increased rainfall.

8) Increased rainfall over the entire target (assuming the absence of compensatory rainfall decreases in the unseeded portions of the target).

to the vertical mass flux divergence beneath the invigorated tower at later stages of cloud development; and 3) Precipitation enhanced by seeding can inhibit or enhance subsequent cloud development creating a meso-high at the subcloud layer to force or inhibit convergence depending on the inflow regime. Theoretical, observational and simulated evidence concerning the above mentioned mechanisms will be discussed.

2.1 Pressure

Surface pressure measurements associated with cumulus storms were taken in the mesonetwork of the National Hail Research Experiment (NHRE) by Foote and Frankhauser (1973) in the National Severe Storms Laboratory (NSSL, OK) by Barnes (1978), Lemon (1976) and others, and in FACE by Cunning and DeMaria (1981).

These studies show existence of meso-lows associated with warm converging air and meso-highs associated with cold diverging outflow air. Cunning and DeMaria carried out observations on the case study day of 25 Aug. 1975 (Sets A and B) and found that as the convective system was in the rapid development stage, prior to the occurrence of downdrafts, the surface pressure decreased below the convection by 0.35 kPa which increased the boundary layer inflow by 8.2×10^{-4} s^{-1} (120%) (see fig. 2.1). Lemon found a correlation between the pressure deficit and the convergence (Fig. 2.2). Barnes (1970) analyzed a radiosonde ascent within an updraft of a tornadic storm. He inferred a negative perturbation below 1.5 km and positive above that level and derived hydrostatically the vertical pressure perturbation field.

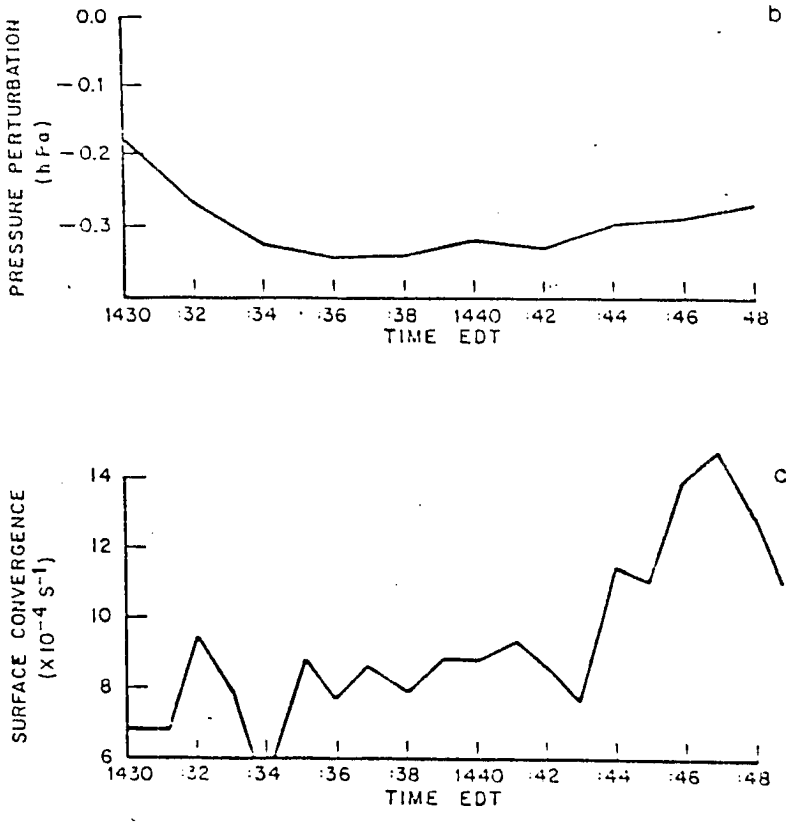

Figure 2.1: Pressure perturbation and convergence on 8.25.75 FACE. (from Cunning and DeMaria, 1981)

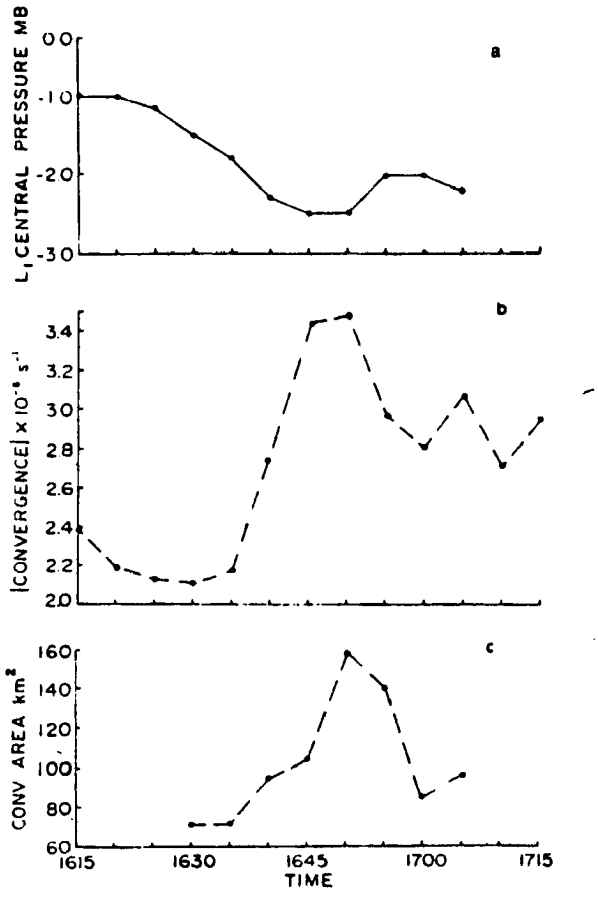

Figure 2.2: Time variations of objectively analyzed surface values of minimum pressure of mesolow L_1, maximum convergence associated with L_1 and planimeter-determined areal coverage within -1.5×10^{-3} s^{-1} convergence contour. From Lemon (1976).

The pressure change beneath a convective storm is described by Byers (1974) as follows: "Early in the cumulus stage a fall in surface pressure almost invariably occurs. This fall is observed before a radar echo forms, and is recorded over an area several times the maximum horizontal extent of the echo. When the radar echo appears, the pressure trace levels off in the region directly underneath it, but continues to fall, frequently at a more rapid rate, in the surrounding areas. The pressure drops in the cumulus stage are usually small in magnitudes - less than 0.7 mb below the diurnal change of the particular time of day - and take place over a period of 5 to 15 min. Following the fall, the pressure trace remains steady for as long as 30 min..."

The pressure falls appear to be caused by the combined effects of vertically accelerated air motions, the expansion of the air due to the release of the latent heat of condensation and the failure of the convergence near the surface to compensate fully for the expansion or divergence aloft. Later, in the mature stage, the displacement of the warmer air by the cold outflowing air from the downdrafts results in a pressure rise initiating a meso-high. An abrupt rise of pressure occurs at the region of the main rain and downdraft just after they have first reached the earth at the beginning of the mature stage. It is superimposed upon or may mark the start of the meso-high. The meso-high persists through the dissipating stage of the cell, after which the pressure returns to the trend prevailing before the passage of the storm. The rate and total amount of pressure rise depend on the slope of the cold air mass, the temperature difference between the cold air and the displaced warm air, the depth of the cold

air itself and the speed with which the system travels. The most marked pressure changes are found near the cell core and they decrease with distance from it.

Wilhelmson and Ogura (1972) decomposed the total pressure perturbation into three components. These components may be termed as dynamic (associated with advection and diffusion of momentum), hydrostatic (associated with thermal buoyancy) and drag induced (associated with the weight of liquid water). Consider the vertical equation of motion for cloud convection neglecting the coriolis force:

$$\frac{dW}{dt} = \delta - g r_\ell + F_z \tag{2.1}$$

where: $$\delta = \frac{1}{\rho} \frac{\partial p}{\partial z} - g \tag{2.2}$$

second and third right hand side terms of (2.1) denote the liquid water drag force and vertical component of friction respectively. Decompose now density and pressure into a hydrostatic base state (ρ_o, p_o) and a perturbation component (p', ρ') $p = p_o + p'$; $\rho = \rho_o + \rho'$:

$$\frac{\partial p_o}{\partial z} = -g\rho_o \tag{2.3}$$

and assume $|p'| << p_o$ $|\rho'| << \rho_o$

to get: $$\delta = -\frac{1}{\rho_o} \frac{\partial p'}{\partial z} - g \frac{\rho'}{\rho_o} \tag{2.4}$$

(see Holton 2.28 p. 40 for detailed derivation)

first term on the right hand side of (2.4) is the perturbed vertical pressure gradient force. Second term is gravitational buoyancy.

By perturbing the equation of state

$$p = \rho R_d T(1 + 0.61\, q_v) \tag{2.5}$$

and Poisson's formula for potential temperature

$$\theta = T \left(\frac{p_{oo}}{p}\right)^{Rd/cp} \qquad p_{oo} = 1000 \text{ mb} \tag{2.6}$$

about a base state (see Dutton and Fichtl , 1969) ρ' is eliminated from the buoyancy term yielding the breakdown:

$$-g \frac{\rho'}{\rho_o} = g \left(\frac{\theta'}{\theta_o} + .61\, r_v'\right) - g \frac{p'}{\gamma p_o} \tag{2.7}$$

On the right hand side of (2.7) the first term is the moist thermal buoyancy whereby an air parcel is lifted if it is warmer or more moist than it's surroundings. The second term, which shows that an air parcel is also accelerated upward if it is at lower pressure than it's surroundings, is the "pressure buoyancy". Schlesinger (1980) performed a pressure breakdown for a three dimensional anelastic numerical simulation. He used a nondimensional pressure variable decomposed into three components, i.e.

$$p = p_H + p_{drag} + p_{dyn}$$

Weighing the importance of each component in different stages of cloud life cycle, Schlesinger concluded that:

i) In the developing stage both the hydrostatic and dynamic components are important contributors to the pressure deficit in the lower 6 km.

ii) The pressure excess near the cloud top in the developing stage is mainly hydrostatic due to cooling of overlying air which is rising dry adiabatically.

iii) The drag induced pressure component acts in opposition to the hydrostatic part and in the developing stage is also rather less important.

iv) In the mature stage the shallow low level meso-high under the cloud is partly hydrostatic resulting from cooling of moist downdraft air. Both the dynamic and drag induced components also contribute greatly to the meso-high and displace its center.

v) In the mature stage all three components are of comparable importance.

vi) The hydrostatic and drag induced components are mainly responsible for the vertical perturbation pressure gradients, whereas, the dynamic component dominates the horizontal pressure gradients namely a high at the upshear side and a low at the downshear side.

A horizontal pressure distribution as in (vi) was also reported by Cotton and Tripoli (1978) and Tripoli and Cotton (1980).

2.2 Downdrafts

The mature stage of a thunderstorm is characterized by the existence of both updrafts and downdrafts at least in the lower half of the cell (Byers). The weight and drag of precipitation helps to change the updraft into a downdraft which, once started can continue without this frictional drive, maintained by evaporational cooling as a consequence of the entrainment of dry environmental air. Down-

drafts can lead to the decay of the cloud as well as, in some cases, to the formation of a sustained, long lived system. Downdrafts originate at midlevels and at high rates of entrainment can either use up all the water or deprive the updraft of its buoyancy.

Browning (1964) developed a conceptual model of a severe right moving storm in a sheared environment with veering winds. He proposed a system of up and downdrafts in which the updraft is fed from low level air ahead of the storm. At the interface between the outflow region of the downdraft and the inflow air, enhanced convergence forces inflow air up and into the updraft. Kropfli and Miller (1976) analyzed a hailstorm in its decaying stage over northeastern Colorado by multiple Doppler radar data. They found that the updraft was fed by potentially warm air from ahead of the storm, and that the source of air for the downdraft is potentially cool air at midlevels in a somewhat different structure. In storms described by Browning and Ludlam (1962) and by Brandes (1977) downdrafts were also found to originate in midlevels regardless of the prevailing flow field. Tropical cumulunimbi and squall lines show the same results (Betts, 1978; Zipser, 1969). A three dimensional simulation by Miller (1978) showed draft structure similar to that proposed by Browning with the downdraft outflow sustaining the storm through its interaction with the low level flow. Schlesinger (1980) performed trajectory analysis of his simulation and concluded that the upper part of the downdraft is fed by midlevel air whereas the lower part is fed by low level air originating in front of the storm. Tripoli and Cotton (1980) found in a series of simulations with a three dimentional cloud model that an initially strong updraft and a more pronounced meso-

low acted to diverge a large fraction of the outflow toward the low pressure region under the main updraft. "The resultant convergence below the primary updraft further reinforced the updraft circulation." In a two-cylinder model of cumulus cells, Yau (1980) concluded that strong entrainment has been demonstrated to be a major dissipative process and condensation (evaporation) is a major heat source (sink). Takahashi (1981) simulated a shallow warm Hawaiian cloud with a three dimensional anelastic cloud model with periodic boundary condition. He found that downdrafts at the downshear side carry westward momentum downward and move the cloud more quickly to the west. The clouds move westward due to transport of low level momentum by the updraft. Downdrafts in this simulation acted to erode the cloud.

Yau and Rejéan (1982) used a three dimensional anelastic model with periodic lateral boundary condition to simulate a cumulus ensemble in Canada. They found cases where small clouds were "dried" by downdrafts of neighboring large clouds and cases in which under favorable conditions downdrafts of two neighboring clouds diverge on approaching the ground and generate a convergence flow in the region between them that can generate a new cloud.

2.3 Rainfall

The role of rainfall in initiating the downdraft was mentioned and indeed Byers, in describing the mature stage of a thunderstorm says "The beginning of the rain at the surface and the initial appearance of the downdraft there are nearly simultaneous". However, rain can appear at the subcloud layer prior to the appearance of the downdraft and create a meso-high by evaporative cooling. At later stages when downdrafts and precipitation coexist at the surface,

separation between effects caused by precipitation, and those caused by the 'dry downdraft' is very difficult. Nevertheless, Yau (1980), in a 3 dimensional numerical experiment isolated the different effect of precipitation in the circulation dynamics by setting the drag force of cloud and rain water to zero. He concluded that the drag of the hydrometeors, no doubt, exerts a non-negligible effect, but evaporative cooling appears to play a more dominant role, at least in a moderate size cumulus. Murray and Koenig (1972) demonstrated the mechanism of evaporation in affecting cloud growth in an axisymmetric model with the same results. Delaying the warm rain processes (by increasing CCN number concentration for example), can carry more water to freezing level and avail more water to the cold rain and ice phase processes and hence to cause stronger dynamic effects as was shown in modelling studies by Cotton (1972). On the other hand, as was shown by Takahashi (1981) in a three-dimensional experiment it increases the water loading and weakens the updraft. If one assumes that cloud and precipitation droplets are falling at nearly their terminal velocity, then the net drag force on a parcel of air due to the presence of condensate is approximately equal to the total weight of the condensed water distribution. The vertical equation of motion for air containing suspended condensate must then be modified by the additional forcing term

$$F_Q = -gr_w$$

where r_w is the mixing ratio of total condensate. This term modifies the buoyancy term in the equation of motion. One consequence of the precipitation process is to unload the updraft. As a result, a tower could penetrate to greater heights when precipitating (Simpson, et al., 1965; Simpson and Wigget, 1969; Weinstein and Davis, 1968). Das (1964), Takeda (1965, 1966) and Srivastava (1967) demonstrated that the water which is removed from the upper parts of the rising tower can accumulate at lower levels and lead to the decay of the convective cell. Rain falling at the subcloud layer, can introduce evaporative cooling at that layer and cause a meso-high.

2.4 The Seeding

Joanne Simpson (1980) postulated downdrafts as a primary linkage between dynamically seeded invigorated cloud towers and those events near and below cloud base which cause enhanced inflow, new tower growth leading to cloud expansion and frequent merger with neighboring clouds. She suggests three mechanisms by which seeding leads to intensified penetrative downdrafts following the initial updraft invigoration: (1) dynamical invigoration of the vertical internal circulation in the rising tower (Levine, 1959); (2) much increased loading of precipitation particles in downdrafts adjacent to and between updrafts which continuously augment their negative buoyancy by evaporation (Malkus, 1955), which is enhanced by the increased dynamic entrainment beneath the rising tower; and (3) pressure forces arising from the rapid warming and rise of the seeded tower and also at low levels from the gust front. The complete chain of

dynamic seeding is described in Table 2. Cunning and DeMaria (1981) recorded pressure falling under a rapid developing tower, prior to the occurrence of downdrafts at the surface. They concluded that the pressure fall is a communication mechanism as important as the downdraft. Simpson and Cooper (1981) argue, however, that the direct cause of the explosive growth of the cloud studied was the downdraft outflow convergence produced by a preexisting cloud to the west and the pressure fall associated with rapid cloud growth could have augmented the pre-existing convergence, but had a secondary role in the explosive growth.

Numerous one dimensional models were employed to simulate and predict results of cumulus seeding (e.g. see Simpson and Wiggert, 1969 and Cotton, 1974). Many of them successfully predict the height change due to seeding ("seedability") and are used operationally as a decision making tool for field programs.

Orville's two dimensional model has been used to simulate effects of seeding with dry ice (Kopp, et al., 1979) and silver iodide (Hsie, 1978; Chen, 1981). Hsie demonstrated the importance of the location of the AgI release for an optimal distribution within the cloud. Chen tried to isolate different seeding effects and concluded that the microphysical processes and the way they are parameterized have great effects on the dynamics of the cloud. He also concluded that the latent heat release effect on cloud development following seeding is secondary to condensate loading. Downdrafts and secondary circulations played an important role in the formation and inhibition of subsequent towers and in the reduction of overall precipitation by 35% due to seeding.

Koenig and Murray (1976) used an axi-symmetric two-dimensional model to test effects of continuous heavy artificial seeding. Their seeded run resulted in diminishing rain water, stronger updrafts and weaker downdrafts. As a consequence precipitation was decreased in the seeded case. They concluded, however, that even in the case of an active ice multiplication process, massive sudden seeding may result in dynamical changes. Fritch and Chappell (1979) simulated seeding with a three-dimensional mesoscale model. They modeled the seeding by assuming that every tower reaching the $-10^{o}C$ level was seeded. Their results show the importance of moist downdrafts to the evolution of the mesoscale systems. Due to the coarse resolution (20 km grid spacing), however, cumuli are parameterized and no cloud scale features are resolved.

An early set of experiments using the CSU 3D cloud model (Cotton et al., 1980) showed an unrealistically vigorous response to seeding because ice phase tendencies were large enough to delete liquid water mixing ratios in excess of the amount available to them. A repeat of these experiments with a revised ice phase parameterization and a correction for large microphysical tendency run by Nehrkorn (1980) yielded a seeding response of a realistic magnitude. An additional 1.5 g kg^{-1} of liquid water was frozen due to seeding, resulting in a warming of about $0.5^{o}C$. Maximum updraft speeds in the seeded towers were between 2 ms^{-1} and 4.3 ms^{-1} higher in the seeded towers than in the untreated cases. The buoyancy enhancement aloft was not communicated to the surface. Pressure falls due to seeding were small and confined to heights above cloud base, while downdrafts, although invigorated by up to 3.9 ms^{-1}, did not penetrate the surface because of

the decelerating influence of adiabatic warming. The precipitation from the seeded towers was increased by up to 14%, but because the intensification of seeded towers inhibited the development of subsequent cells, the overall precipitation from the cloud was decreased by seeding. Figure 2.3 illustrates the precipitation response to seeding in Nehrkorn's experiments.

The above response to seeding in terms of mass and temperature fields, precipitation, buoyancy and vertical velocities was concluded by Nehrkorn in his thesis. The pressure response was very slight at and below the seeding level, but not observable at all below cloud base. The intensification of downdrafts below cloud base was not observable as well. Hence, the subcloud communication mechanisms associated with seeding were not clearly identified. Therefore it is the intent of this study to concentrate on those communication mechanisms.

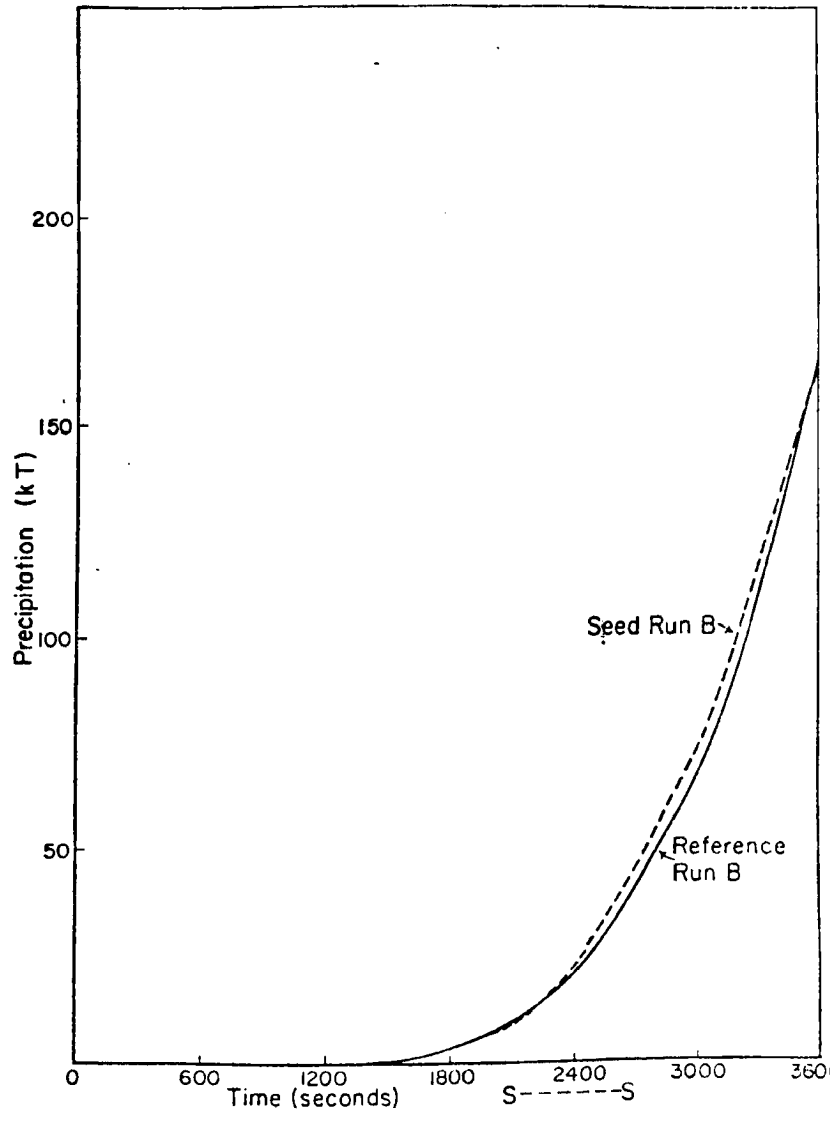

Figure 2.3: Time evolution of precipitation for seed and reference run B. From Nehrkorn (1981).

3.0 DESCRIPTION OF THE MODEL

The three-dimensional cumulus convection model employed in this study is a revised version of the model described in Tripoli and Cotton (1980). The revised version is described in full detail in Tripoli and Cotton (1982) and Cotton et al. (1982). A brief summary of the equations is given in the Appendix. In the following, only the major features of the model will be described qualitatively.

3.1 The System of Equations

The Colorado State University multidimensional cloud model described by Tripoli and Cotton (1980) has undergone a basic reformulation to accommodate the addition of an ice phase parameterization and experimentation with higher-order turbulence closure schemes. The equations of motion remain essentially the same. However, density is perturbed from a dry basic state. Instead of specifying a pressure tendency equation as done previously, separate dry air and moisture continuity equations are invoked. Cloud water has been changed from a predictive variable to part of a diagnostic set which also includes temperature, potential temperature and perturbation pressure. The specification of latent heating tendencies are avoided by using ice-liquid water potential temperature as the thermodynamic variable. As demonstrated by Tripoli and Cotton (1981), θ_{il} remains unchanged in the presence of all water phase changes. The reference state is assumed to be hydrostatic, dry and to obey the ideal gas law.

Total water is divided into vapor (r_v), liquid ($\bar{r}_\ell$) and ice water ($\bar{r}_{ice}$). As with the model of Tripoli and Cotton (1980), liquid water is assumed to consist of cloud droplets having a mixing ratio r_c and raindrops having a mixing ratio r_r. Cloud droplets are assumed to have negligible terminal velocity and evaporate and condense instantaneously maintaining zero supersaturation. The cloud droplet distribution is not specified, yet they are assumed to exist in concentrations which are constant and characteristic of the environment modeled. Raindrops, having a mixing ratio r_r, on the other hand, are much larger and are assumed to exist in a Marshall-Palmer distribution with a constant slope.

The mixing ratio of cloud droplets is initially converted to raindrops by a parameterization of cloud droplet collection described by Tripoli and Cotton (1980). Once formed, raindrops can accrete cloud droplets, evaporate, precipitate or interact with ice particles.

The ice-phase is partitioned into ice crystals having mixing ratio $\bar{r}_i$, and graupel or frozen raindrops having mixing ratio $\bar{r}_g$. Ice crystals are considered pristine individual crystals which are not highly rimed. They are initiated from a specified concentration of activated ice nuclei which are assumed to occur naturally or by seeding. Graupel particles, on the other hand, are highly rimed ice crystals that have lost their crystalline identity, or are frozen raindrops. They are much larger and have particle densities as high as 0.9 g cm^{-3}. As graupel mixing ratios increase, the assumed mass of individual graupel particles may reach a large enough size to be considered hail. The ice phase parameterization also provides an average terminal fall velocity for both ice crystals and graupel. Unlike raindrops, graupel particles are assumed to have a variable particle density and the

distribution slope varies. Hence, fall rates change considerably with ice mixing ratio.

The ice parameterization predicts the changes in ice crystal mixing ratio $\bar{r}_i$ by vapor deposition and riming growth of ice crystals, as well as melting. The parameterization also predicts the changes in graupel mixing ratio ($\bar{r}_g$) due to vapor deposition, conversion of ice crystals into graupel, riming growth of graupel, supercooled raindrops collecting ice crystals and freezing, graupel particles collecting supercooled raindrops, melting of graupel, and precipitation. A schematic representation of the microphysical parameterization is given in Fig. 3.1

3.2 Numerical Integration Scheme

a. Time differencing scheme

The time differencing scheme used is similar to that reported by Klemp and Wilhelmson (1978) and Cotton and Tripoli (1978). The acoustic fluctuating terms are integrated on a short timestep while a leapfrog marching scheme is performed with the other terms on the large timestep. The short timestep marching scheme is the same as that described by Tripoli and Cotton (1980), except perturbation dry air density replaces perturbation pressure.

b. Finite space differencing and averaging

The model variables are defined on a spaced-staggered grid with variable spacing in both the horizontal and vertical directions as described by Cotton and Tripoli (1978). In this system, all scalar variables are placed at the midpoint of each grid volume. Velocity components are defined on the faces of the volume perpendicular to the

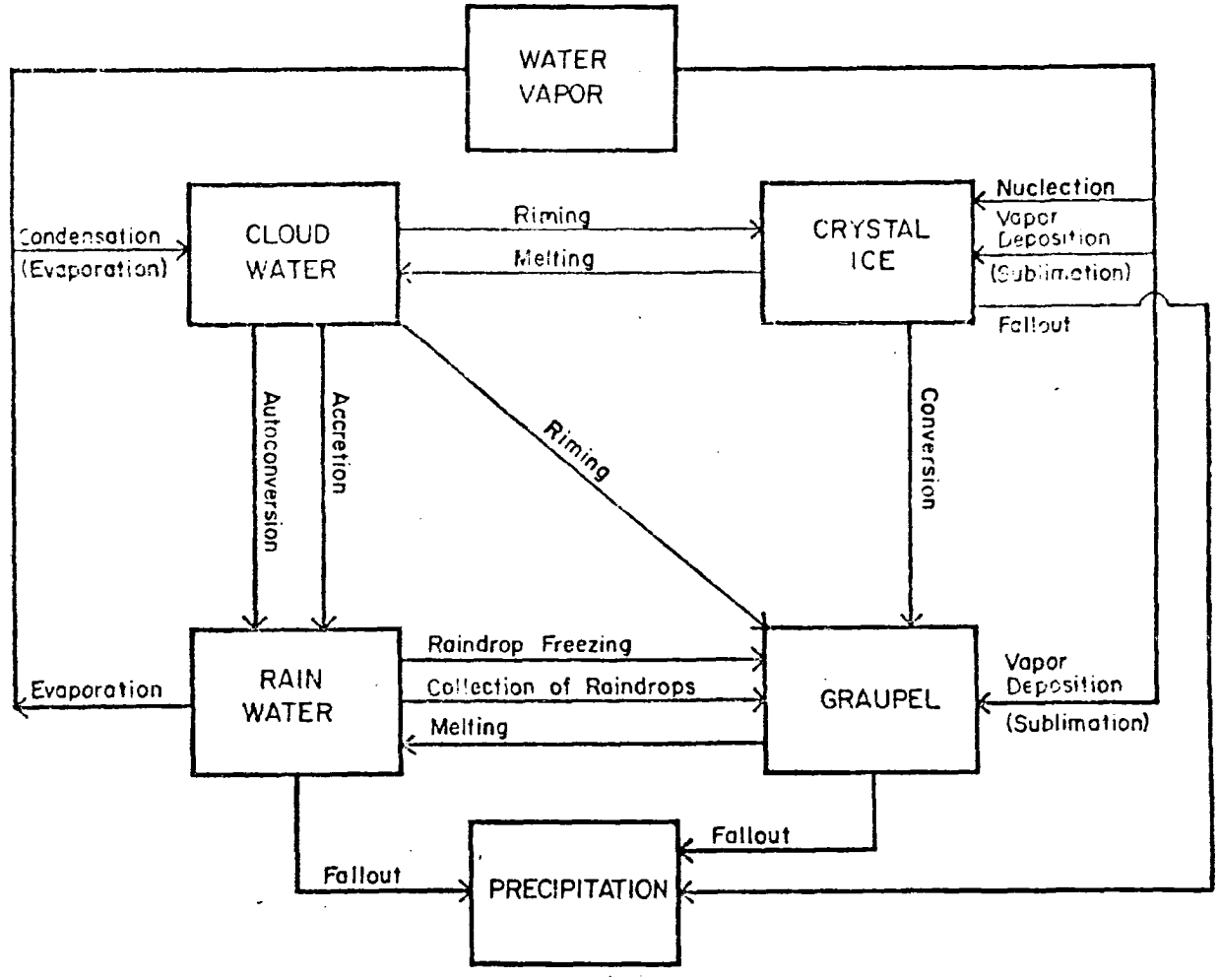

Figure 3.1: Diagram of microphysical processes. Arrows denote direction of mass transfer. Parentheses denote negative rates. Adapted from Stephens (1979).

component direction. The model may be integrated both two-dimensionally and three-dimensionally. In the two-dimensional case, an x* by z* coordinate system is used in which all variations in the y direction are neglected. The grid resolution is chosen according to the features needed to be resolved and the time step is then adjusted to keep computational stability.

Second-order space differencing similar to that of the box method (see Kurihara and Holloway, 1964) is used to calculate all derivatives.

c. Numerical adjustment procedures

Because of truncation error associated with the finite differencing, negative values of positive definite quantities will be produced. In addition, growth rates calculated by microphysical parameterizations may actually deplete quantities in excess of the amounts available over a single time step. In order to preserve the integrity of the solution, some numerical adjustment procedures must be performed.

Such an adjustment procedure must be performed to prevent microphysical tendencies from over-depleting water mixing ratio quantities. This adjustment can be made directly to the microphysical tendencies because interrelationships with neighboring grid points are not involved. The procedure is to simply add up the microphysical sources and calculate the amount of mixing ratio available over a given time step. The microphysical sinks are compared to the amount available and if they exceed it, the tendencies are adjusted on a equal percentage basis in order to adjust the mixing ratio to exactly zero after each timestep. The adjustment procedure is repeated interatively because a sink for one adjusted mixing ratio quantity may be a source term for another.

Over depletion of mixing ratio quantities due to numerical errors encountered when the advective and corrected tendencies are combined and adjusted after a prediction is made. The procedure is to raise predicted negative mixing ratios to zero by borrowing from other available water quantities at the same grid point. A decision of what quantity to borrow from is made by attempting to first preserve total water mixing ratio and second to preserve water phase. If these conditions cannot be met, they are sacrificed in reverse order until mixing ratios can be maintained.

3.3 Boundary Conditions

a. Spatial boundary conditions

The lateral boundary conditions used by Tripoli and Cotton (1980) were developed by Orlanski (1976). These boundary conditions are applied to the advective terms of all variables and all terms in the horizontal equation of motion. They may be considered open boundary conditions which allow gravity waves of a specified phase speed to pass freely out of the domain. Wave forms having phase speeds differing from this given phase speed will be partially reflected in varying degrees, depending on how much the phase speed differs from that specified.

In order to control the mean mass field in an acoustic model in a physically realistic manner, the lateral boundary condition should attempt to simulate the response of the extra domain-scale environment to the mean pressure fluctuations within the domain. Therefore, the concept of a mesoscale compensation region (MCR), was introduced (see Tripoli and Cotton, 1982). The MCR keeps track of mass leaving and

entering the domain at each vertical level. Compensating lateral and vertical motion will occur in the MCR which will, in turn, feed back on the simulation domain.

As a result, waves propagating out of the simulation domain are allowed to pass into the MCR. Within the MCR, in turn, the mass can be redistributed under the constraint that the flow is unaffected outside the MCR. For instance, a cloud within the simulation domain may form an anvil outflow into the upper MCR in one region. Compensating subsidence and accompanying drying will then occur in the MCR, perhaps lowering the moisture content of inflow into the domain at lower levels.

The vertical boundary condition on the advective terms is an acoustic radiative upper boundary condition which allows hydrostatic adjustment to occur across the upper boundary and waves to propagate out similar to that discussed by Klemp and Wilhelmson (1978).

The lateral and top boundary conditions on the turbulence are the specification of zero turbulent flux across the boundary. At the bottom boundary, a modified version of the Manton and Cotton (1977) surface layer parameterization is employed to calculate $\overline{w''^2}$, $\overline{w''\theta''_{il}}$, $\overline{w''u''}$, $\overline{w''v''}$ and $\overline{w''r_v''}$, while turbulent fluxes of condensate are set to zero. The modification to the Manton and Cotton (1977) parameterization involves the specification of surface layer lapse rates. In the previous use of the surface layer theory reported by Tripoli and Cotton (1978), temperature and moisture at the surface were initially specified and subsequently held constant. In this application, the lapse rate of θ_v and r_v are specified from the initial field and subsequently held constant. Also, when condensate of any type adding

up to greater than 0.01 g kg^{-1} is found in the grid column, the surface layer lapse rate of θ_v and r_v are set to zero. Thus it is assumed that cloud cover will block the solar heating instantaneously. The angle of incidence of the sun as well as any time lag of the heating response has been neglected.

b. Temporal boundary conditions - initialization

The model initialization consists of (1) the specification of all variables by a horizontally homogeneous initial field and (2) the inclusion of some horizontal variability designed to initiate a cloud circulation or simulate observed environmental vertical or horizontal circulations. In this section, the first step in initialization is described. The second initialization step, however, is dependent on the individual experimental design.

The horizontally homogeneous initial fields are specified from soundings observed in the vicinity of the cloud system under investigation. The initial field of each variable should represent a sampling of the environment in a region unperturbed by the active convection, yet be as near in space and time to the observed convection as possible. Since such soundings are rarely available to the modeler, a composite sounding based upon a number of observations and subjective smoothing is most often used to specify the initial field.

The dry basic state is derived directly from the initial field.

The horizontally homogeneous, initial horizontal wind is given directly from the observed profile. A Galilean transformation may be performed where a mean value or specified value of the horizontal wind is removed in order to keep the cloud system centered in the domain. This transformation must then be considered in the surface layer para-

meterization where the absolute magnitude of the wind relative to the earth becomes important. If topography is considered, the Galilean transformation may not be used.

The initial vertical profiles of $\overline{T}^s$, $\overline{r}_v^s$, and $\overline{u}_i^s$, described at Z levels where $z_s = 0$, are derived from sounding values observed at various pressure levels using a spline fitting technique described in Tripoli and Cotton (1980). This profile is then linearly interpolated to z^* levels throughout the model with given values of z_s. The remaining quantities of P_o, $\overline{\rho_o}$, $\overline{\theta}^s$, $\overline{\theta}_{il}^s$, $\overline{\rho}_a^s$, $\overline{r}_T^s$ and condensate are then calculated at these z^* levels.

In the second step of the initilization procedure, the initial horizontally homogeneous state is varied to reflect observed environmental variations or to perturb the environment in order to initiate a cloud circulation.

4.0 WEATHER CONDITIONS AND EXPERIMENTAL DESIGN

Two sets of experiments are based on observations and soundings taken in South Florida on 25 August 1975. The third set is based on observations taken in South Florida on 13 August 1975. All observations were taken as part of FACE.

4.1 Weather Conditions on 25 August 1975

On that day, the Florida peninsula was under the influence of a subtropical high, with small pressure gradients throughout the troposphere and light and variable winds at the surface. Clear skies in the early morning hours and the absence of any frontal disturbances set the stage for a typical sea breeze day over Florida. Aside from an area of fog between Tampa and Orlando, which existed from 1130 GMT (0730 EDT) to approximately 1300 GMT, the clouds over south Florida were of a purely convective nature. A line of convection could be seen as early as 1300 GMT along the east coast of the peninsula. As time progressed, this line moved inland and extended westward while skies cleared up on a thin strip along the east coast south of Cape Canaveral. Around 1800 GMT, the first intense storms began to form along the sea breeze convergence line. The largest system formed in the Everglades area and moved southwestward. In its dissipating stage, it produced an arc-cloud extending to the north and northeast. Several cells formed to the northwest of Lake Okeechobee and moved northwestward. One dimensional model predicted seedability of 100-300 m for that day.

4.2 Weather Conditions on 13 August 1975

On August 13 the prevailing synoptic scale features were characterized by a well-defined east-west 500 mb trough in south Georgia moving southward, and the displacement southward of the sub-tropical high running from east Cuba northeast to the Azores. A continental high over north Georgia with a surface trough in south Georgia and off the east coast was also evident. In south Florida and over the FACE target area there was a trend of increasing convective instability after four suppressed days, with increasing moisture in the vertical though soundings were still rather dry. Positive vorticity advection and convective instability in central and south Florida were also evident. Widespread and quite intense convection with a well-defined growth in a west coast sea breeze line started at 1900 Z. Satellite data showed a strong west coast line building up at 1930 Z. By 2030 Z a weaker east coast line dissipated into a cirrus deck. After 2030 activity along the west coast moved into the central target area. (See map of target area on Fig. 4.1.) At the observation site (point A in Fig. 4.1) puffy cumuli with some alto-cumulus patches were observed between 1430 Z and 1600 Z. Some distant cumulunimbi could also be seen. Starting at 1600 Z cumulus developed mainly to the east and east-southeast of the observation site, and a large cumulonimbus complex grew larger. By 1700 Z the cumulonimbus complexes were visible along the east shore of the lake with light rain starting 20 minutes later just north of the Field Observation Site (FOS). By 1800 Z the raining cloud died and a new raining cloud was observed on the south side of the lake clearing (ESE of FOS) dying by 1830 Z. At 2030 Z a developing line of cumulunimbi extended from northeast

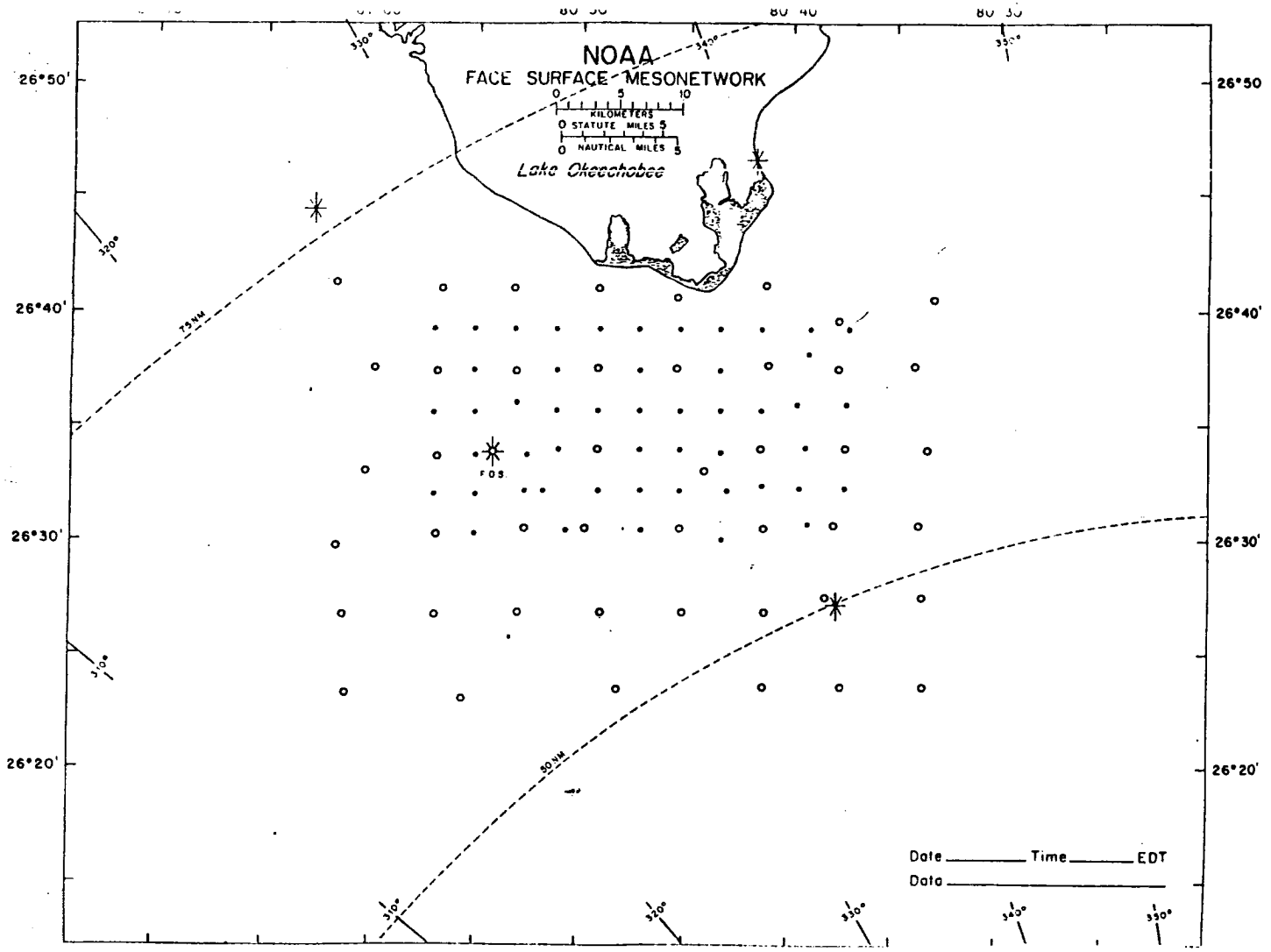

Fig. 4.1: FACE experiment area map: F.O.S. - special sounding site

to southwest with tundershowers dissipating by 2100. New cumuluminbi were seen SE to S to SW of the FOS at that time one dimensional model predicted high seedability of 5 km for a narrow range of clouds (1000 m radius cloud).

4.3 Design of the Numerical Experiments

The experiments are designed as sets of runs in which the first is a reference run and the following runs are identical to the reference run except that a change is introduced representing modification of some physical process (such as seeding with IN, change in CCN or alternating the shear regime). A description of the initialization procedure is given for each set.

The optimal seedable cloud is a marginal cloud that penetrates to the supercooled levels, but yet stays marginal without further growth and intense ice phase processes. It is extremely difficult to initiate such a cloud as the perturbation often needed to start and maintain the cloud is strong enough to carry it into the vigorous ice phase stages.

4.3.1 Set A: Aug. 25 - Alternate shear regime (exp. A-1, A-2)

This set is designed to look more closely at the communication mechanisms. The pressure response in Nehrkorn's simulations was extremely weak and never communicated to the subcloud layer. Downdrafts in his simulations lost all of their momentum near the surface. The first part of this set of experiments (A-1) is an extension of Nehrkorn's experiments. The second part (A-2), is designed to look at all the above mentioned mechanisms, and, in addition to examine the role of the shear regime on the cloud life cycle.

a. Run A-1R:

The model was initiated with a horizontally uniform temperature and moisture sounding. The base state sounding used is the

special sounding taken at the FACE observation mesonet at 1745 GMT. A "smoothing" was applied to values that were a result of disturbance (cloud layer). Above 30 kPa the sounding was matched with the National Weather Service 1200 GMT Miami sounding, resulting in the sounding shown in Fig. 4.2. A strong conditionally unstable layer from the surface to 70 kPa is capped by a slight conditionally unstable layer between 70 kPa and 35 kPa. Above 35 kPa a weak stable layer is present and above 20 kPa strong stability indicates the tropopause. The moisture is fairly low for Florida. The corresponding profile of the equivalent potential temperature (θ_e) shows a minimum at a height of 5 km.

The wind profile chosen for initialization consists of theodolite measured winds from the 1745 GMT special sounding from the surface to 85 kPa, and the 1200 GMT Miami rawinsonde data above that level. A low level mean wind of u = 5.8 ms^{-1} v = -.17 ms^{-1} is removed to prevent the cloud from advecting out of the domain, resulting in a model input wind profile shown in Fig. 4.3. The cloud is started by imposing large scale convergence matched to the measured surface convergence in the form of mean vertical velocity as given in Table 3.

Table 3: Initial mean vertical motion

z	w (cm s^{-1})
0	0
.75	9.36
1.5	13.13
2.25	10.71
3.00	5.65
3.75	2.0
4.5	0

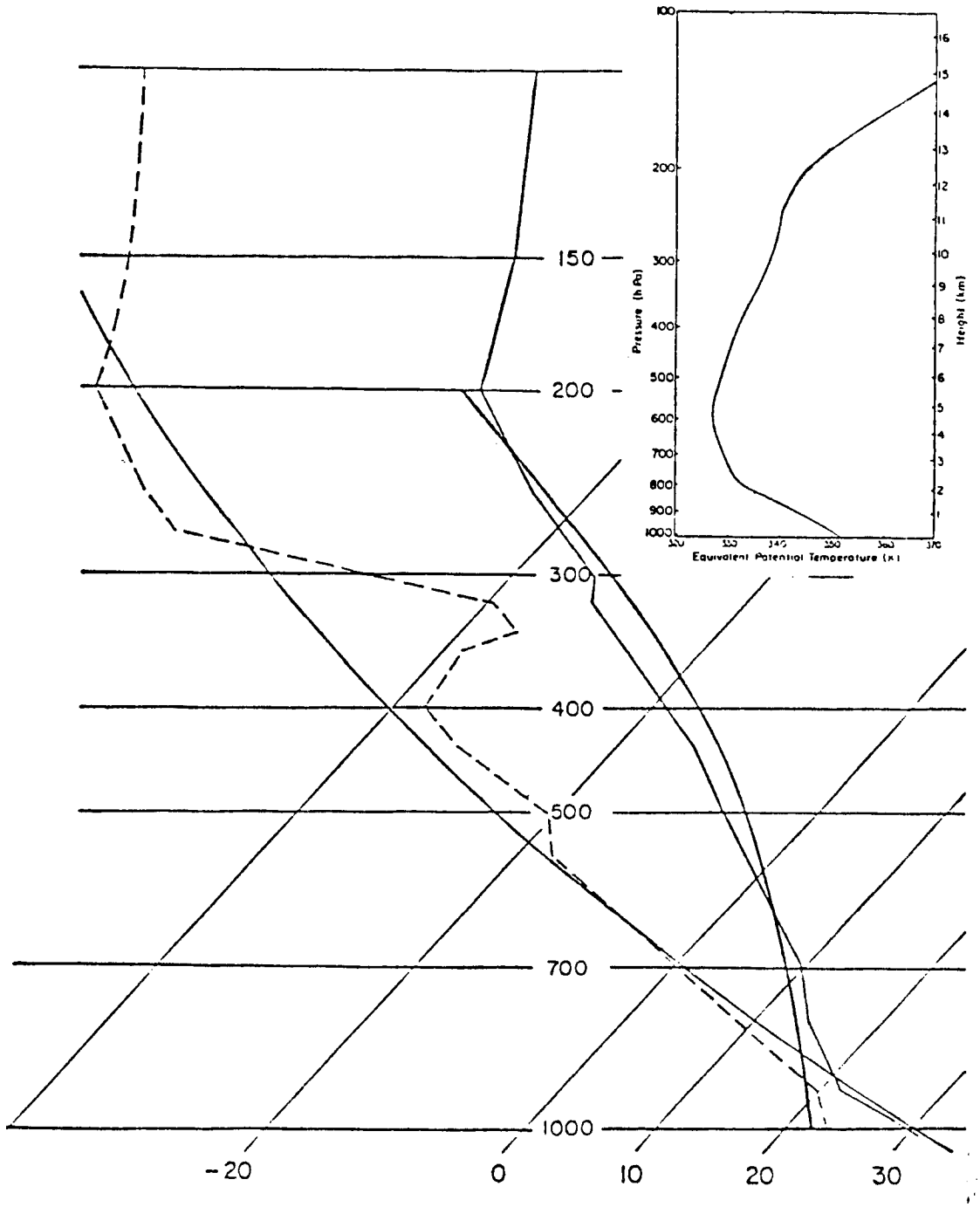

Fig. 4.2: Composite sounding used to initialize the model. Also shown are the 30°C dry adiabat and the 70°C moist adiabat. Insert: Profile of Equivalent Potential Temperature.

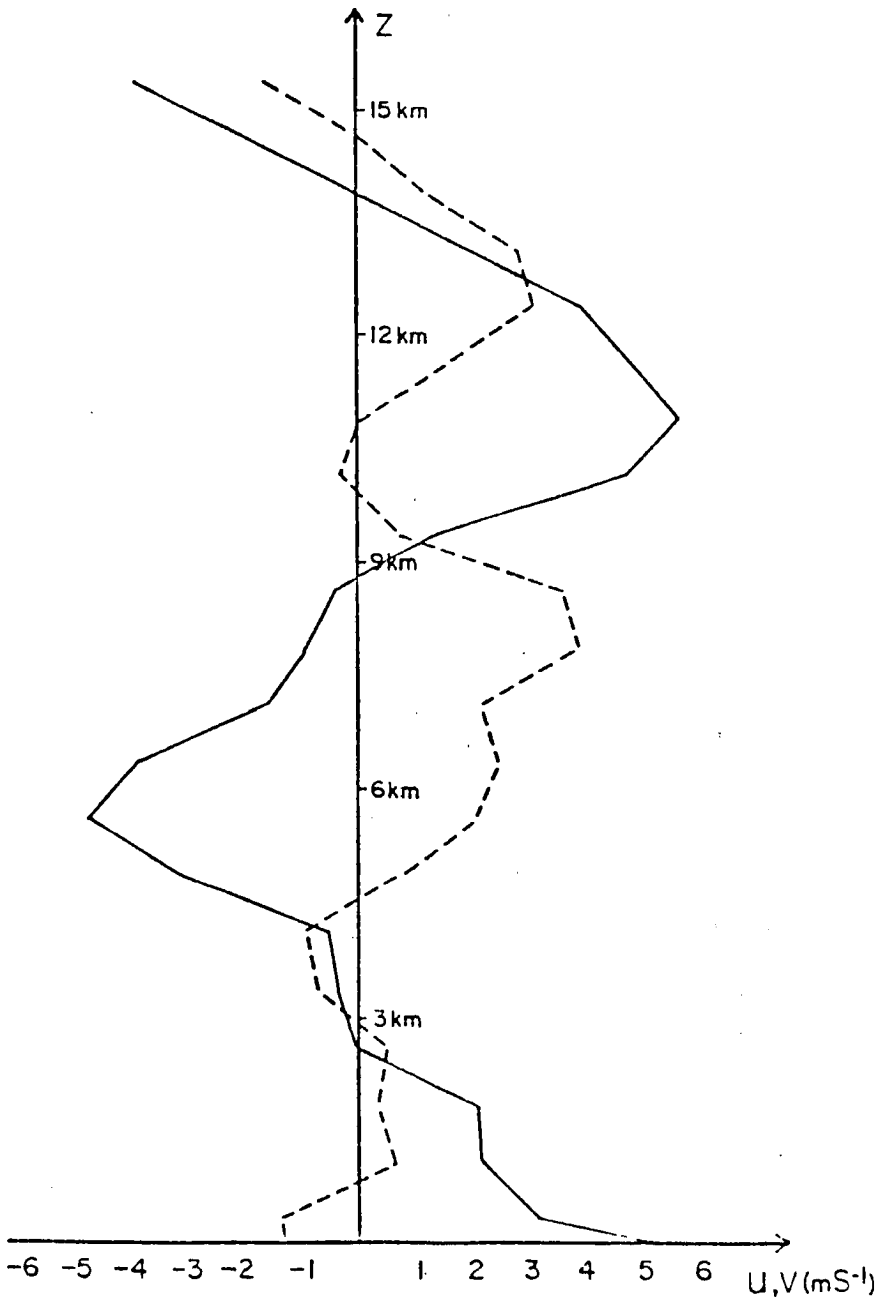

Fig. 4.3: Composite wind profile used to initialize the model. The solid line is the u-component of the horizontal wind, the dashed line the v-component.

Thirty percent of this convergence is imposed as a disturbance on a radius of 2.25 km (corresponding to a peak vertical velocity of 4 ms^{-1} at a height of 1.5 km). A moist initial perturbation is also imposed. The perturbation is selected from preliminary runs to give a seedable cloud that does not dissipate before the seeding level is reached.

b. Runs A-1S:

The seeded case is identical to run A-1R except that from 900 sec until 1500 sec seeding is simulated by setting the IN concentration equal to 100 ℓ^{-1} for two vertical grid points (at z = 5.6 km and z = 6.4 km corresponding to temperatures $-6^{o}C$ and $-10^{o}C$, respectively) and for a horizontal area of six grid points (0.8 km $\leq$ x $\leq$ +0.8 km, 0 km $\leq$ y $\leq$ +0.8 km). In addition a time step of 5 s was used starting at 900 s.

c. Run A-2R:

The reference is identical to run A-1R except that the low level flow is altered from westerly flow to easterly flow at the lowest three levels. The low level flow is given in Table 4. The change results in a mean flow of u = -6.5 ms^{-1} that is removed to keep the cloud in the domain. This is done to test the hypothesis that precipitation falling at the relative inflow flank of the cloud inhibits any new development on that flank. Whereas, precipitation falling at the opposite side could force convergence where downdraft outflow and relative inflow meet.

d. Run A-2S:

This run is identical to run A-2R except that seeding was introduced as in run A-1S. The objective is to test the role of downdrafts and precipitation converging with the inflow in communicating seeding and their influence on subsequent towers' evolution.

Table 4: Initial low level flow

z (km)	3-1 u(ms^{-1})	3-6 u (ms^{-1})
0	5.8	-3.1
0.75	2.5	-1.1
1.5	0	0.2
u mean:	-5.8	-6.5

4.3.2 Set B: Aug. 25 - Convergence line - The CCN seeding

This set is designed to test the importance of the loading effect on cloud growth versus the gain in potential energy due to the delay in warm rain. An exaggerated seeding experiment is done and communication mechanisms and seeding response are tested in precipitating and non-precipitating clouds.

a. Initialization of the reference run B-1R:

The model is initialized with the same moisture composite soundings as described in section 4.3.1. The surface mesonet data show a line of convergence oriented southwest to northeast to the south of Lake Okeechobee (see Fig. 4.4). The wind profile used to initialize this run is the one used for Set A-1. However, it it rotated anticyclonically by 45^{o} resulting in a wind profile as illustrated in Fig. 4.5. After the rotation, an east-west oriented convergence line is imposed on the model. Employing the anelastic form of the continuity equation for shallow convection, the large scale convergence is computed according to the transformed wind profile. Table 5 shows the mean vertical velocity. Preliminary runs and smoothing were

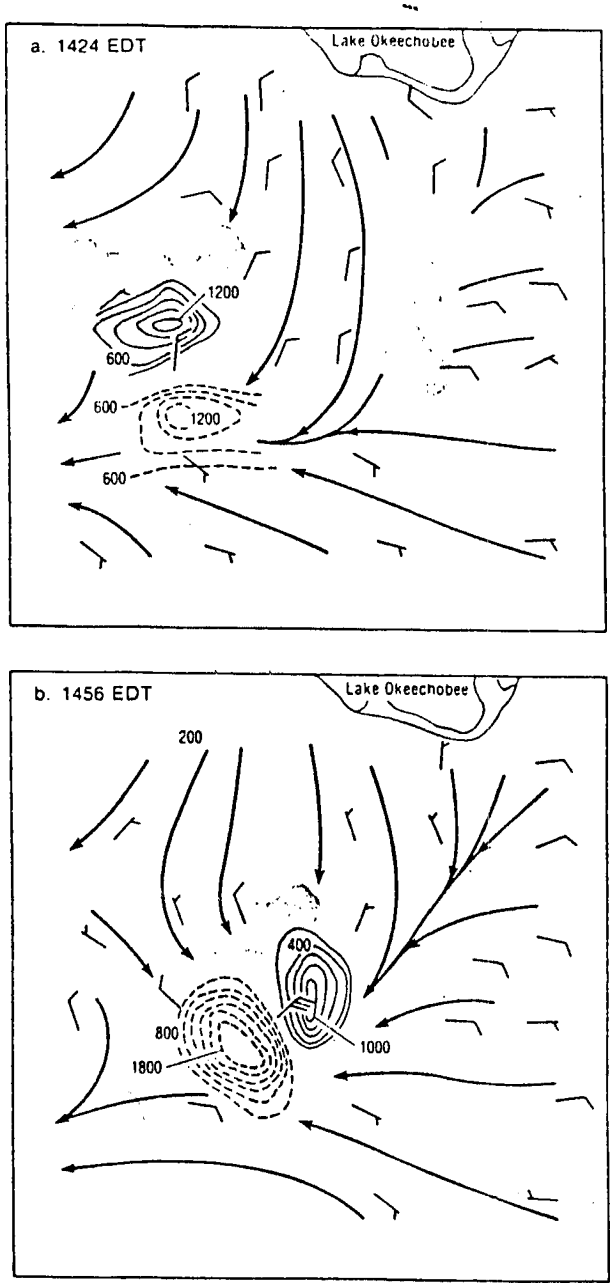

Figure 4.4: Meso net streamlines and convergence analysis on 25 Aug 1975 at FACE area (From Cunning and DeMaria, 1982).

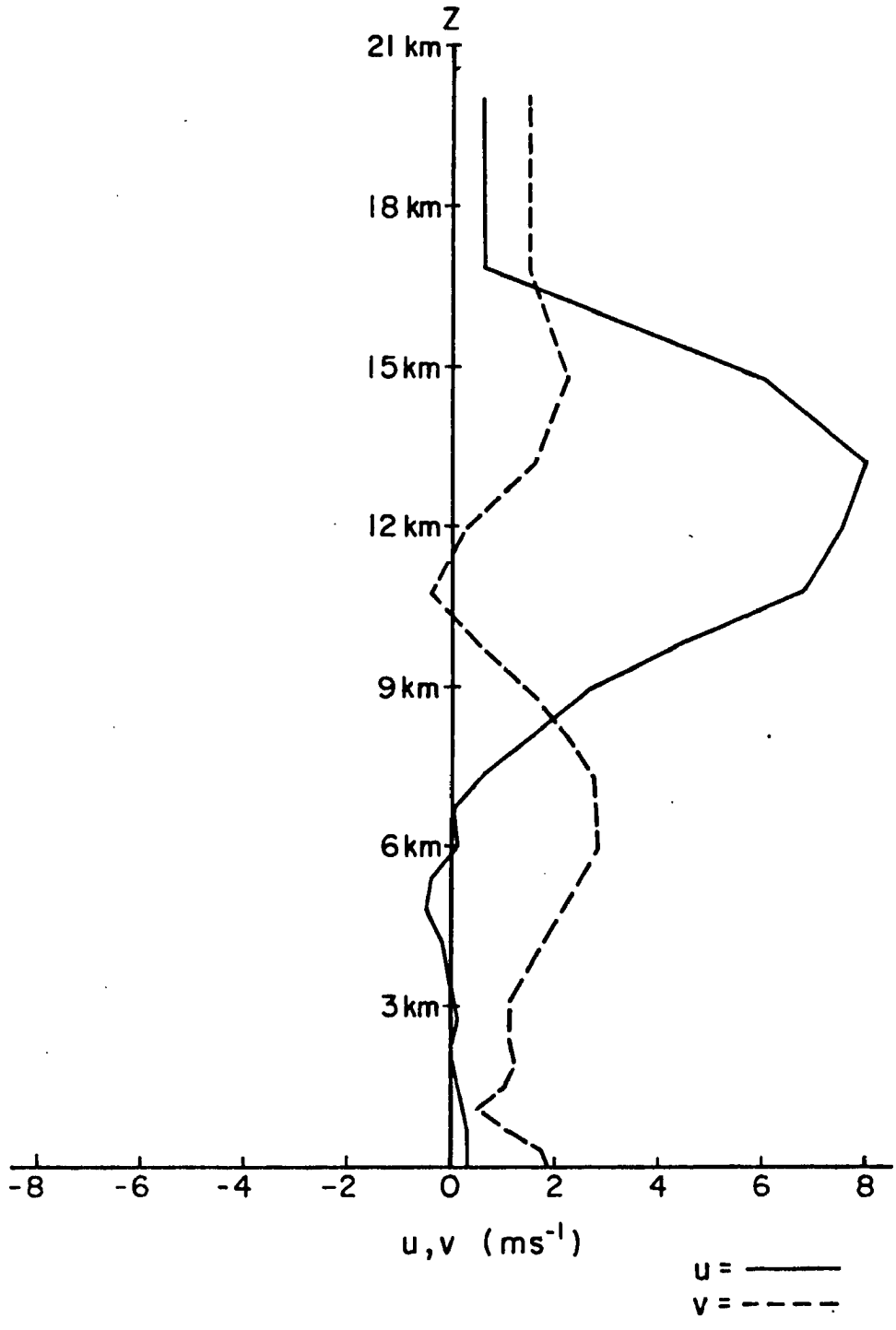

Figure 4.5: Wind profile used to initialize set B.

Table 5: Initial mean vertical motion

z (km)	w (cm s^{-1})
0	0
.359	4.2
.728	5.6
1.109	5.1
1.503	4.2
1.913	2.8
2.339	1.4
2.784	.3
3.25	0

done in order to reproduce the wind profile at the place the soundings were taken (FOS) as a result of the convergence line. The perturbation is imposed by focusing 50% of the mean convergence on a radius of 2.25 km. A low level mean wind of u = -5.2 ms^{-1}, v = 1.9 ms^{-1} is removed to keep the cloud centered. The critical cloud droplet radius for autoconversion of cloud to rain droplets is increased to 14 μm in an attempt to delay warm rain. The horizontal grid spacing is 750 m and the vertical is 40 mb. To test the ice phase role the run is repeated with no ice.

b. The enhanced CCN run B-2R:

This run is identical to the reference run (B-1R) except that the number concentration of CCN is raised from 300 ℓ^{-1} to 1000 ℓ^{-1} in an attempt to delay warm rain that produced a meso high in Set A. It is also expected to carry more moisture to higher levels (above melting level) and thus to make more condensate available for

IN seeding. Measurements by Sax et al. (1981) indicate that concentrations of 1000 ℓ^{-1} are quite common in inland sites of the Florida peninsula.

c. The IN seeding run B-2S:

This run is identical to the high CCN run except that starting at 3600 secs seeding is simulated by setting the IN concentration equal to 100 ℓ^{-1} for three vertical grid points (at z = 6.624 km, z = 7.320 km, and z = 8.071 km) and for a horizontal area of 20 grid points (0 km $\leq$ x $\leq$ 3 km, - 4.5 km $\leq$ y $\leq$ -1.5 km)

d. The modified high CCN run B-3S:

This run is identical to the CCN seeded run except that the cloud to rain autoconversion threshold is zero above the -10^{o}C. This was done in order to initiate rain water at higher levels of the cloud and test the dynamic repsonse to seeding in the presence of rain water. The cloud is identical to run B-2R until it reaches the -10^{o}C level (at 3600 sec). This cloud was seeded with IN (100 ℓ^{-1}) between 3600 sec and 4200 sec at three vertical grid points (z = 6.624 km, z = 7.32 km, and z = 8.071 km) and on horizontal area extending over -.8 km < x < 3.7 km and -4.5 km $\leq$ y $\leq$ -1.5 km.

4.3.3 Set C: Aug. 13 - Convergence line

This set of experiments is designed to confirm previous results with a different case study as well as to study the role of early convection and mesoscale modification on cloud's evolution. One dimensional model predictions showed high seedability for a narrow range of clouds.

a. Initialization of the reference run C-1R:

The model was initialized with a horizontally uniform temperature and moisture sounding. The base state sounding used is the special

sounding taken at the FACE observation mesonet at 2025 GMT. The sounding is shown in Fig. 4.6. A conditionally unstable layer exists from 85 kPa to the tropopause (18 kPa). The moisture is low for Florida. A nearly saturated layer (1^{o}C dew point temperature depression) is introduced between 88.7 kPa and 66.6 kPa. This layer represents the effects of a preexisting mesoscale cloud deck that was observed. Without that moist layer the model generated only non-precipitating fair weather cumuli, which started dissipating at about 20 minutes. The wind profile chosen for initialization consists of the 2025 GMT special sounding taken at the field site from the surface to 45 kPa, and the 1200 GMT Miami rawinsonde data above that level. The surface mesonet data show a line of convergence oriented southwest to northeast south of Lake Okeechobee. The winds were rotated by 45^{o} resulting in a wind profile as drafted in Fig. 4.7. After the rotation an east-west convergence line is imposed on the model. The large scale convergence is computed according to the transformed wind profile employing the anelastic form of the continuity equation for shallow convection, in a way that the winds at the sounding site are reproduced by the model. Table 6 shows the resultant domain averaged vertical velocity.

A perturbation is imposed by focusing 100% of the mean convergence on a radius of 2.25 km. A low level mean wind of $u = -4.8$ ms^{-1}, $v = 1.6$ ms^{-1} is removed to keep the cloud centered. The horizontal grid spacing is 500 m and the vertical is 40 mb. A time step of 5 sec is used. The cloud is initialized in an environment containing 1000 cm^{-3} activated CCN.

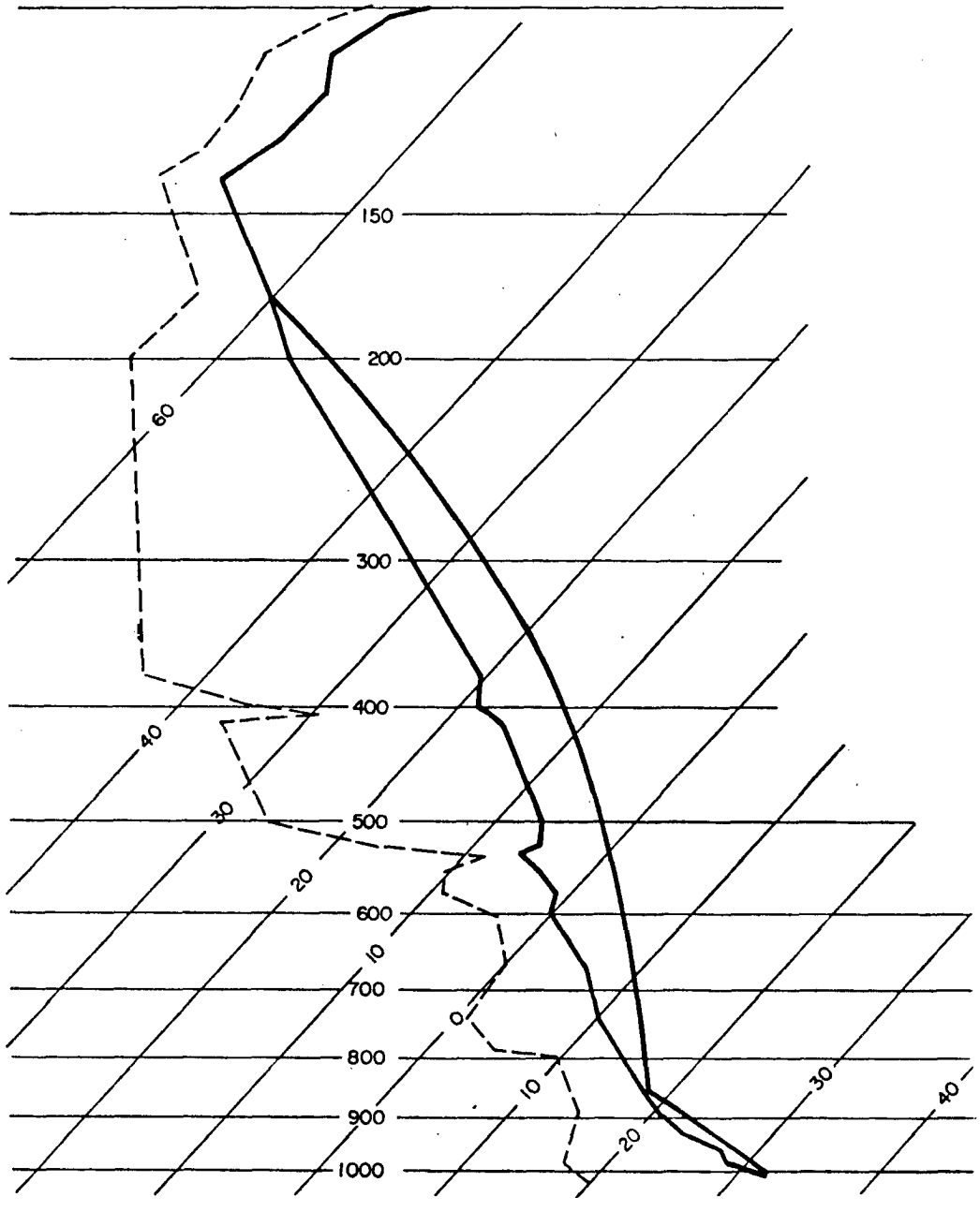

Fig. 4.6: Sounding used to initialize Set C (8.13.75).

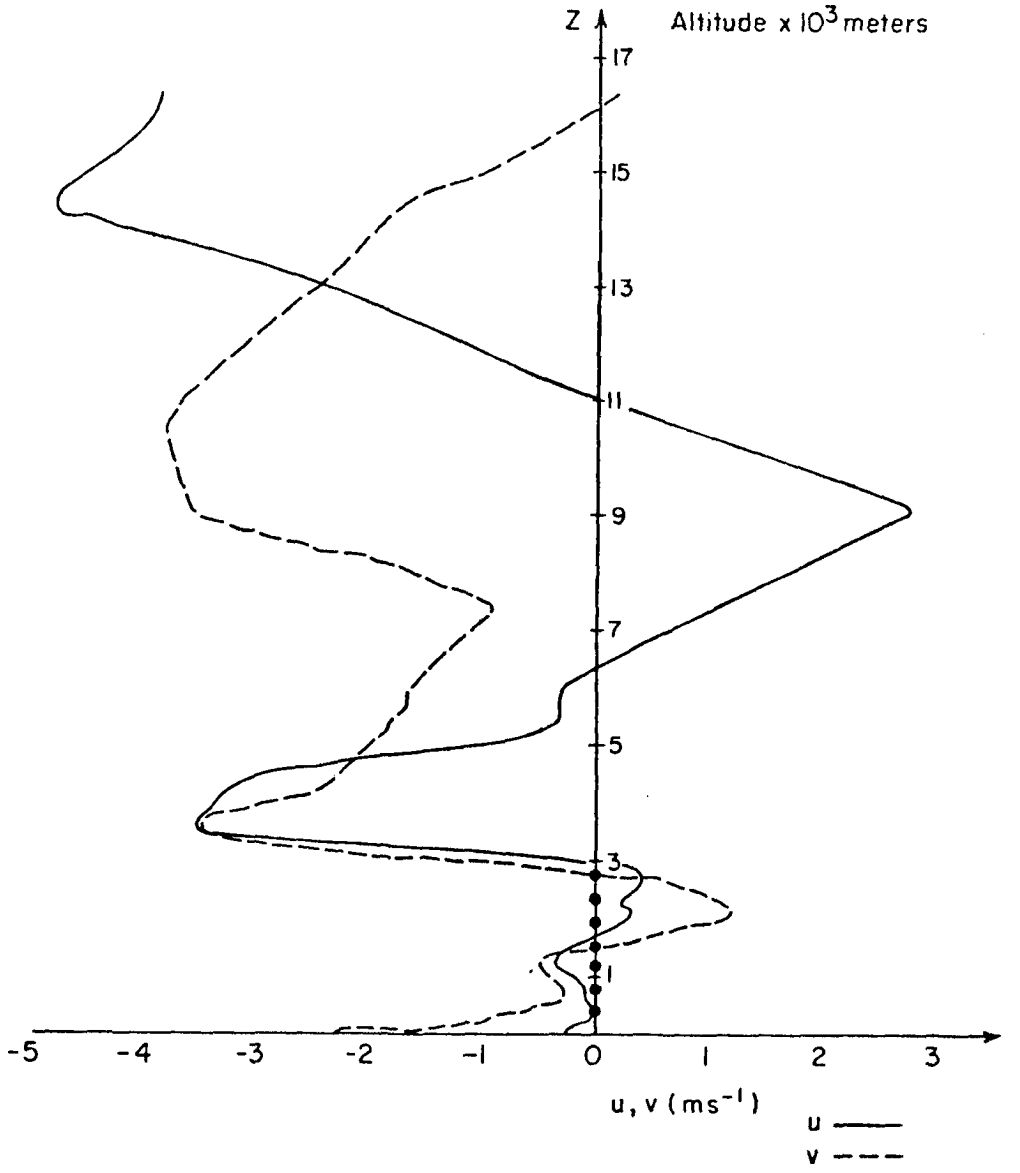

Fig. 4.7: Wind profile used to initialize Set C. v was set to zero from ground to z = 2.9 km (dotted line). The convergence reproduced v (dashed) at F.O.S.

Table 6: Initial mean vertical velocity

z (Km)	w (cm s^{-1})
.359	4.6
.728	5.9
1.109	7.3
1.504	8.8
1.913	8.1
2.338	3.4
2.780	1.0
3.244	0

b. The seeded run C-1S:

This run is identical to the reference run except that from 2000 sec until 2700 sec seeding is simulated by setting the IN concentration equal to 100 ℓ^{-1} for two vertical grid points (at z = 5.952 km and z = 6.601 km) and for a horizontal area extending over -3.75 km $\leq$ x $\leq$ 1.25 km and - 5.25 km $\leq$ y $\leq$ -1.75 km. The lowest seeding level is at the -7^{o}C level.

In summary, Table 7 summarizes the sets of experiments performed in this study.

Table 7: Summary table of experiments

Experiment	Date	CCN	IN seed no seed	Comments
A-1R	8.25.75	300	no seed	Areal mean convergence to 4.5 km. 30% of the convergence is imposed as perturbation. Moist perturbation imposed autoconversion threshold is 10 μm.
A-1S	8.25.75	300	seed	
A-2R	8.25.75	300	no seed	Alternate shear regime.
A-2S	8.25.75	300	seed	
B-1R	8.25.75	300	no seed	Mean convergence to 3.25 km set on a line. 50% of convergence imposed as perturbation autoconversion threshold set to 14 μm.
B-1NI	8.25.75	300	no seed	no ice
B-2R	8.25.75	1000	no seed	
B-2S	8.25.75	1000	seed	
B-3R	8.25.75	1000	no seed	Autoconversion threshold adjusted above the -10^{0}C isotherm.
B-3S	8.25.75	1000	seed	
C-1R	8.13.75	1000	no seed	Convergence line to 3.25 km. 100% of convergence is imposed as perturbation. A nearly saturated layer is introduced.
C-1S	8.13.75	1000	seed	

5.0 RESULTS

5.1 Analysis, Philosophy and Reservations

In any experiment, numerical as well as laboratory, one should be very cautious in interpretation and application of the results to the real open system - the atmosphere. In a careful and reliable analysis one should bear in mind the deficiencies of his experimental system and "screen" the results before drawing conclusions. Such a screening is especially important in interpretation of model results, as a model usually parameterizes many processes quite crudely. Numerical procedures and schemes often introduce errors to which no physical explanation exists. The results are presented in full in the form of quantities of model variables and cross sections at different planes of the domain. No screening is done in this chapter and results are presented exactly as read from the model runs. Whenever possible comparison with information from observations, physical theories and other models is done to prevent erroneous conclusions.

During the model run, analysis files are written periodically at 100 second intervals containing the model-predicted variables and integrated budgets such as water and energy budgets. Consider, for example, a continuity equation for a general nonconservative parameter or function F,

$$\frac{dF}{dt} = \frac{\partial F}{\partial t} + U_i \frac{\partial F}{\partial x_i} = \Sigma S_i \quad , \tag{5.1}$$

where S_i are the source and sink terms. The above combined with the mass continuity equation gives the flux form of the continuity equation:

$$\frac{\partial}{\partial t}(\rho F) + \frac{\partial}{\partial x_i}(\rho F U_i) = \rho \Sigma S_i \tag{5.2}$$

To get the budget of the source and sink terms one needs to integrate the above over the cloud volume and over time.

In dynamic seeding we are interested in the integrated rain at the ground. With V_T denoting the terminal velocity of the hydrometers, and r_w the mixing ratio of total condensed water the vertical flux per unit area is $\rho r_w V_T$ and the fallout is the rate of change of flux in the vertical or:

$$Pr = \frac{\partial}{\partial z}(\rho r_w V_T) \tag{5.3}$$

Integrated over time and area, the above equation gives the precipitation. The condensation is similarly computed integrating the vapor flux through cloud base. Nehrkorn (1981) used those two budgets to define a precipitation efficiency parameter that accounts also for storage rate. In dynamic seeding, the concept is to increase rainfall by processing more water and not necessarily by having more efficient clouds. Therefore, the total budget is calculated as well as differences in mass and moisture convergence. As the model is very sensitive to microphysical parameters, an attempt is made, when possible, to compare mixing ratios and size distributions of droplet populations to actual measured and observed ones. Cotton, Nehrkorn and Hindman (1981) analyzed water content measurements taken in the clouds on 25 Aug 1975.

The precision of the foil impactor used for the size distribution measurements is limited, however. Size distribution and water contents are accurate to ± 50% and the minimum detectable droplet is 0.5 mm in diameter. Results from Cotton's (1972) one dimensional model runs are directly quoted from model output and the seedability parameter is usually compared to the three dimensional model results as it is commonly used as a decision-making tool. The results are summarized for the reference run of each experiment and for the response due to the change introduced (i.e. seeding, shear, CCN).

5.2 Alternated Shear: Set A, experiments A-1R, A-1S, A-2R, A-2S

5.2.1 - West inflow: Runs A-1R, A-1S

a. Run A-1R - west inflow

Following initiation the cloud develops fast sending one strong tower (w_{max} = 31.5 ms^{-1}). The tower is seedable at 900 s. The vertical growth rate of the tower is $\leq$ 2 grid points (1500 m) in 100 s corresponding to 15 ms^{-1}. Simulated downdrafts have magnitudes of 5 ms^{-1} or less and descend to 750 m height at 1200 s. Somewhat later strong downdrafts (~10-14 ms^{-1}) are simulated at heights of 1.9-3.4 km. The intensity of the downdrafts weaken considerably by the time they reach the surface, however. The surface mesohigh reaches a maximum at 1100 s (Δp = 0.39 mb) and at 1500 s (Δp = 0.58 mb). The simulated surface mesolow reaches a minimum at 600 s (Δp = -0.19 mb) at 2700 s (Δp = -.21 mb), and at 3100-3300 s (Δp = -.25 mb). Warm rain processes in the model are very fast and surface rainfall starts at 300 s. This early precipitation creates a mesohigh at the ground and masks any attempt to track expected surface pressure lows associated with seeding.

b. Run A-1S - the seeding response

Seeding of cloud A-1 was simulated by introducing 100 crystals ℓ^{-1} at two vertical levels (Z = 5.6 km and Z = 6.4 km) between 900 s and 1500 s. The seeding resulted in simulated temperature increases of up to 1.5°C (at 1000 s) in the seeded volume. One grid point (750 m) below the seeding level, temperature drops of 0.3° to 0.5°C were simulated, reflecting enhanced entrainment at this level. The buoyancy enhancement was accompanied by vertical acceleration and updraft enhancement of up to 1.4 ms^{-1} at the seeding level of 2.56 ms^{-1} one level (570 m) above the seeding level. The downdrafts were intensified by only 0.1 ms^{-1} at the lowest level (0.4 km) and by 4.6 ms^{-1} below the seeding level.

Immediately after seeding started, at 1000 s there was a "jump" in the kinetic energy due to the enhanced vertical velocity. This "jump", however, reached a peak at 1300 s at a value which was greater by only 0.4% than the natural case. Following that, the kinetic energy of both cases followed a similar structure with another peak at 1800 s as is illustrated in Fig. 5.1. The seeded case's energy was lower by 1.5-2.7%, however. At 3000 s the kinetic energy stabilized in both clouds with a higher value for the seeded cloud. Soon after seeding started the liquid water content dropped at the lowest seeding level by 5.11 g kg^{-1} at that level. At the next level (Z - 6.4 km) the graupel content continued to rise by 2.67 g kg^{-1}, but no changes in liquid water content due to freezing were simulated.

The cloud pressure field in both the "natural" and the seeded cloud is similar with a pressure low at low levels which drives the inflow of air into the updraft and a high pressure at the top of the cloud. The cloud base low does not get to the surface due to the

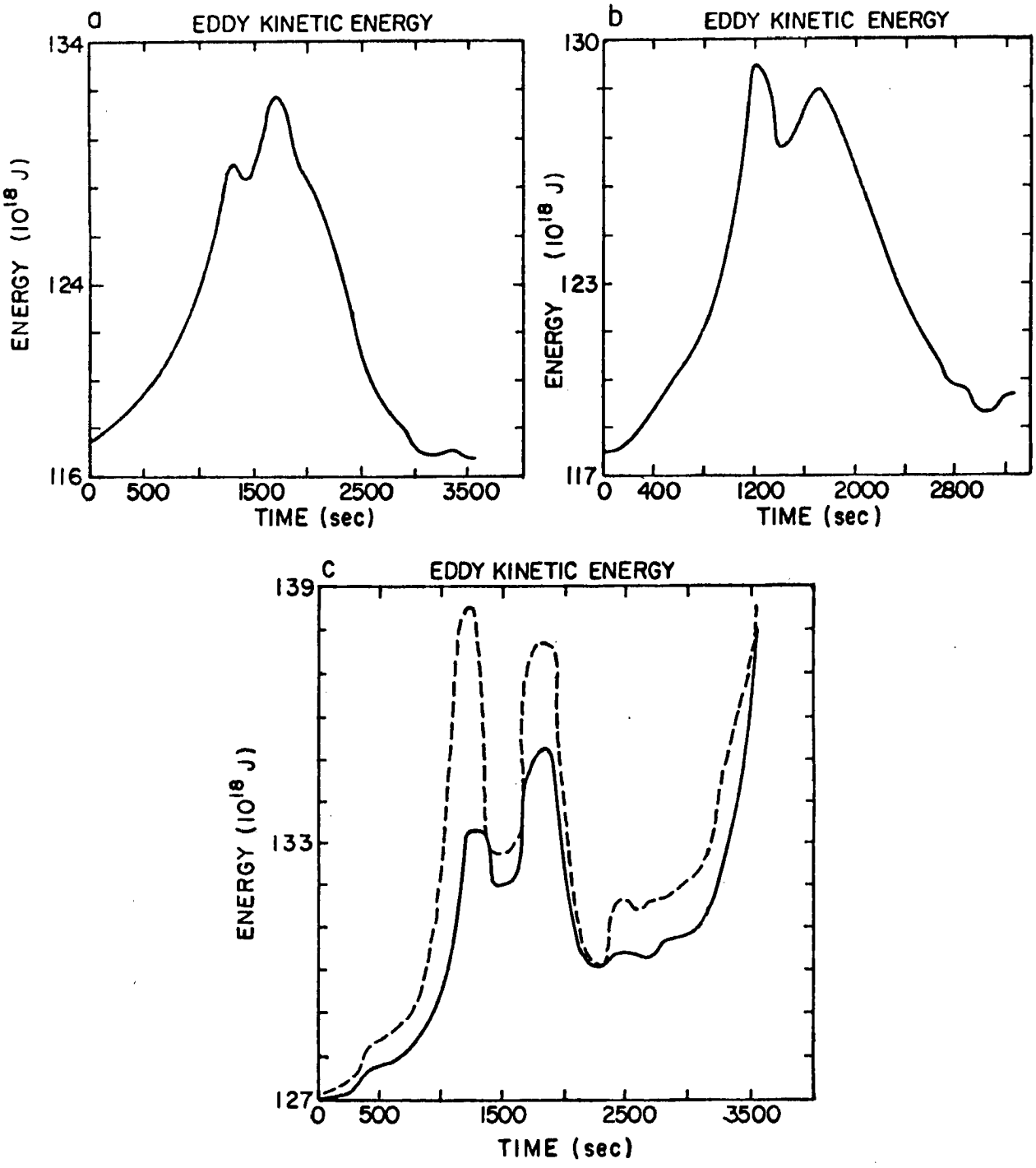

Figure 5.1: Kinetic energy: a. A-1R b. A-1S c. A-2R: solid
c. A-2S: dashed

mesohigh established there by the early rain. However, starting at 1000 s and up to 1500 s the surface mesohigh in the seeded subcloud layer is ~0.1 mb lower than under the unseeded one. This could indicate that the "pressure communication" noted by Cunning and DeMaria (1981) is indeed simulated, especially as at this time there is more precipiation falling, and, due to that fact alone, higher surface pressure could be expected. (Note: it is before downdrafts reach the lower grid point!). They measured a pressure drop of 0.35 mb, however. Fig. 5.2a-f shows the pressure fields at 1000 s, 1100 s and 1500 s (A-1R vs. A-1S). Fig. 5.3 shows the pressure field evolution for A-1S. The net inflow of water vapor into cloud base at the end of seeding and after seeding ends increases by up to 6.7×10^7 gs^{-1} (10%), and it causes an increase of 0.03 g kg^{-1} in the boundary layer vapor mixing ratio averaged over the domain.

The total precipitation increases by 8% following seeding, but decreases by 8% on the long run due to earlier dissipation of the seeded cloud. At 2700 s the seeded cloud cuts off to become an anvil aloft and two bubbles below whereas the unseeded is still more intense. Overall precipitation at the end of 3600 s of simulation is lower in the seeded case. Fig. 5.4 shows the three dimensional cloud field of A-1S in 300 s intervals. Fig. 5.5 shows integrated precipitation for A-1R vs. A-1S. Fig. 5.6 shows precipitation falling on the inflow flank.

In summary, seeding resulted in a simulated subcloud pressure drop of 0.1 mb, subcloud downdraft intensification of only 0.1 ms^{-1}, an increase of 10% in moisture inflow into cloud base, but in less efficient processing of that moisture in the long term due to more

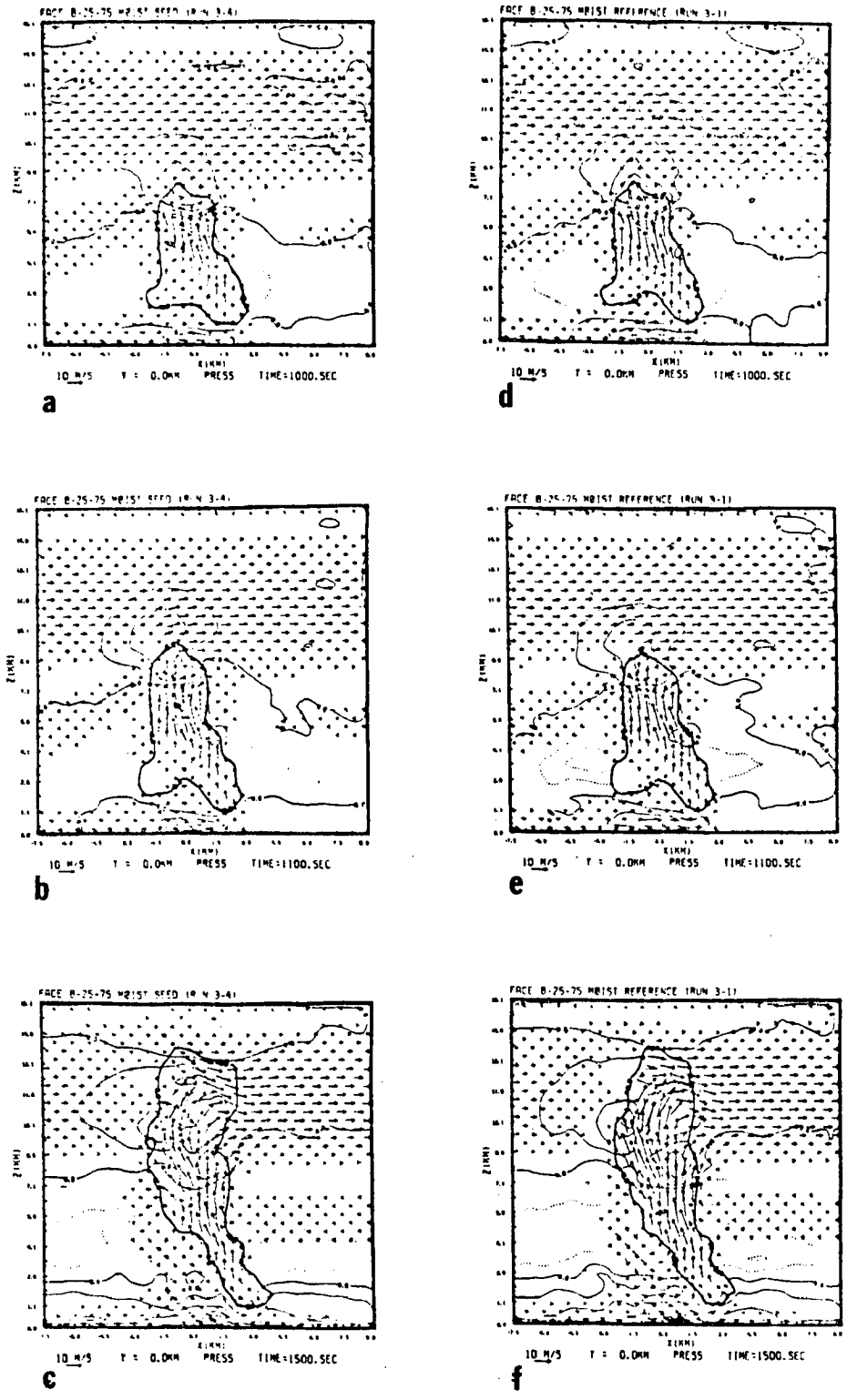

Figure 5.2: A-1R vs. A-1S Pressure fields at times 1000 sec (a,d) 1100 sec (b,e) 1500 sec (c,f)
a-c shows 'natural' case A-1R
d-f shows seeded case A-1S.
Thick solid line is cloud's outline. Isobars are contoured at 0.1 mb. Solid lines are positive perturbations. Dotted lines are negative perturbations.

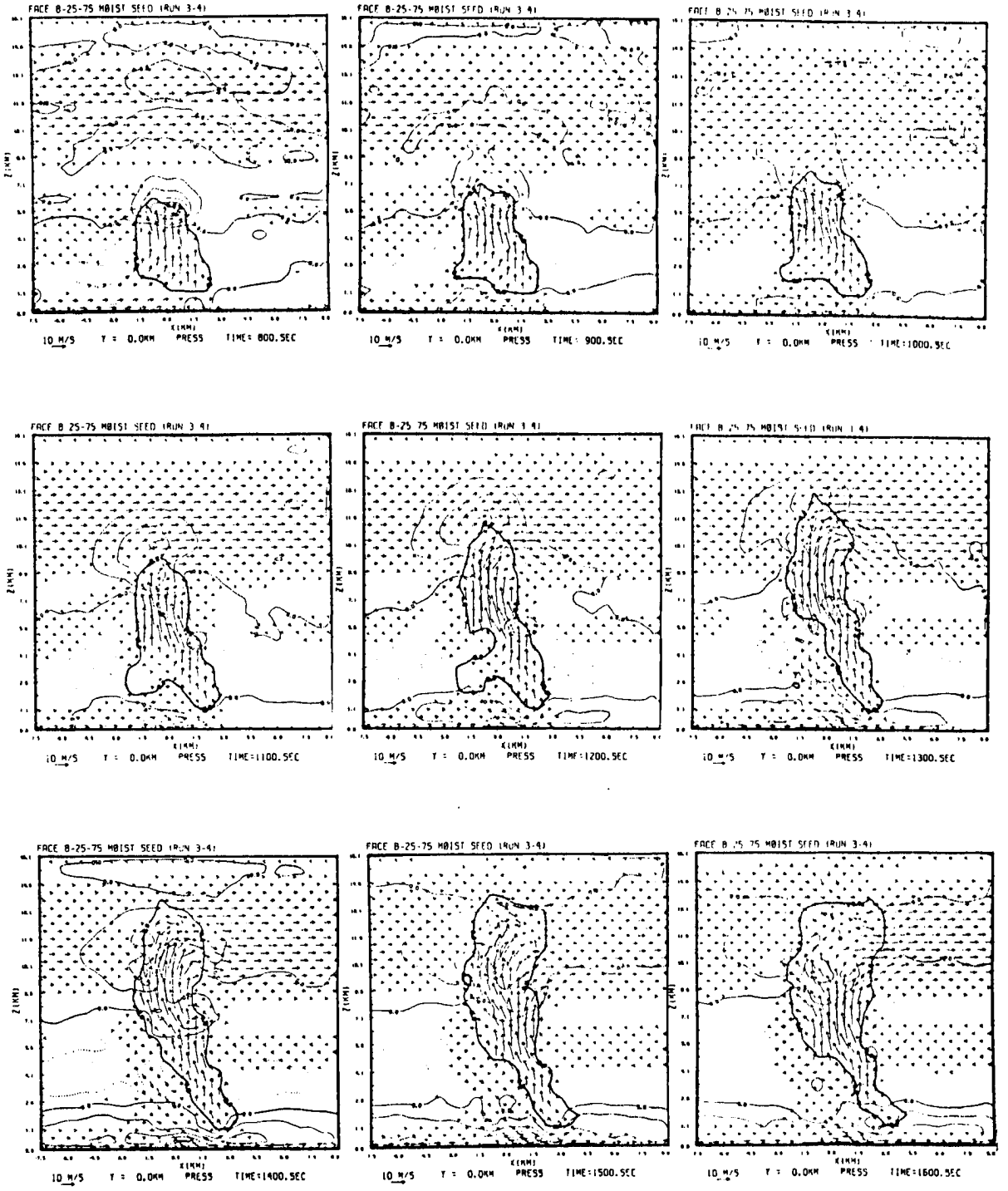

Figure 5.3: Pressure field evolution before during and after seeding for run A-1S. Seeding was introduced between 900-1500 sec. Solid lines are positive perturbation, dotted lines are negative perturbations. Contouring as in Fig. 5.2.

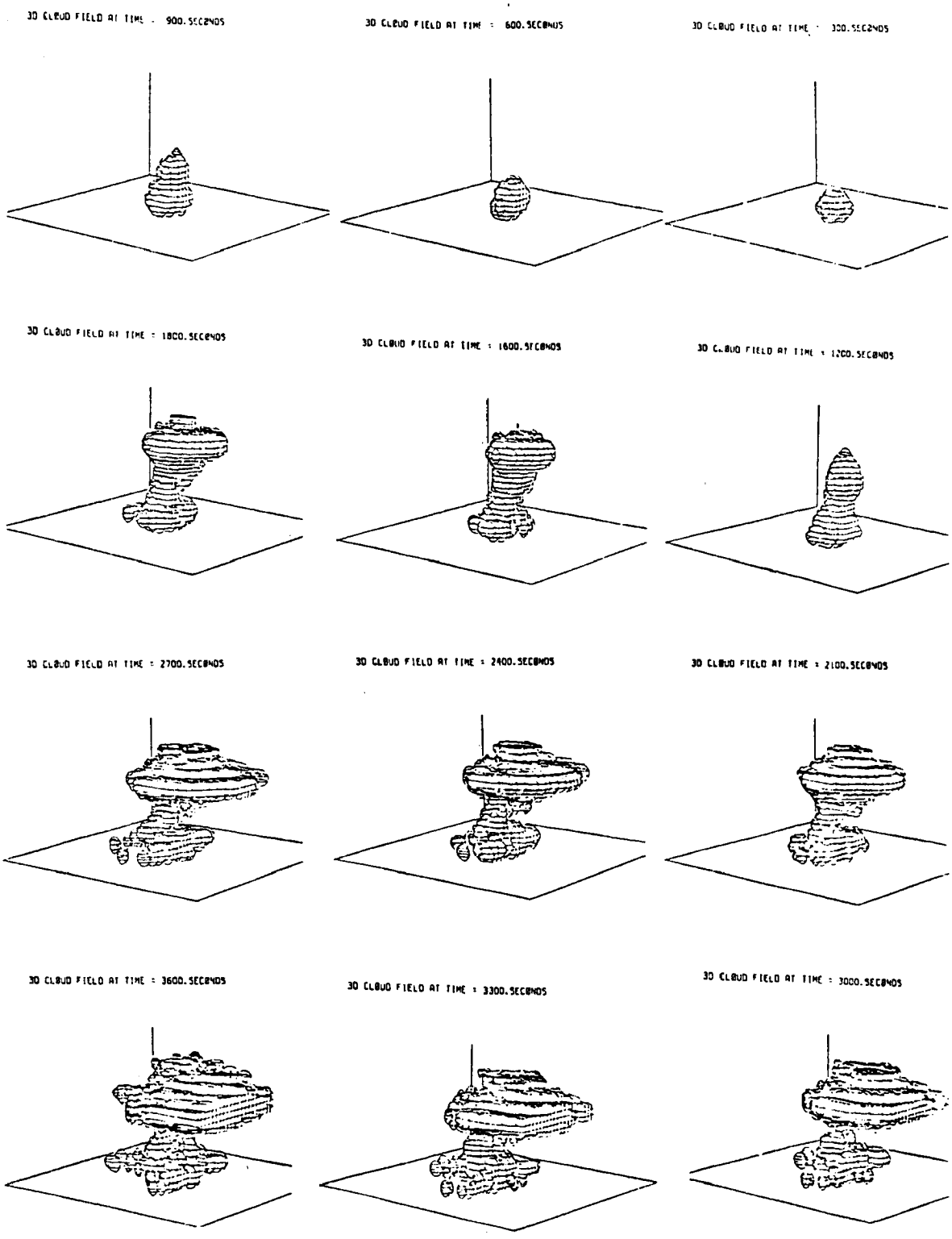

Figure 5.4: 3-D field every 300 sec for case A-1S.

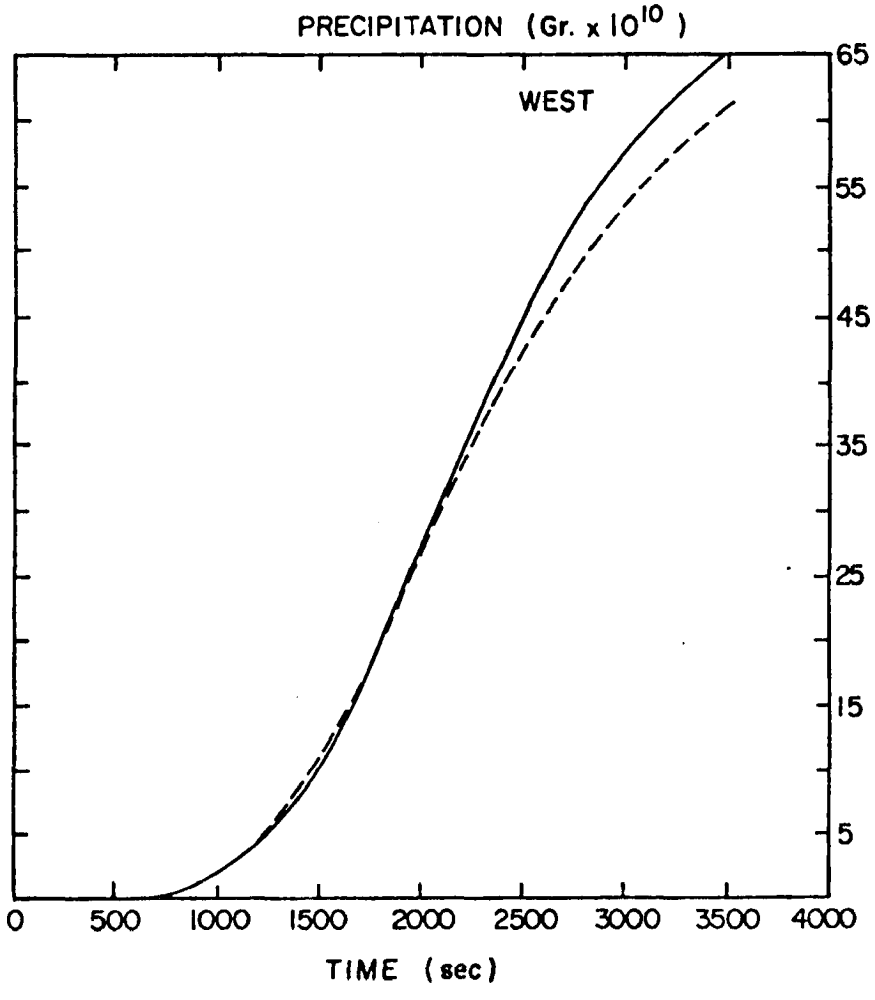

Figure 5.5: Precipitation (integrated quantities) vs. time for A-1R [natural solid line] and A-1S [seeded dashed line].

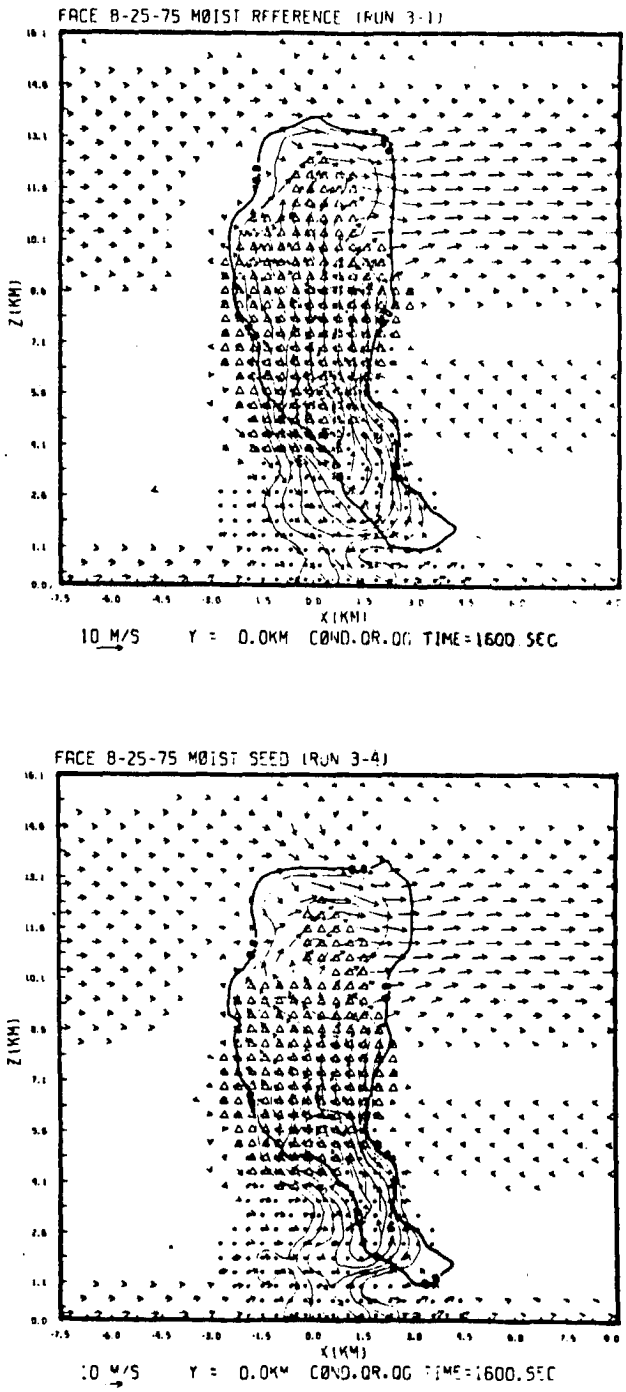

Figure 5.6: Precipitation falling on the inflow flank at 1600 sec. of simulation for the reference (upper) and seeded (lower) runs. Mixing ratio contoured at 1 g kg^{-1} intervals.

entrainment and inhibitation of subsequent tower development. Temperatures increased by an average of $0.5^{o}C$ in the seeded volume and vertical velocity increase by 2.5 ms^{-1}.

5.2.2 East Inflow: Run A-2

This experiment is identical to experiment A-1 except that the low level flow was changed from westerly to easterly to examine the response to mesoscale modification and to prevent precipitation from falling on the inflow flank.

a. Run A-2R - the reference run

The cloud sends one tower at the center of the domain and is seedable at 900 s. At 1800 s, an anvil is seen between 10 and 13 km expanding to the northeast. An early maximum vertical velocity of 30.2 ms^{-1} is reached at 1200 s (z = 8.6 km). The highest downdraft speed (12.6 ms^{-1}) is reached at z = 2.6 km at 1800 s, but it gets to the lowest grid point at a value of only 5.7 ms^{-1} (vs. 6.1 ms^{-1} at that level in the west inflow case A-1R). The subsequent towers after the "cut off" are much stronger than in run A-1R. At the end of 3600 s simulated precipitation is less in A-2R than in A-1R by 4%. However, after an hour's simulation A-1R is decaying fast whereas A-2R has still a lot of moisture and potential to precipitate (see Fig. 5.7). The cloud is therefore simulated to 4500 s.

At the surface a low pressure region exists from the initialization until the cloud is seedable. At that time (900 s) the low pressure center is at 4.8 km expanding symmetrically to the surface at a distance of 5 gird points to the east and west of cloud base. Below cloud base there is a mesohigh due to rain, with the same perturbation values as in A-1R, at the precipitation flank.

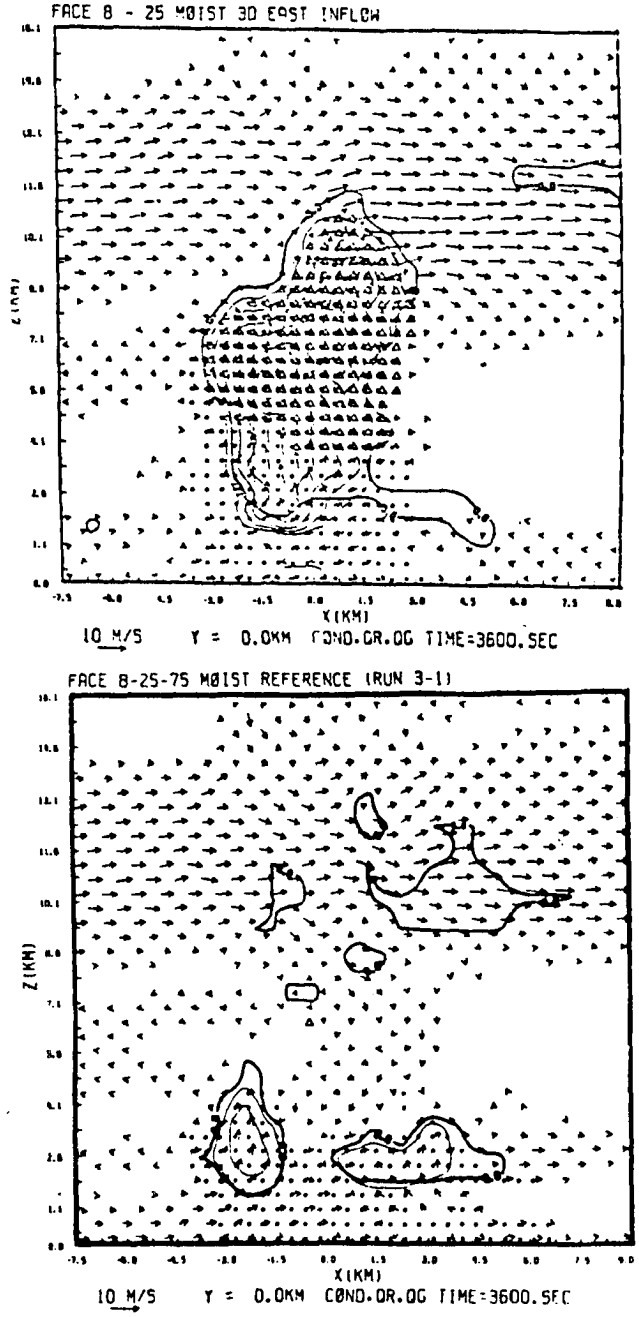

Figure 5.7: Cloud and precipitation fields at 1 hour for reference run A-1 (below) and reference run A-2 (east inflow) (above). Contours as in Fig. 5.6.

The change in shear regime resulted in some weakening of both the simulated updraft and downdraft velocities (0.4 - 1.3 ms^{-1}) and in a much longer living storm that yielded 32% more rain. Simulated pressure perturbation values remained unaltered. As is shown in Fig. 5.1c, the eddy kinetic energy of storm A-2 is still rising at the end of an hour's simulation while A-1's energy is declining as A-1 is dissipating already.

b. Run A-2S - the seeding response

Seeding was simulated by introducing 100 crystals ℓ^{-1} at two vertical levels (Z = 5.6 km and Z = 6.4 km) between 900 s and 1500 s. The seeding resulted in simulated temperature increases of up to 1°C at the first level of seeding (5.6 km) and up to 1.4°C at the next two levels. A corresponding vertical velocity enhancement of 1.59 - 2.38 ms^{-1} was simulated at those levels. The maximum updraft velocity (32.5 ms^{-1}) which occurred 300 s after seeding stopped, remained unchanged, however. The changes in vertical velocity is reflected by the eddy kinetic energy. The eddy kinetic energy of A-2S followed the same evolution and structure of the reference run's kinetic energy but exhibited values higher by 1.8% - 4.2% is illustrated in Fig. 5.1c.

Though following seeding downdrafts intensified by 2 ms^{-1} at mid levels (-20.1 ms^{-1} vs. -18.1 ms^{-1} at 2100 s), this intensification was not communicated to the surface, and at the lowest grid point (0.4 km) the seeded cloud's downdraft (5.5 ms^{-1}) was a little weaker than the unseeded reference downdraft (5.7 ms^{-1}). The response of the water mass field to simulated seeding was the freezing of liquid water which dropped by as much as 7 g kg^{-1} in liquid water content at the

first seeding level and 4.6 g kg^{-1} at the next seeding level. A corresponding increase of 9.75 g kg^{-1} and 2.84 g kg^{-1} in graupel content at the first and second seeding levels respectively, was simulated.

Just above seeding level at the location of the updraft outflow, a high pressure region was simulated. A low pressure region was simulated at midlevels. Two hundred seconds after seeding starts, the low deepened at the seeding level. A high formed at the surface due to rain (starting at 900 s). Following seeding (1800 s - 2000 s) the surface high values dropped by ~ 0.1 mb with respect to the reference run. As simulated precipitation was almost equal in the seed, no-seed cases, this pressure fall is probably a reflection of the "pressure communication mechanism" suggested by Cunning et al. (1981). Fig. 5.8 shows the pressure field evolution. Note that since the pressure fall is imbedded in high pressure, it is unlikely to have major dynamic effect. The pressure fields at the times when seeding-induced pressure differences exists are shown in Fig. 5.9.

Differences in the total precipiation in the first hour of simulation were very slight, starting with a slight increase (up to 7%) right after seeding stopped (1500 s) and continuing with an equal decrease after 2000 s. At the end of 3600 s the total precipitation was equal in both cases (see Fig. 5.10). No positive results for precipitation enhancement are seen due to seeding. The seeded cloud yielded up to the end of simulation at 4500 s 5.7% less precipitation. The change in wind regime gave a 32% increase in precipitation in the east inflow (A-2) seeded case versus the west inflow (A-1) seeded case and a 33.8% increase in the natural east flow cloud versus the natural

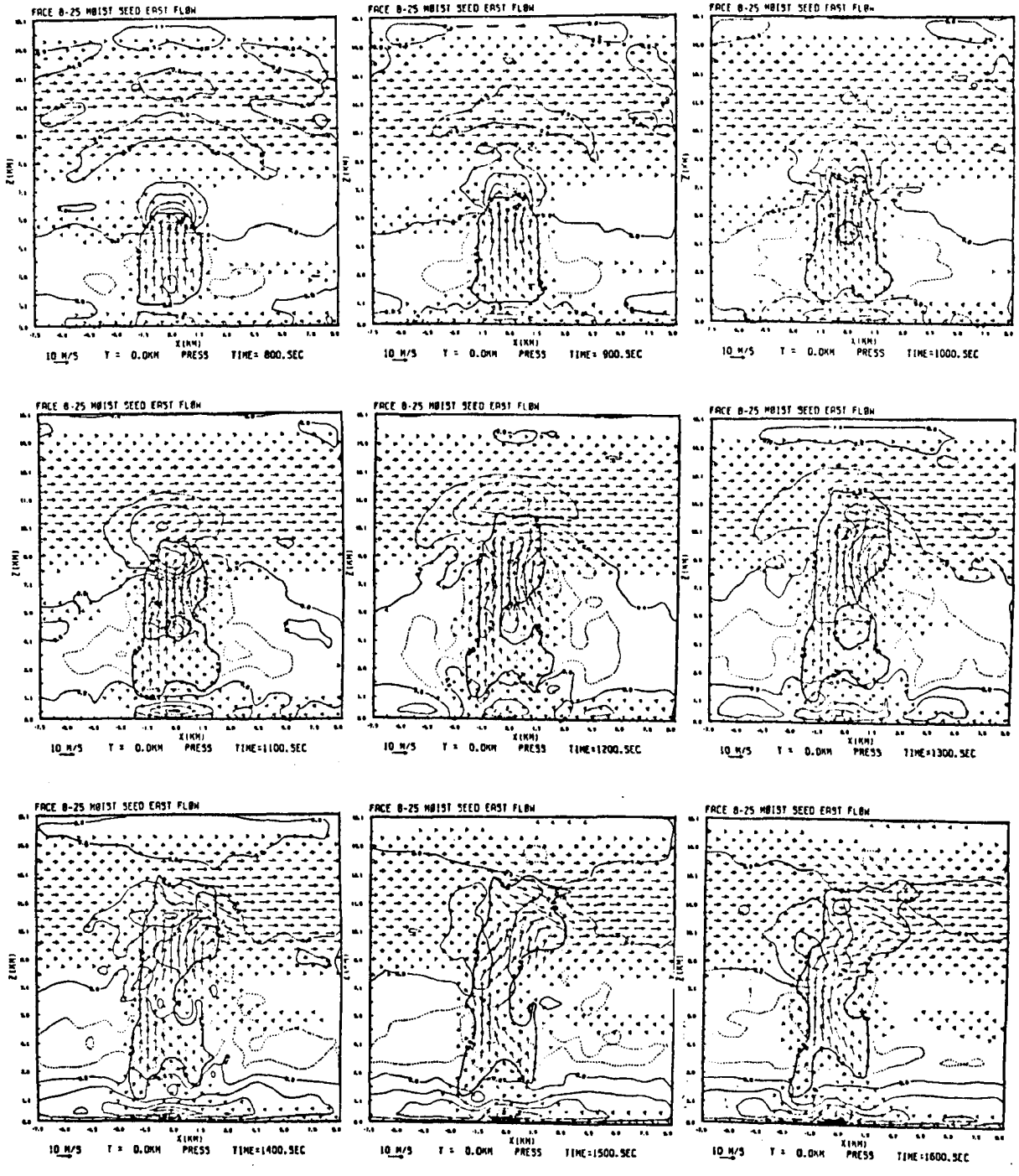

Figure 5.8: Subcloud high pressure build up before, during and after seeding for A-2 seeded east flow case. Seeding was performed between 900 and 1500 sec. Solid lines are positive pressure perturbation, dotted lines are negative pressure perturbation. Contours as in 5.2.

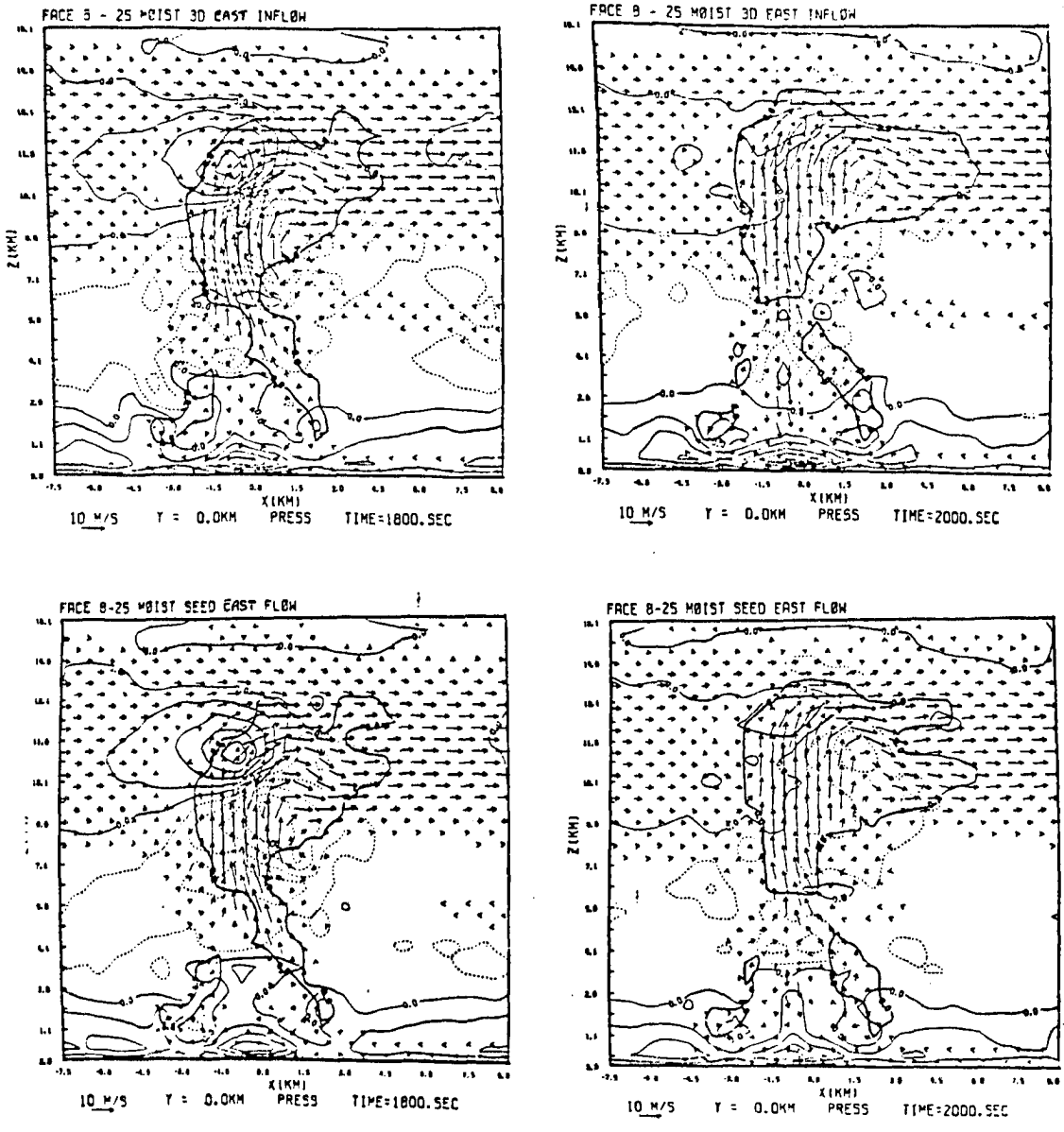

Figure 5.9: Pressure fields at 1800 sec and 2000 sec for A-2 seeded and no seed cases. Contours as in 5.2.

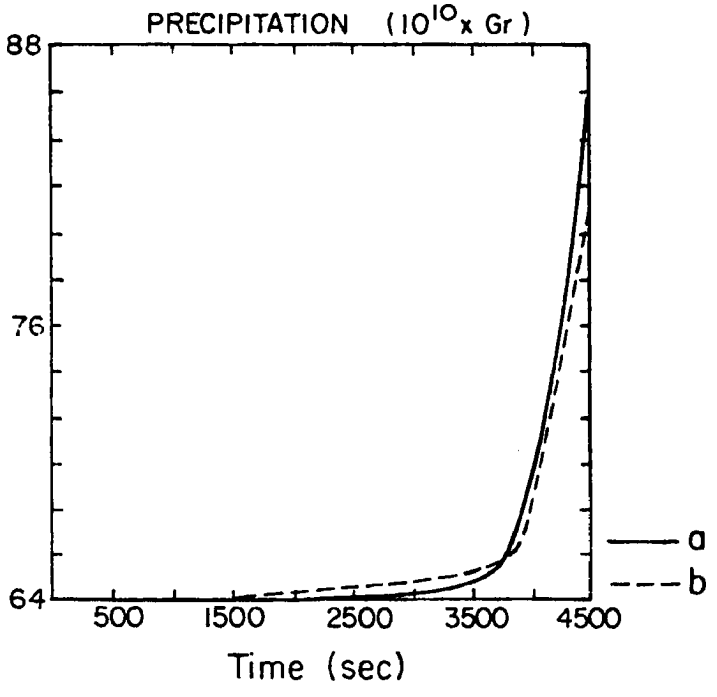

Figure 5.10: Total cumulative precipitation for the time 0-4500 sec for A-2 : a. reference b. seeded.

west flow one. This is assuming that the west flow cases were indeed in the final dissipative stages and used all their precipitable water (Fig. 5.7). Considering that some precipitation would still fall from them after 3600 s could bring the above percent increase down by 2%-3% but the values are still high.

In summary, Set A resulted in an overall mild response to seeding. Vertical velocities were enhanced by up to 2.5 ms^{-1}. Potential temperatures increased following seeding by an average of 0.5°C in the seeded volume, an increase which is in good agreement with previous estimates (Nehrkorn, 1981). The kinetic energy showed only a small modification due to seeding. Pressure fields at the surface showed modification due to seeding in values that are 35% of the values measured by Cunning and DeMaria (1981). These pressure drops were associated with a 10% enhanced moisture convergence. This added moisture, however, was not efficiently processed by the cloud due to the drying influence of enhanced entrainment. Downdrafts were also enhanced at midlevels. However this enhancement communicated very weakly to the subcloud layer. Precipitation was enhanced slightly right after seeding, but inhibited in the long run. The mesoscale modification of the shear regime resulted in a differently organized stronger storm yielding 33% more rain, but having no greater response to seeding.

The reference runs showed, in general, features similar to some observed ones. The clouds of Set A were very vigorous corresponding to the fourth, unseeded "explosive" cloud observed at the FACE site on August 25, 1975, except for the "cut off" towers that were not observed. Cunning hypotehsized that the observed cloud was actually seeded by the seeding agents with which three former towers were seeded. If so, these clouds are not the observed ones. The location of formation of

first rain water - near cloud top at early stages, appears to be in agreement with observations (Cunning, 1981 and Takahashi, 1981) and other simulations (Takahashi, 1981, Nehrkorn, 1981 and others). Measurements made in the three passes through cloud 2 on 25 Aug 1975 show good agreement (±50%) between measured and predicted mixing ratios for cloud water (0.5 - 2.0 g kg^{-1}) and graupel (0-0.4 g kg^{-1}). Rain water, however, seems to be overpredicted by the model for Set A by an order of magnitude. It is important to mention that the measurements taken were very limited and with accuracy of ±50%. Results of the three penetrations into the cloud are different one from the other. The warm rain processes in Set A seem to be too fast resulting in immediate premature rain on the ground.

5.3 Convergence Line: Set B

5.3.1 The lower CCN case: Run B-1R, Run B-1NI

This run was designed as a reference run to the high CCN runs. The convergence pertubation is more realistic (along a line instead of symmetrical) and comparison with the real observed cloud is done whenever possible. The experiment is repeated with the ice phase (B-1NI).

a. Run B-1R - the reference run

The cloud started as a small tower at the site where a perturbation was imposed with a somewhat longer axis along the convergence line (at 300 s). At a later time, the tower grew vertically and laterally along the convergence line and two separate lines of convection formed to the east and west of the main tower. Those lines grew vertically at a slower vertical rate. At 3000 s the three subsystems merged to form a convection line with one central main tower. Fig. 5.11 shows the general three dimensional evolution of the cloud. In the early stages the vertical growth was approximately 1500 m

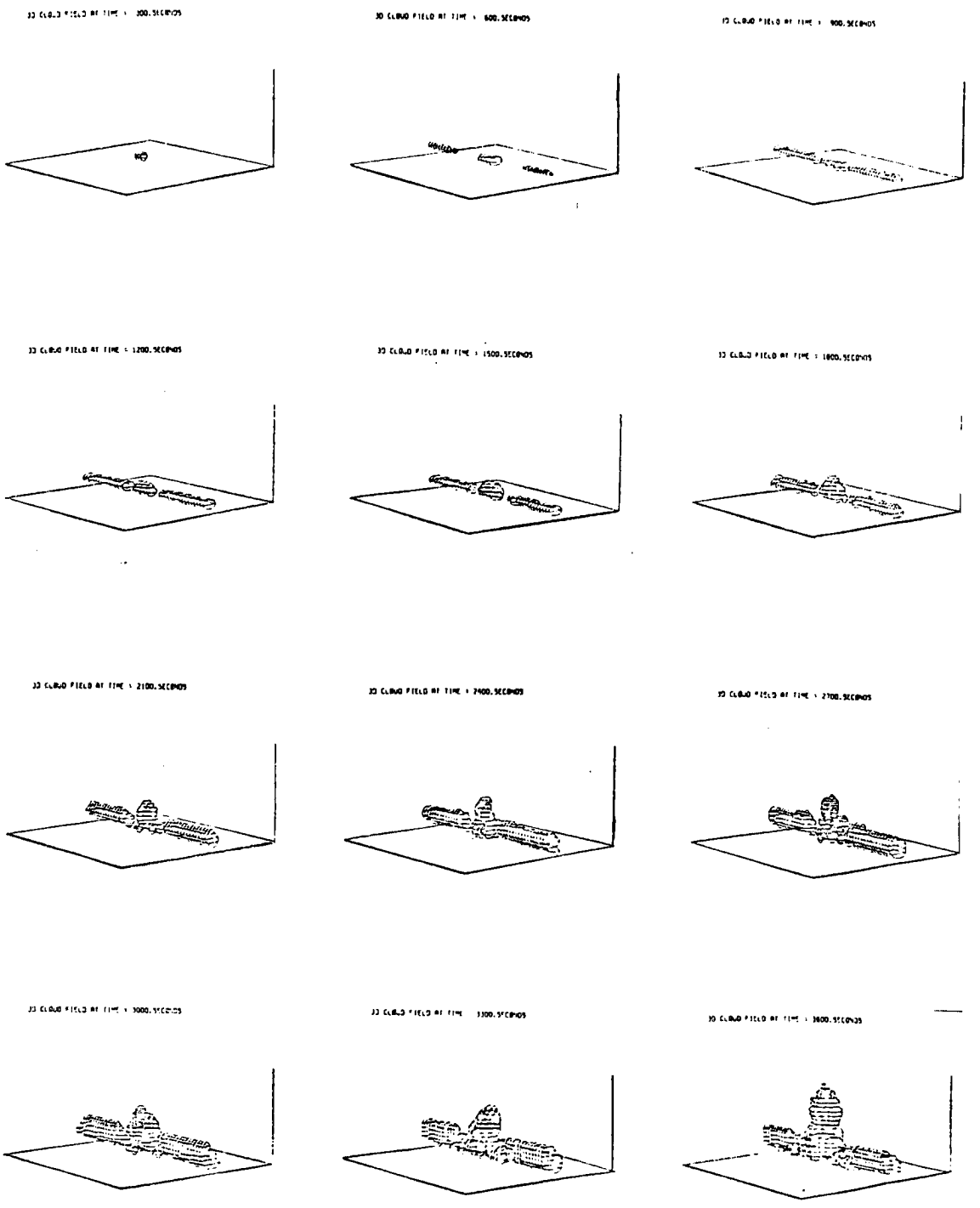

Figure 5.11: 3-D plots for CCN = 300 (B-1R).

in 500s and most growth was lateral. Starting at 1500 s growth was somewhat accelerated both laterally and verticall. The first rainwater appeared at the upper third of the cloud (around 4 km) at 1900 s. This was preceded by and accompanied (starting at 1600 s) by positive temperature buoyancy at mid-levels and negative temperature buoyancy just above cloud top. Vertical growth prior to ice phase was in a pulse-like fashion. It was not before 2300 s when first rain hit the ground. Peak updrafts of 10.8 ms^{-1} appeared at that time at a height of 3 km and at 2000 s. Elliptical downdrafts were seen surrounding the main updraft core at a height of 3.0-3.5 km, with peak value of 5.4 ms^{-1} on the north (see Fig. 5.12). However, at 0.4 km it diminished to 0.2 ms^{-1} and only after 2600 s did it get to a value greater than 2.0 ms^{-1}. The storm-induced circulation had a maximum downward motion of 6.2 ms^{-1} at a height of 4.0 km with maximum entrainment at the same level which is also the level of minimum equivalent potential temperature (see Figs. 5.13 and 5.14). This entrainment of return air flow led to "cut off" towers starting at 2400 s (see Fig. 5.15). Vigorous ice phase processes were introduced at 3000 s at a height of 6.5 km (~-11°C level). This was followed by a rapid growth rate and production of more ice. Cloud top reached the seeding level at 3000 s and the coexistence of ice phase and supercooled water at this level lasted until 3500 s. This leaves a "time window" of 500 s in which seeding can be performed. However, the cloud was so vigorous naturally that it was decided that a simulation of seeding would not be useful (the realistic "time window" for most seeding agents is between 5-10 min). Fig. 5.16 shows cloud growth between 3300-3600 s. The change in low level equivalent potential temperature shown in Fig. 5.14 represents cooling by

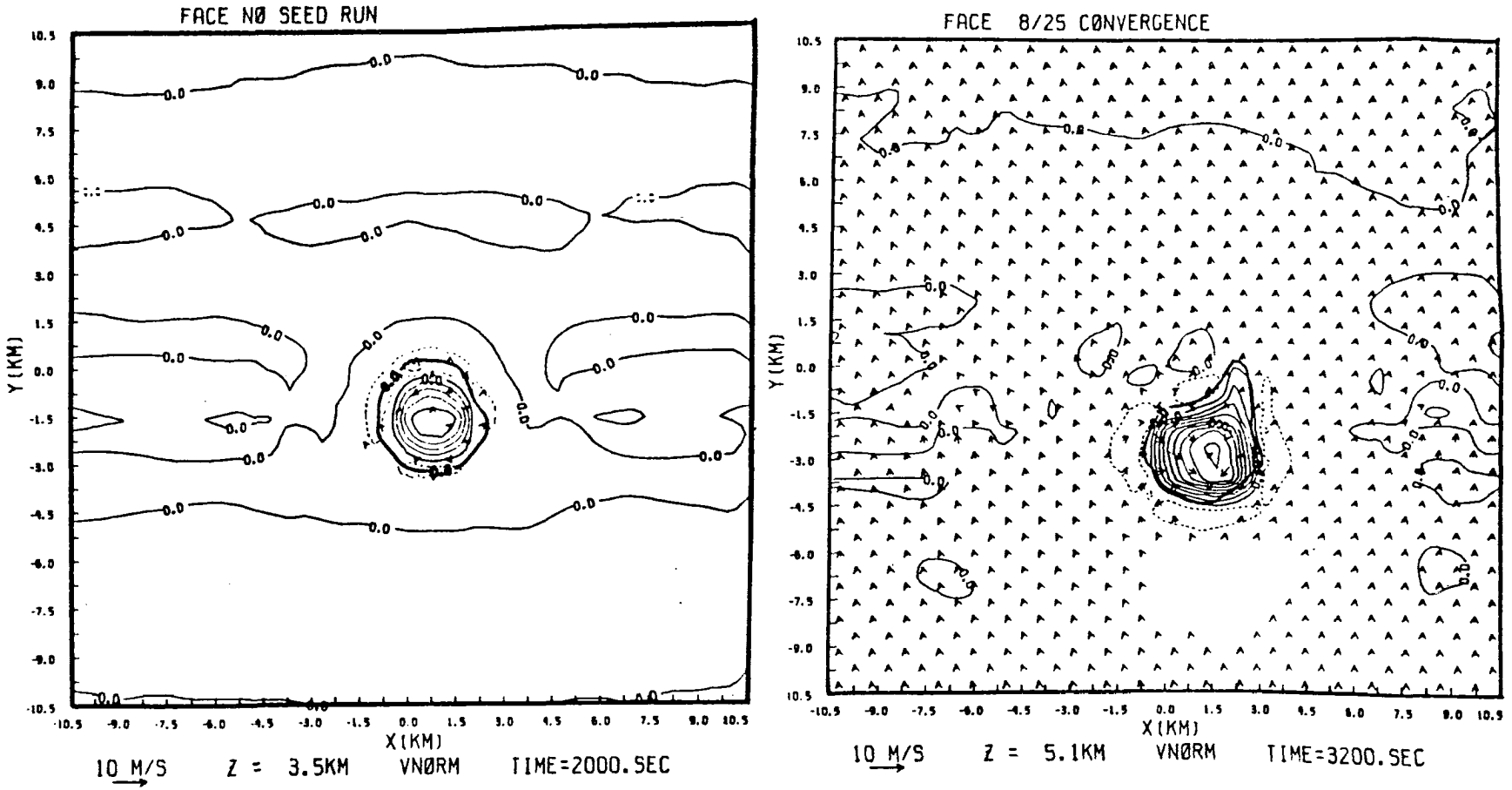

Figure 5.12: Vertical velocity structure on horizontal cross sections at heights of 5.1 km and 3.5 km and at times 3200 sec and 200 sec. For the low CCN convergence line case (B-1). Solid lines-updrafts; dashed lines-downdrafts. Contours at 1 ms^{-1} intervals.

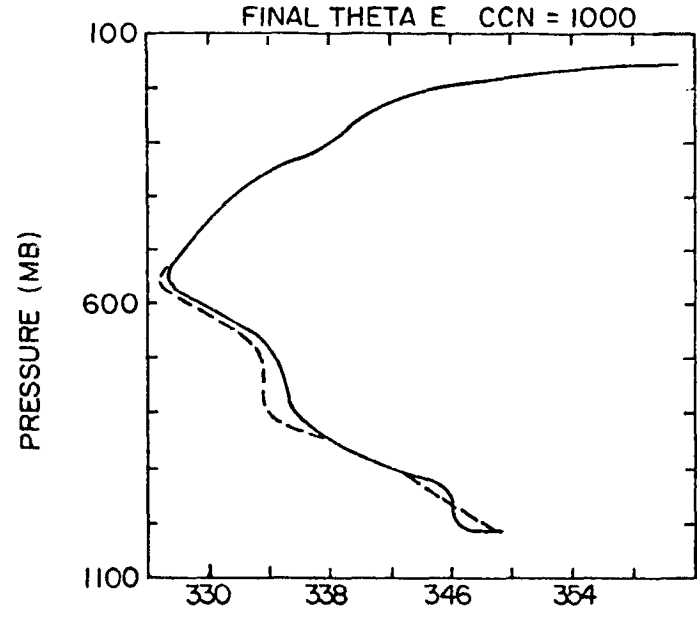

Figure 5.13: Environmental equivalent temperature for B-2R solid - final. Dashed - initial.

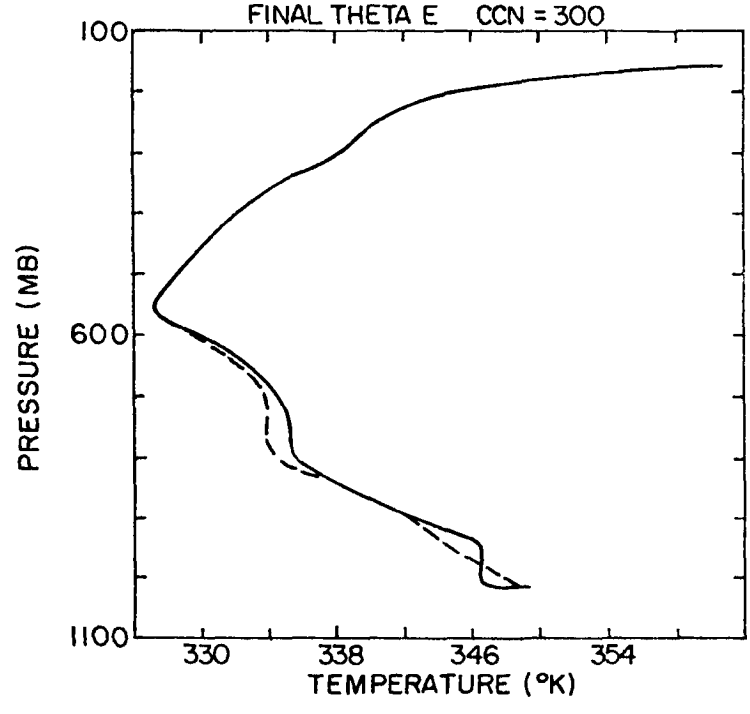

Figure 5.14: Environmental equivalent temperature for B-1R. Solid - final. Dashed - initial.

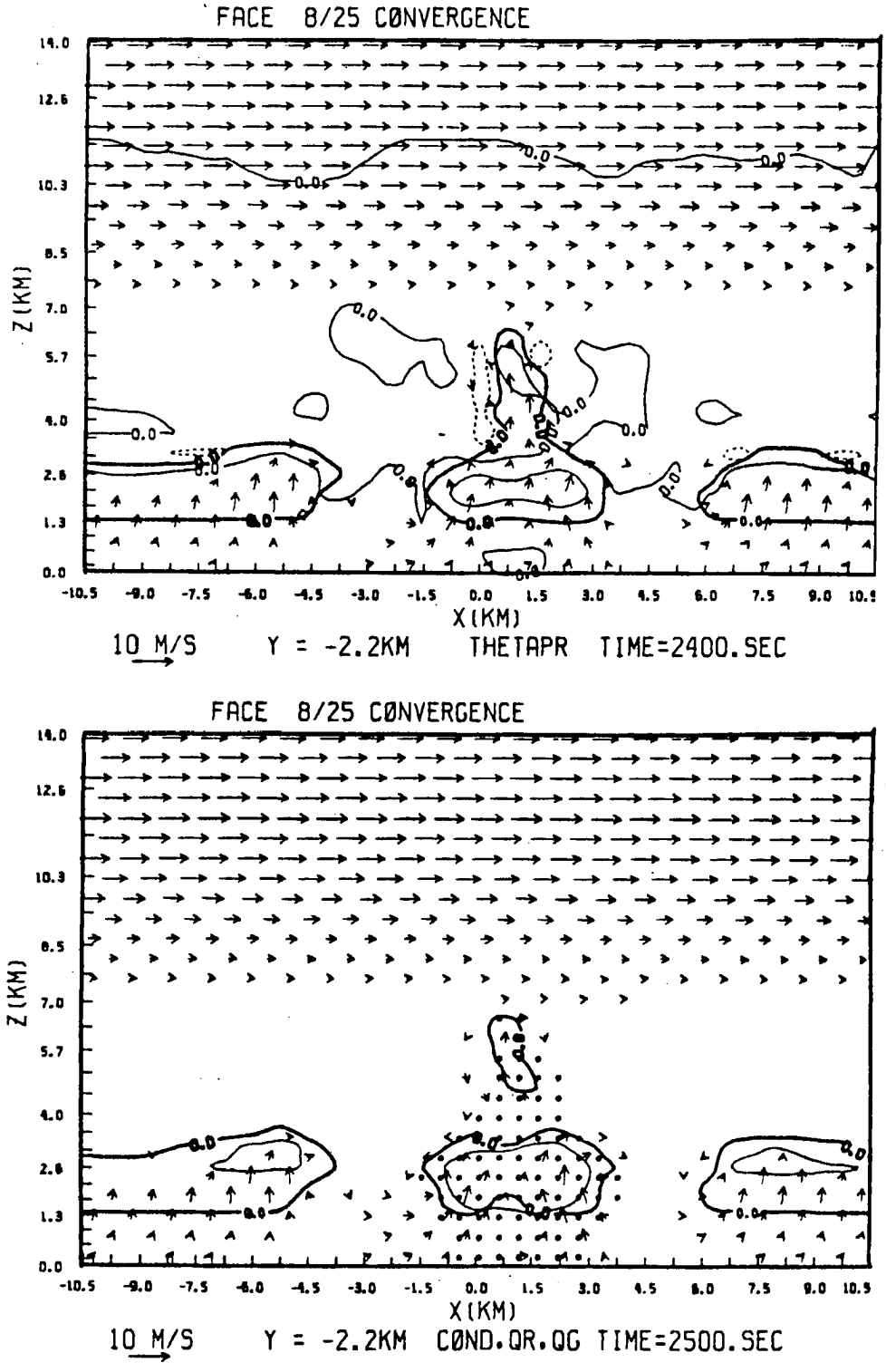

Figure 5.15: Evolution of "cut off" tower by entrainment for Set B low CCN cloud (B-1).

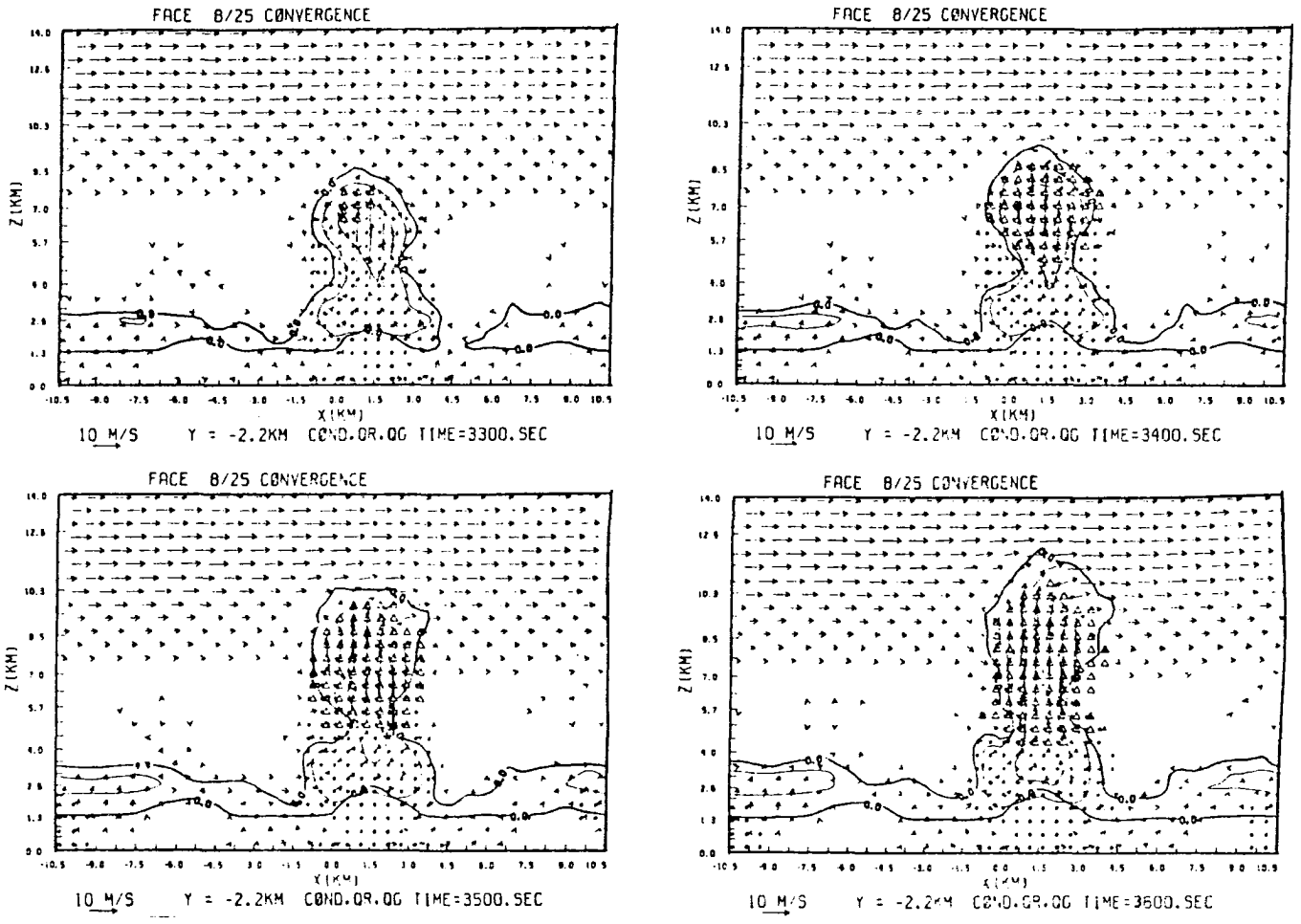

Figure 5.16: Set B. Low CCN case cloud (B-1R) growth on vertical cross section between 3300 s and 3600 s of simulation. Contours as in Fig. 5.6.

transport of low equivalent potential temperature air down by entrained downdrafts. The eddy kinetic energy constantly rose within the first hour of simulation as seen in Fig. 5.17.

From cloud formation a slight positive pressure perturbation was established at cloud top associated with cloud top divergent flow, with perturbation values ranging from 0.02 mb to 0.36 mb. Between 2800 s and 3000 s the outflow from the "cut off" upper dissipating tower converged just above the top of the lower main tower in association with slight low pressure anomaly (0.01 mb to 0.04 mb) at that level (6.5 - 7.7 km) (see Fig. 5.18). Following that episode, the cloud top high is restored for the rest of the simulation in a typical depth of 2 km. Starting at 1700 s low pressure associated with the convergence and entrainment of low level inflow and midlevel return flow persistently existed below the top high pressure layer, (with the exception of the 300 s gap, when it is "pushed up" to merge the "cut off" tower low). With vertical growth this low broadened upwards with higher values at levels of 5.7 - 7.0 km (low environmental equivalent potential temperature and ice formation levels). The intensity of the low pressure ranged between 0.03 - 0.26 mb.

Lower cloud levels were characterized by constant positive pressure perturbations with divergent flow and of varying intensity (0.02 - 0.25 mb) and depth (0.5 - 1.5 km).

The subcloud boundary layer pressure field along the convergence line exhibited positive, almost homogeneous (0.01 mb - 0.03 mb) pressure pertubations at the early stages (900 s) giving way to a more pronounced less homogeneous (-0.06 mb to -0.13 mb at surface) mesolow, with highest values below the centered tower at 1800 s (this is following condensation and conversion to rainwater but prior to rain

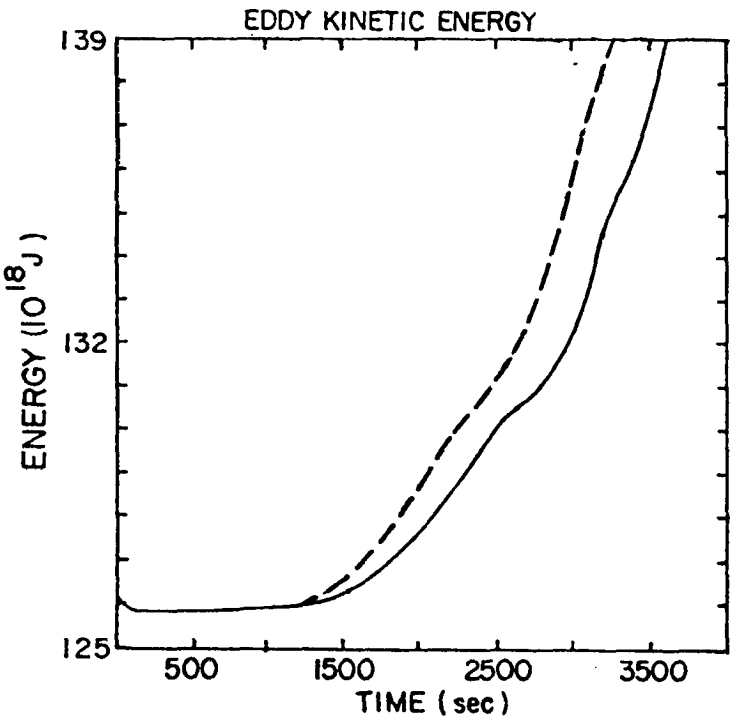

Fig. 5.17: Eddy kinetic energy for Set B.
dashed line: 300 CCN cloud B-1R
solid line: 1000 CCN cloud B-2R

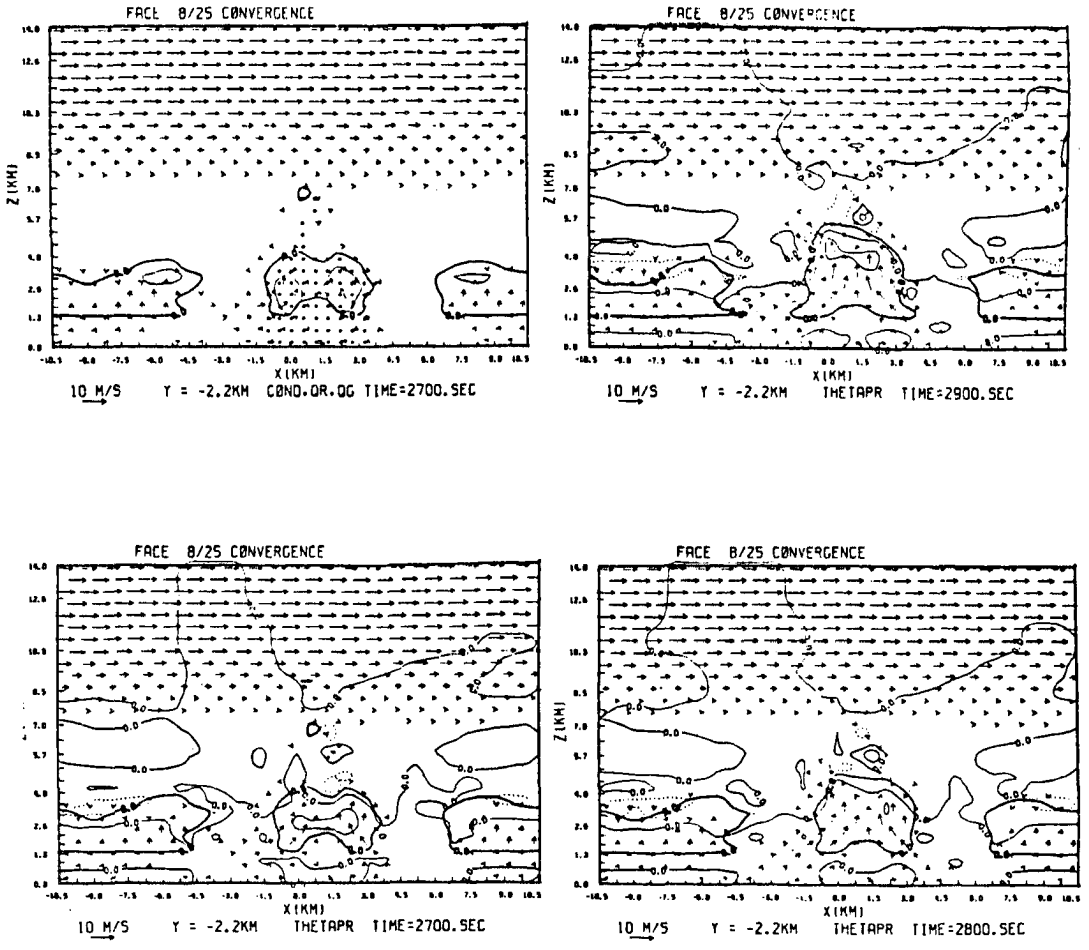

Figure 5.18: Convergence of flow from upper dissipating "cut off" tower (for B-1R cloud).

hitting the ground). At 3600 s with vigorous ice phase processes aloft the low further deepened reaching surface values of -0.35 mb. However, just under cloud base at the precipitation flank values were higher (-0.04 mb to -0.06 mb) and the low center expanded to the east and west at the surface. Figs. 5.19 a and b show the pressure field.

In summary, the low CCN cloud of Set B bears resemblance to the clouds observed at the first phase of convection on that day and radar reflectivities of this simulated cloud are in good agreement with the observed ones (Cunning, personal communication). The mixing ratios for cloud water are in good agreement with the measurements, but rain and graupel mixing ratios are higher than the measured ones (Hindman, personal communication). Though observed in-cloud pressure was not analyzed, the simulated cloud pressure field is in agreement with previous estimates and simulations (Barnen, 1970; Schlesinger, 1980; Nehrkorn, 1981). A general vertical distribution of pressure perturbations with positive perturbations opposing buoyancy near cloud top and low pressure at low levels is simulated.

The lowest simulated surface pressure perturbation of -0.36 mb is the same as that measured by Cunning and DeMaria (1981). It was not, however, brought about by seeding aloft as was hypothesized by Cunning and DeMaria.

b. Run B-1NI - the ice phase role

In order to explore the role of the ice phase on the surface pressure and the dynamics of the cloud, experiment B-1R was repeated without any ice phase processes. This accounts also for the possibility that the simulated cloud was "naturally seeded."

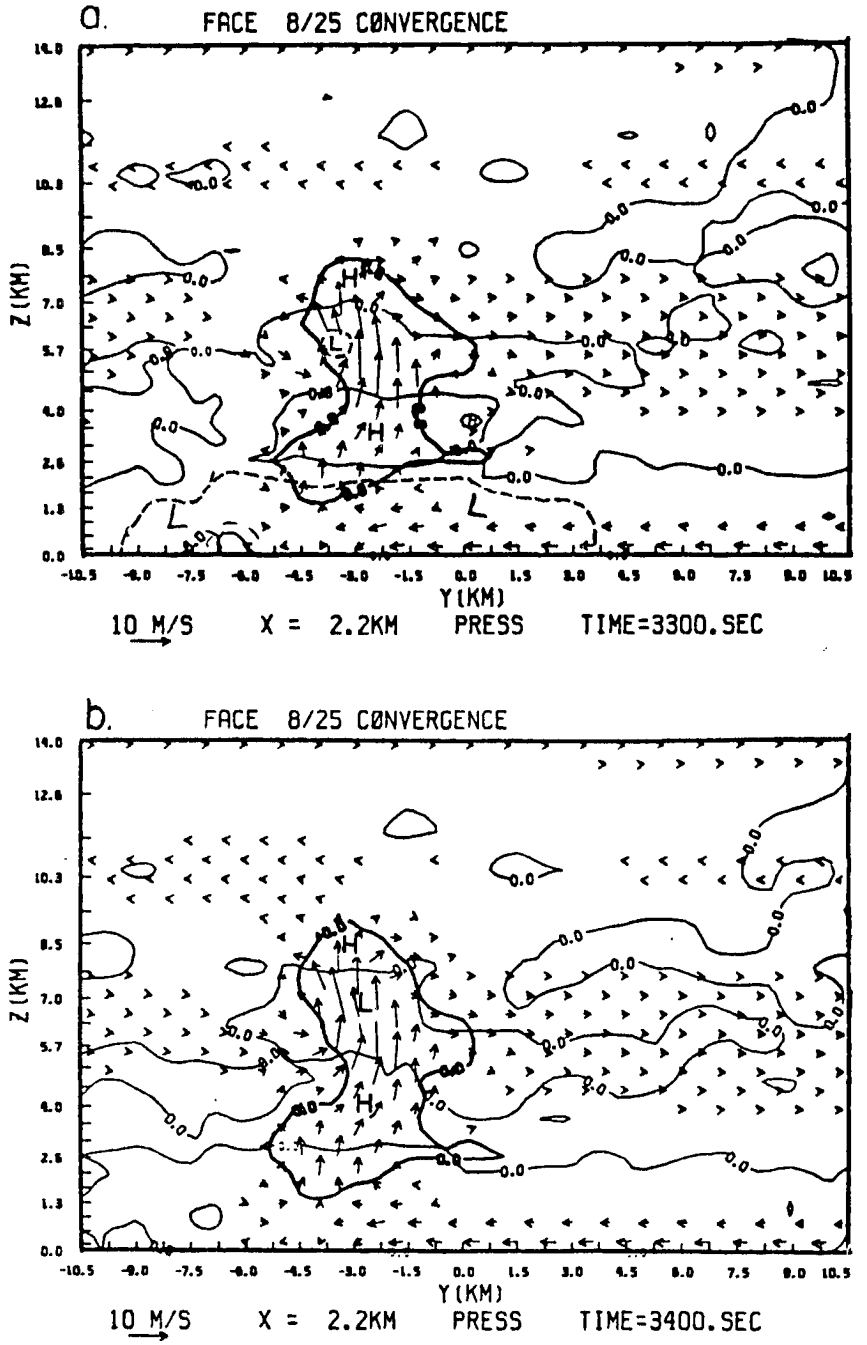

Figure 5.19: Vertical cross section showing vertical perturbation pressure field for Set B. Low CCN cloud (B-1R). Contours as in Fig. 5.2.

Elimination of the ice phase processes resulted in a less vigorous storm. The kinetic energy was lower by 45% in the absence of the ice phase. The maximum vertical velocities of B-1R were higher by 9-10 ms^{-1} at the time in which vigorous ice phase processes were going on (3300 s). Updrafts, however, were weaker at earlier times. Precipitation from B-1NI decreased drastically from 83 x 10^9 (for B-1R) to 68 x 10^6 (for B-1NI). This, it will be shown, is the same order of magnitude yielded by the modified high CCN cloud B-3R. A considerable portion of the updraft velocity difference could be, therefore, due to the loading effect and not necessarily due to the release of latent heat. The surface mean pressure field is lower under cloud B-1NI (-0.17 mb) than that under the cloud B-1R (-0.08 mb). However, any possible surface pressure response to the ice phase was masked by the overwhelming effect of the excessive rain. No increase in cloud top height due to the ice phase was seen.

5.3.2 The high CCN cases: B-2

This experiment is identical to B-1R except that the cloud is initiated with 1000 ℓ^{-1} CCN. It was designed to delay warm rain and the precipitation induced higher pressure at the surface, so that surface pressure drops if existing and communicating buoyancy enhancement aloft, would be more pronounced. It was designed also to explore the relative importance of water loading effects vs. the potential energy gained by lifting more liquid water above freezing level.

a. Run B-2R - the reference run

The high (1000 ℓ^{-1}) CCN cloud corresponds to a continuous CCN seeding of the cloud with the same constant concentration at all levels, or alternatively, to cloud growth in a more continental air

mass. The cloud started, like the low CCN case, as a small tower at the perturbed site, followed by a line of convection along the convergence line. Nevertheless this cloud's evolution is significantly different from that of the lower CCN case as can be generally seen from the three-dimensional plots (Fig. 5.20).

Starting from early stages the cloud appeared to grow faster, both laterally and vertically. This is due to the fact that no conversion of cloud droplets to rain drops took place. The numerous cloud droplets occupy larger volume. The total liquid water content at this stage stayed the same, however. As no conversion to rain water was simulated at all, the effect of water loading was very pronounced and limited drastically the vertical growth of the cloud. Following 2300 s the low CCN cloud began precipitating, hence the water loading decreased in that cloud, which with the release of latent heat of freezing after 3300 s allowed for vertical growth to higher levels. At 1 hour, the top of the low CCN cloud was 4.5 km above that of the high CCN case. In the early stages (1000 s to 1500 s) the vertical growth was approximately 2000 m in 500 s. The vertical growth was in a pulse-like fashion. The horizontal growth and the growth along the convection line were significant. With progressing time, more condensation occurred and the growth rate accelerated - mainly laterally. The potential temperature field exhibited negative anomalies near cloud top representing entrainment and dry adiabatic cooling while positive perturbations representing condensational warming existed at lower levels. Starting at 1900 s (see Fig. 5.21) lateral entrainment was evidenced by negative temperature perturbations at the sides. The flow pattern suggests that the cloud entrained higher level return

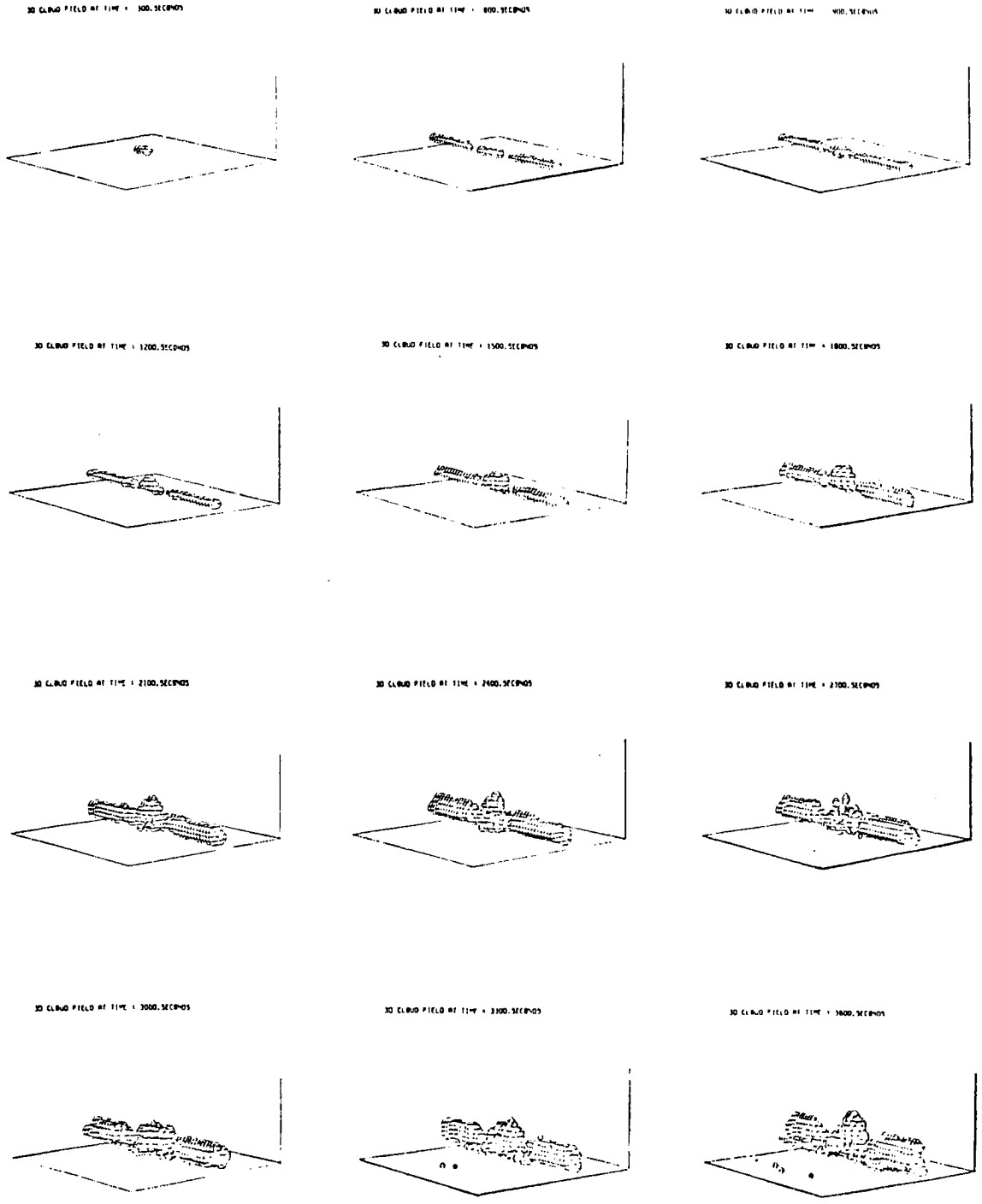

Figure 5.20: 3-D plots for 1000 CCN (B-2R).

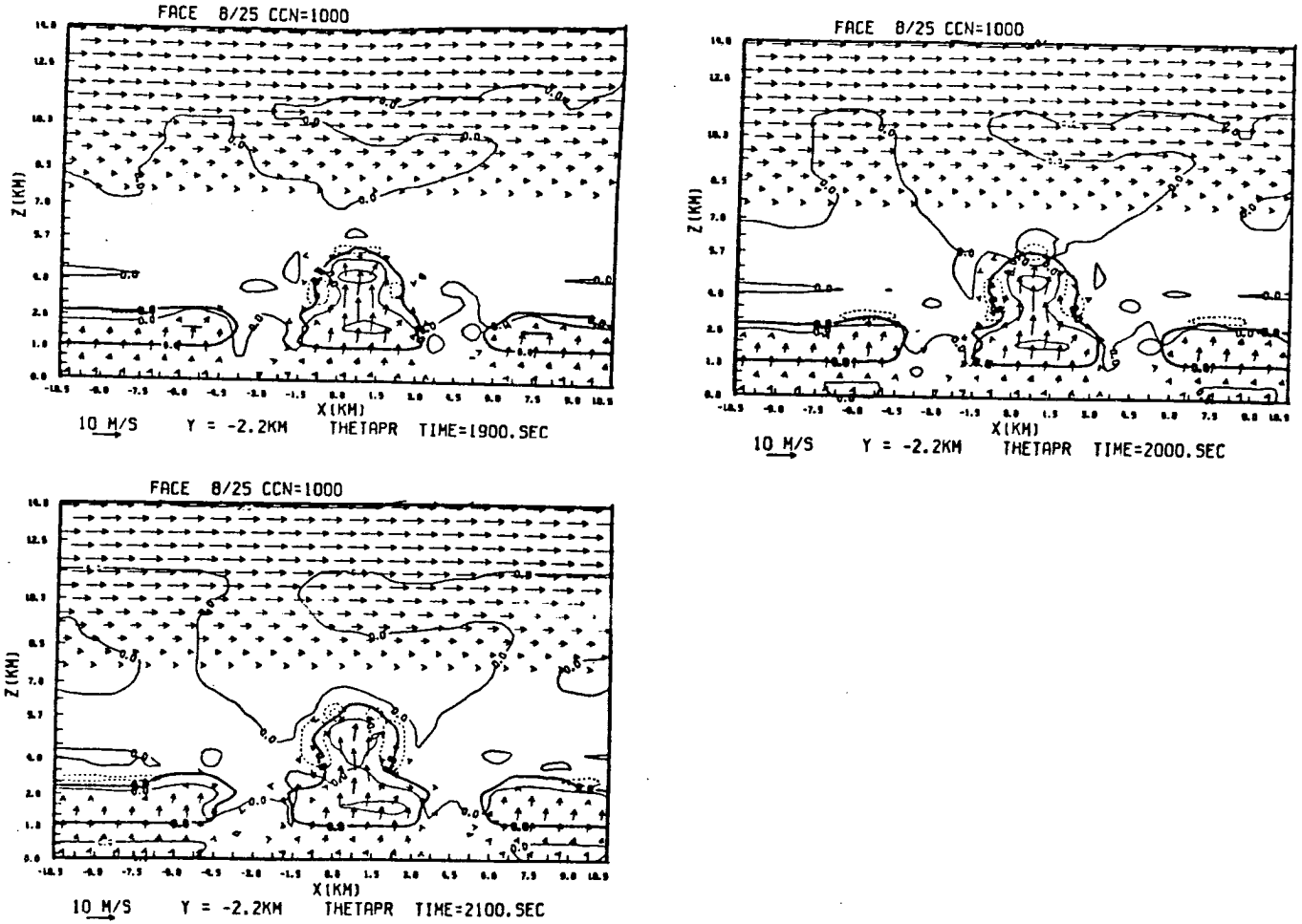

Figure 5.21: Set B high CCN cloud B-2R temperature field showing top and lateral entrainment. Solid lines are positive perturbations, dotted lines are negative perturbations. Contouring intervals of 1°C used.

flow air and not environmental air laterally. Starting at 2000 s cooling was seen near the convection line top. Fig. 5.22 showed the evolution of the return flow entrainment leading to a "cut off" cloud. Updrafts with maximum values of 10.2 ms^{-1} appeared as early as 1700 s at a height of 2 km. Later on, updraft velocities grew even more to a peak value of 15.1 ms^{-1} at 3600 s (at 6.3 km). However, this value is still lower than the peak updraft values (21.2 ms^{-1}) at the same time in the low CCN cloud. As the cloud's vertical growth was limited, downward motion was confined to lower levels and bears a different structure than that of B-1R as shown in Fig. 5.23. Downdrafts formed in the middle of the tower and actually split the updraft, whereas in B-1R downdrafts surrounded the main updraft. The loading force right in the center of the tower became so strong that a downdraft was initiated at the location of the highest liquid water content. Maximum downdraft values were lower by 1.2 - 3.0 ms^{-1} greater with a maximum value of 7.1 ms^{-1} aloft (at 3600 s) and 0.6 ms^{-1} near the surface. This near surface value was lower than that of B-1R, reflecting the lack of precipitation evaporative cooling and drag. The environmental potential temperature profile (Fig. 5.13) changed in a way similar to that of the low CCN case and so did the turbulent kinetic energy (Fig. 5.17). The general cloud pressure field was very similar to that of the low CCN case (B-1R), with positive perturbations near cloud top and negative pertubations at lower levels.

The subcloud surface pressure field at early stages (900 s) exhibited a negative pertubation (0.06 mb) centered below the perturbed bubble. This negative pertubation spread to the north. To the

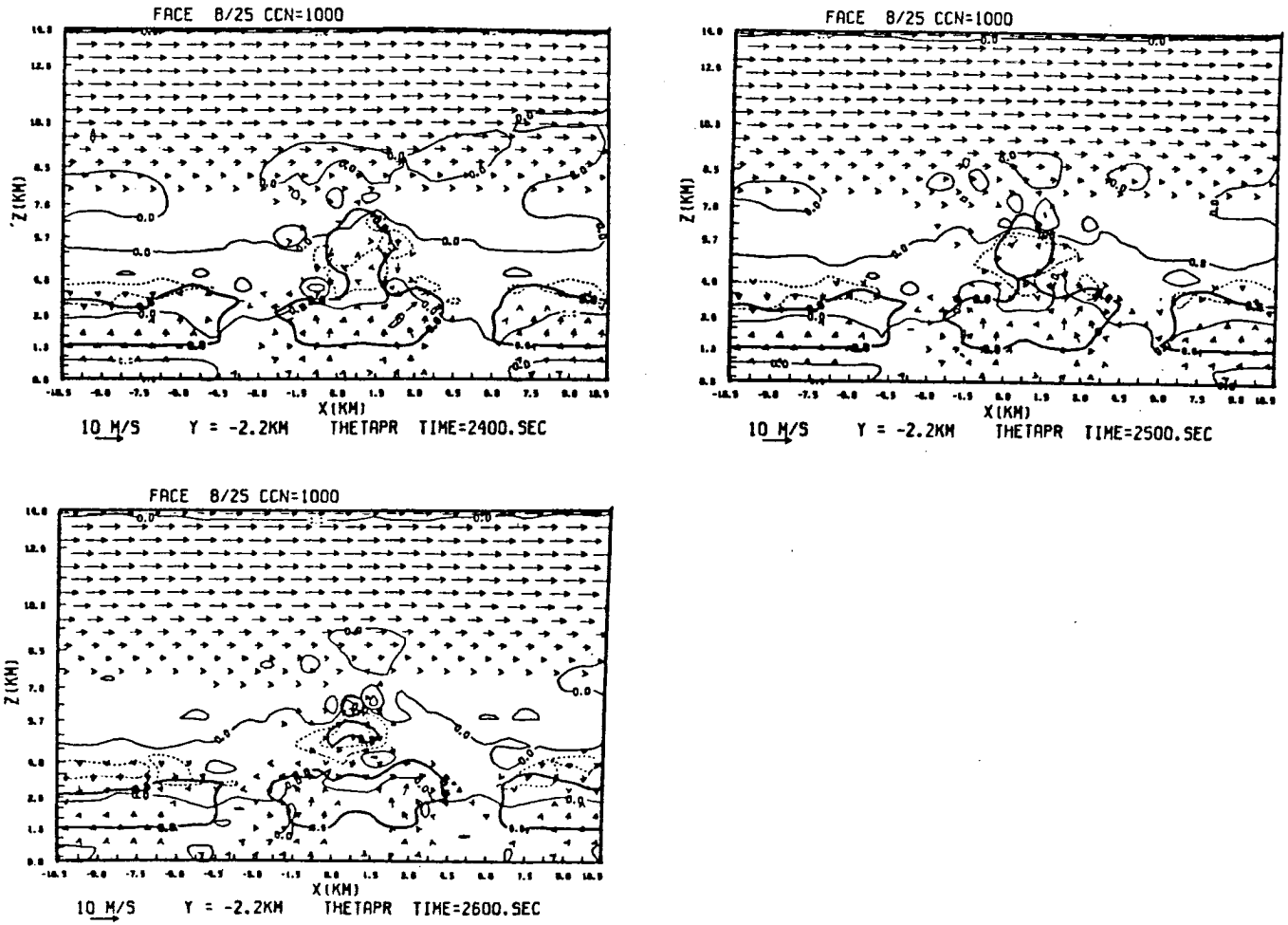

Figure 5.22: "Cut off" tower of the high CCN case B-2R caused by entrainment. Contouring as in Fig. 5.21.

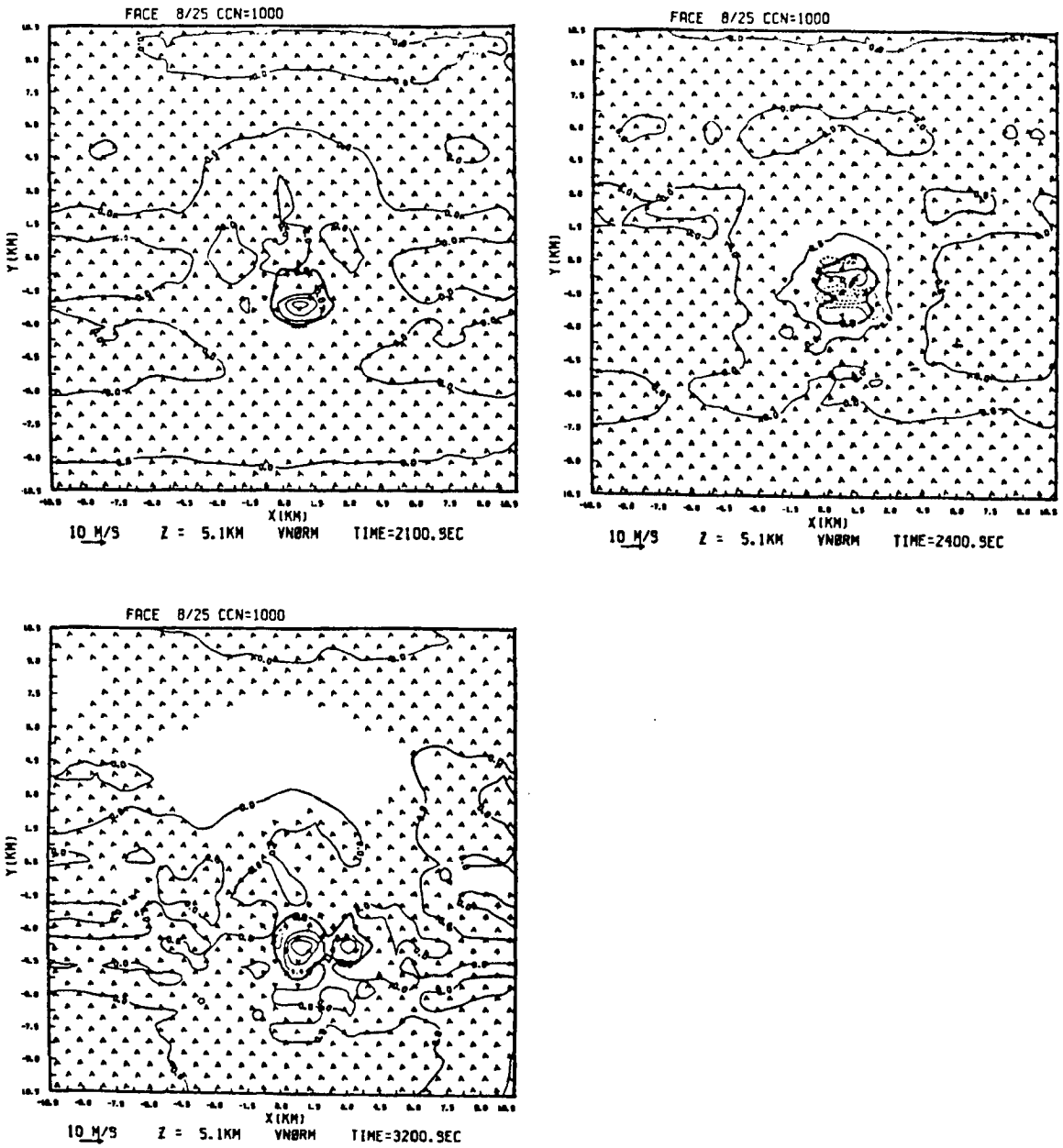

Figure 5.23: Downdraft structure for the high CCN cloud (B-2R). Contouring as in Fig. 5.13.

south, east and west slight positive (0.01 - 0.03 mb) perturbations existed. At 1800 s the low deepened (peak surface negative pertubation of 0.19 mb) and expanded with different intensities to cover all the subcloud layer. At 3600 s, with no ice phase processes aloft and no rain on the ground, the lowest surface negative perturbation was 0.32 mb. The minimum perturbation at that time for B-1R was -0.36 mb. The relative significance of the gain in liquid water due to the delay of precipitation by high CCN number versus the loss of liquid water above seeding level ($-10^{o}C$) due to the loading effect was achieved by integration of total water above the $-10^{o}C$ isotherm. Though the total liquid water content of the high CCN cloud was higher at the end of 1 h none of this water was present above the seeding level.

b. Run B-2S - the seeding response

Starting at 3600 s when cloud water reached the seeding level the cloud was seeded by adding 100 crystals ℓ^{-1}. At that time the simulated cloud did not have any rain water. Keep in mind that the current version of the model does not simulate aggregation processes that can accelerate the growth rate to precipitation size particles. The changes described herein are the dynamic properties at the lowest seeded volume (height of 6624 m) 900 s and 1800 s after seeding started. The absence of rain water significantly slowed the response.

The potential temperature increased very slowly. After 900 s of seeding the average temperature of the seeded volume rose by $0.01^{o}C$ with maxima of $0.25^{o}C$ at some locations. Fifteen minutes later, the temperature rose, on the average, by $0.3^{o}C$ more with increases of up to $1.45^{o}C$ at preferred locations. The vertical velocity decreased first by an average of 0.12 ms^{-1} (at 4500 s) and then increased

slightly by an average of 0.4 ms^{-1} (at 5400 s). With such slight changes in vertical velocities, changes in eddy kinetic energy were barely detectable -- less than 0.5%. Ice appeared at the seeded volume following seeding and the cloud water mass increased. In the absence of rain water and aggregation processes graupel particles did not form even after 30 minutes of seeding and the cloud was void of precipitation size particles. After 900 s of seeding an average pressure drop of 0.03 mb in the lowest seeded volume was simulated. Nine hundred seconds later the pressure dropped by 0.14 mb. The subcloud pressure field behaved as follows: At 4500 s the surface pressure (lowest 500 m) below the seeded volume dropped by 0.02 - 0.03 mb, while a slight increase was seen above that level. At 5400 s a drop of 0.15 mb in the subcloud layer from the surface and up to a height of 1.7 km was simulated.

In summary, the response of cloud B-2 to seeding was very weak. In the absence of supercooled rain drops seeding resulted in the freezing of cloud droplets only. As the mass of a cloud droplet is substantially smaller than that of a rain drop the latent heat released is sufficient to cause significant changes in the dynamics of the cloud. In the absence of aggregation processes cloud droplets cannot grow to graupel particles fast enough, nor can graupel particles form.

5.3.3 The modified high CCN case (0 threshold)

The results of experiment B-2S led to this experiment. This experiment actually introduces raindrops at and above seeding level and thus is designed to explore the response to seeding of a continental cloud containing raindrops at high levels.

a. Run B-3R - the reference run

The modified high CCN cloud is identical to the high CCN case at the first hour of simulation. However, at the -10°C level the cloud to rain autoconversion threshold is set to be zero to force conversion of cloud droplets to rain at high levels.

The cloud grew explosively, both in the main tower and in the convection line to the west of the main tower, starting at 3700 s with the release of latent heat of freezing of rain drops. At 5200 s the main tower and the west line of convection merge to one system. Fig. 5.24 shows three-dimensional plots of the system. The peak mixing ratio for rain water at the -10°C level at 3800 and 3900 s, was 6.34 g kg^{-1} and 5.15 g kg^{-1}, respectively. The average mixing ratio for rain at that level over the center of the main tower was only 0.46 g kg^{-1}. Rain water was distributed in pockets rather than in a homogeneous way. This can be a reflection of resolvable eddies causing dried areas of low liquid water in the neighborhood of high liquid water areas.

The cloud gained its highest perturbation temperature (3.4°C) and positive buoyancy at 4000 s (height of 7.7 km), with the release of latent heat of freezing rain drops. This was accompanied by maxima of graupel mixing ratios and followed by a peak updraft velocity of 24.8 ms^{-1} at 4100 s, a value which is higher by 8.8 ms^{-1} than the maximum updraft velocity of B-2R. Pockets of significant crystal ice concentrations (exceeding 1 g kg^{-1}) were apparent at higher levels (above 10.3 km), but the ice crystal concentrations on the average were very low. Vertical growth rate are higher than that of the B-2R cloud by 7.9 ms^{-1} and is ~23 ms^{-1}. The potential temperature and

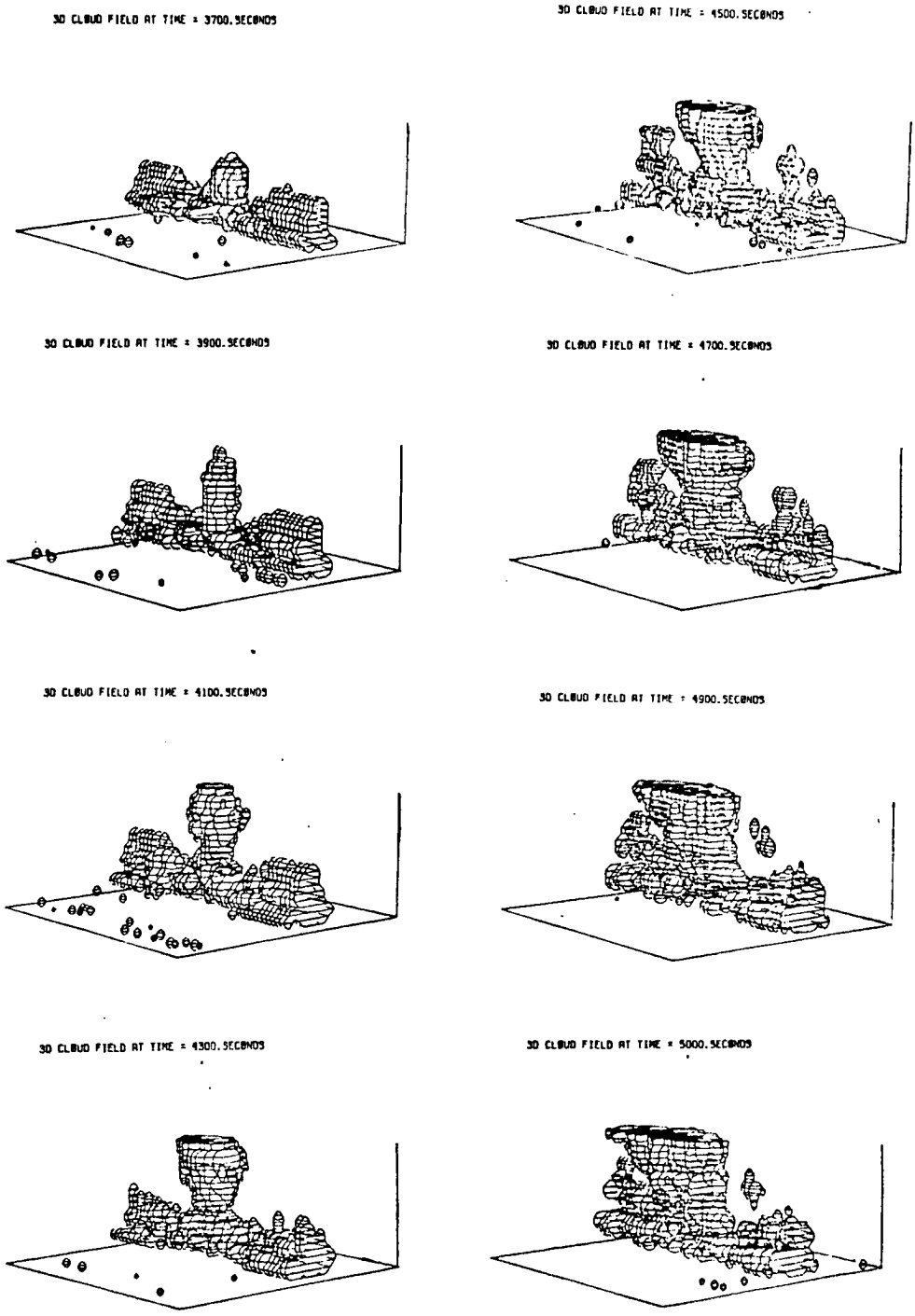

Fig. 5.24: 3-D evolution of the modified high CCN cloud B-3R between 3700-5000 s.

vertical velocity fields at a height of 7.0 km are shown in Fig. 5.25. Cloud growth between 3700 s and 4200 s is shown in Fig. 5.26. The potential temperature perturbation field indicates top entrainment with ambient air starting at 4000 s as well as mid-levels' air entrainment both at the upshear and downshear (wake effect) sides. This mid-levels entrainment caused drying of parts of the cloud (see Fig. 5.27). With first precipitation hitting the ground (at 4400 s) some evaporative cooling was evident near the surface at the downdraft area, but it was not before 4700 s that the temperature at the surface dropped by $0.5^{o}C$. Maximum updraft velocities reached 25.6 ms^{-1} and started as a main centered circular updraft surrounded by downdrafts. Later the main updraft divides into two cores with downdrafts in between (see Fig. 5.28). The maximum downdraft magnitude was 21.2 ms^{-1} aloft and 2.1 ms^{-1} near the surface.

The cloud pressure field exhibited a low pressure near cloud base, and a high pressure above it between 1.7 km and 4.0 km. At mid-levels (4.5 km - 7.0 km) a low capped by the cloud top positive pressure perturbation was simulated. The mid-level low expanded downwards and upwards to a height of 12 km with time, filling gradually and turning within 1000 s to a positive perturbation field. The deepest cloud low was -0.27 mb at mid-levels and the highest cloud high was 1.51 mb near the cloud's top.

The subcloud boundary layer pressure field between 3700 s and 4900 s exhibited a mesolow averaging negative perturbation between 0.12 mb and 0.25 mb with a peak value of 0.59 mb (at 4200 s). At 5000 s the average mesolow filled and a mesohigh was established.

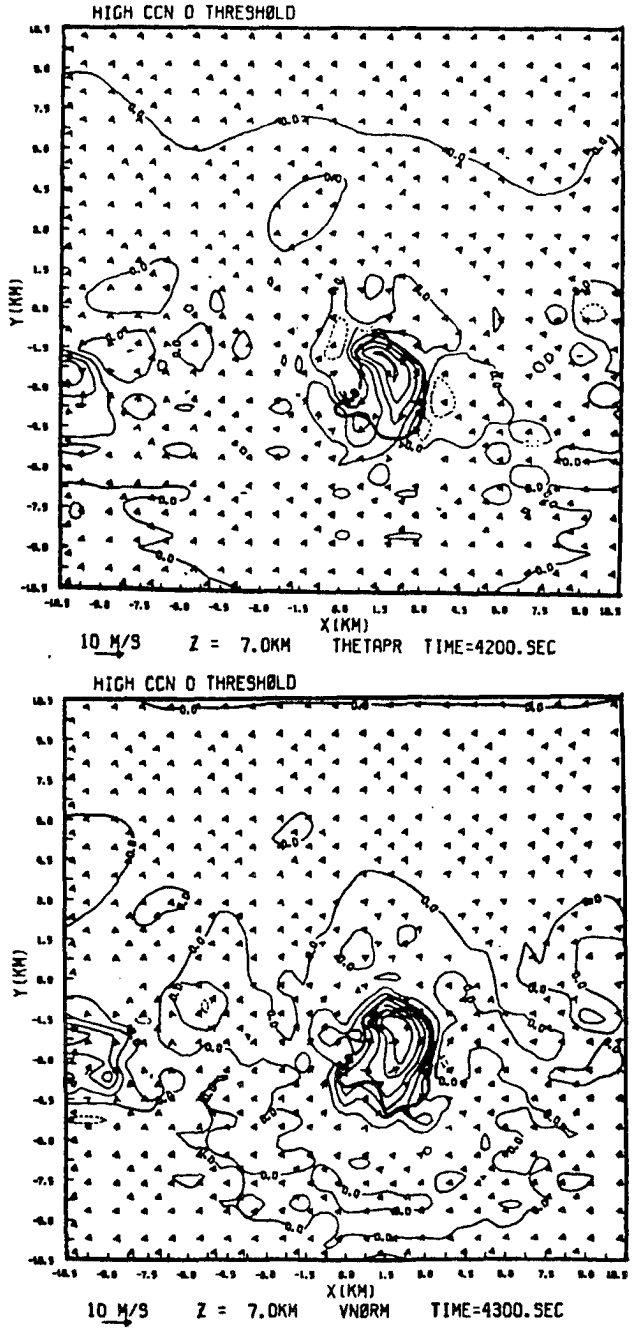

Fig. 5.25: Potential temperature and vertical velocity at z = 7.0 km for the modified high CCN cloud B-3R. Contouring as in Figs. 5.21 and 5.13.

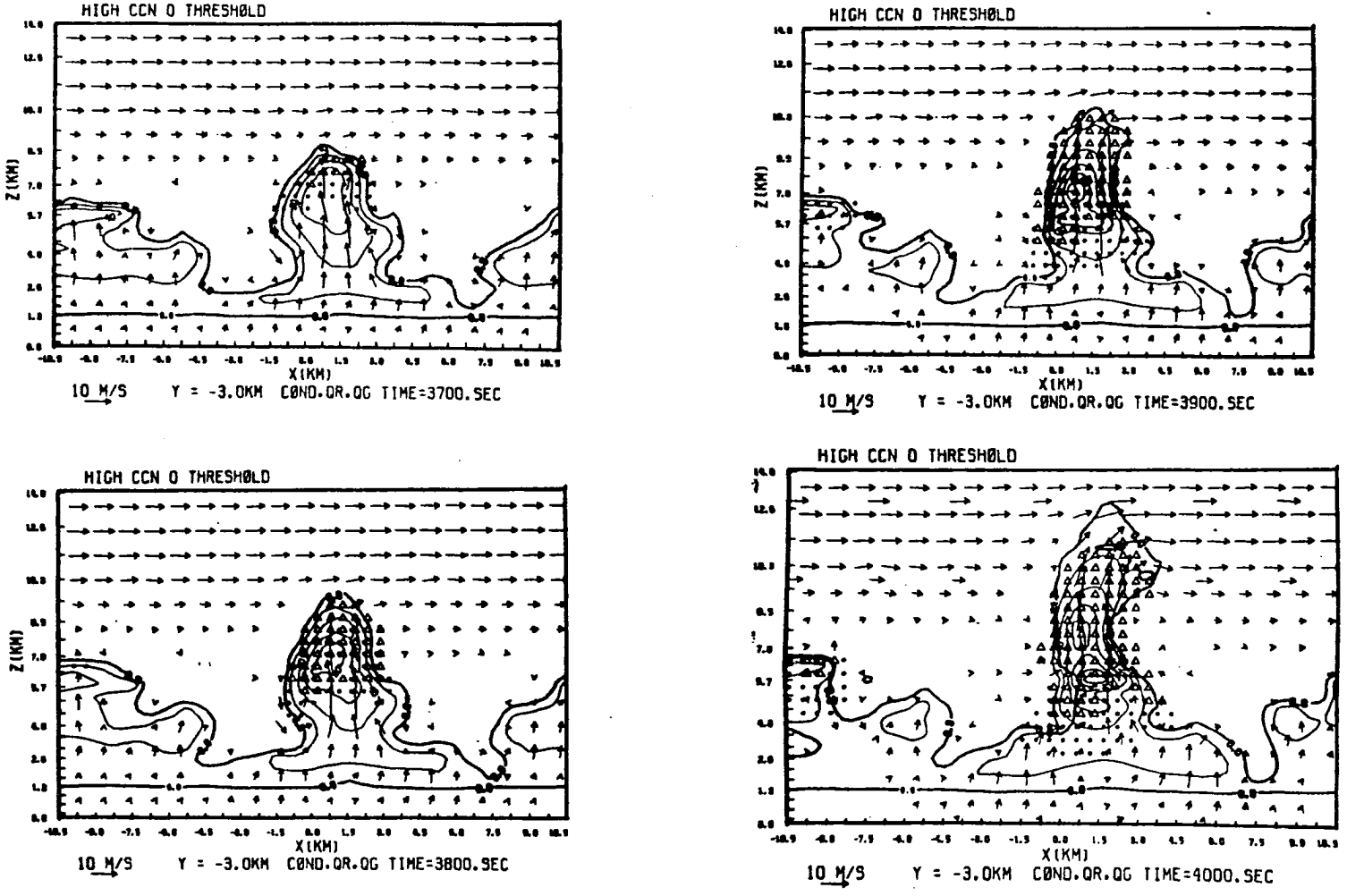

Fig. 5.26: Cloud growth between 3400 s and 4200 s for the modified high CCN case B-3R. Contouring as in Fig. 5.6.

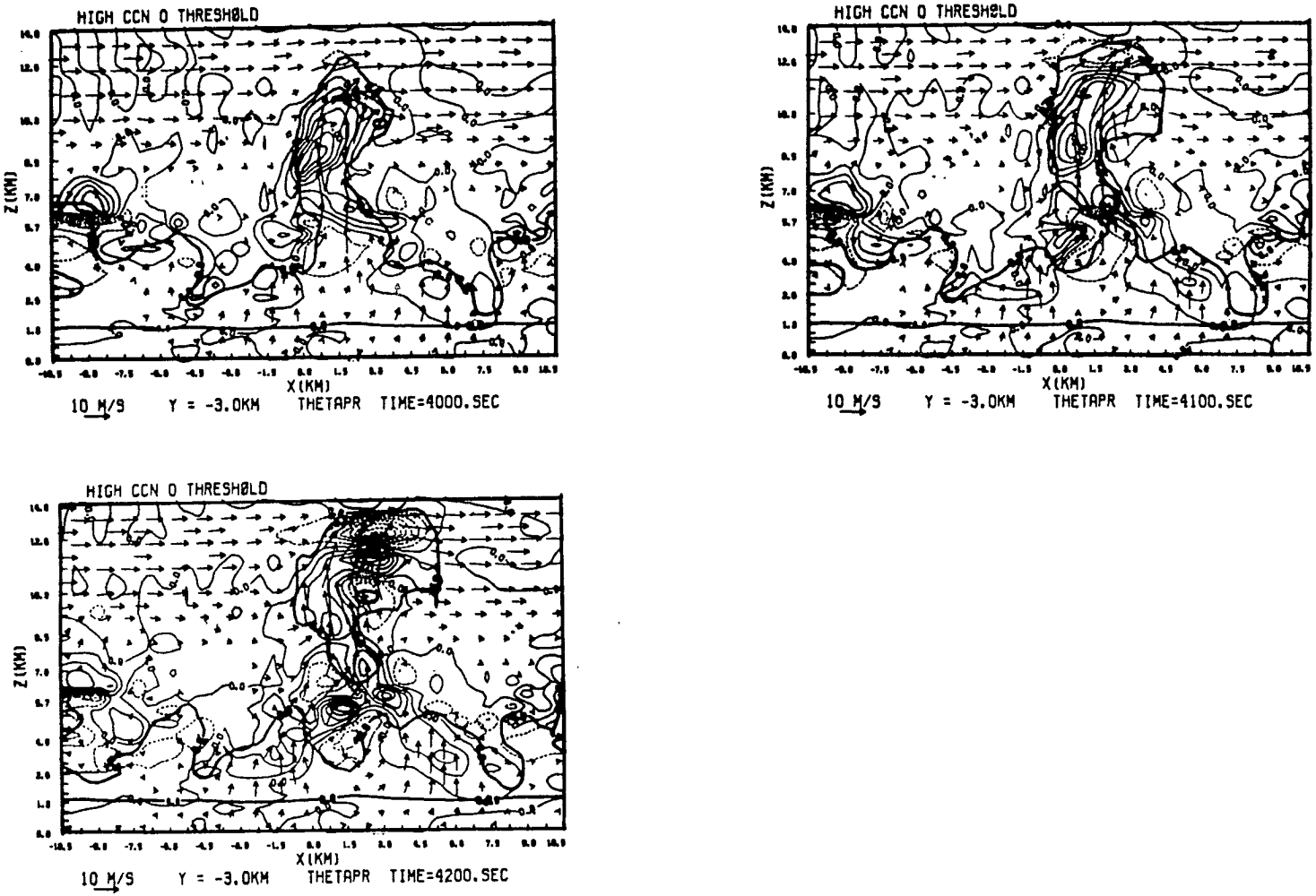

Fig. 5.27: Evolution of top and side entrainment leading to drying of parts of the cloud (B-3R). Contouring as in Fig. 5.21.

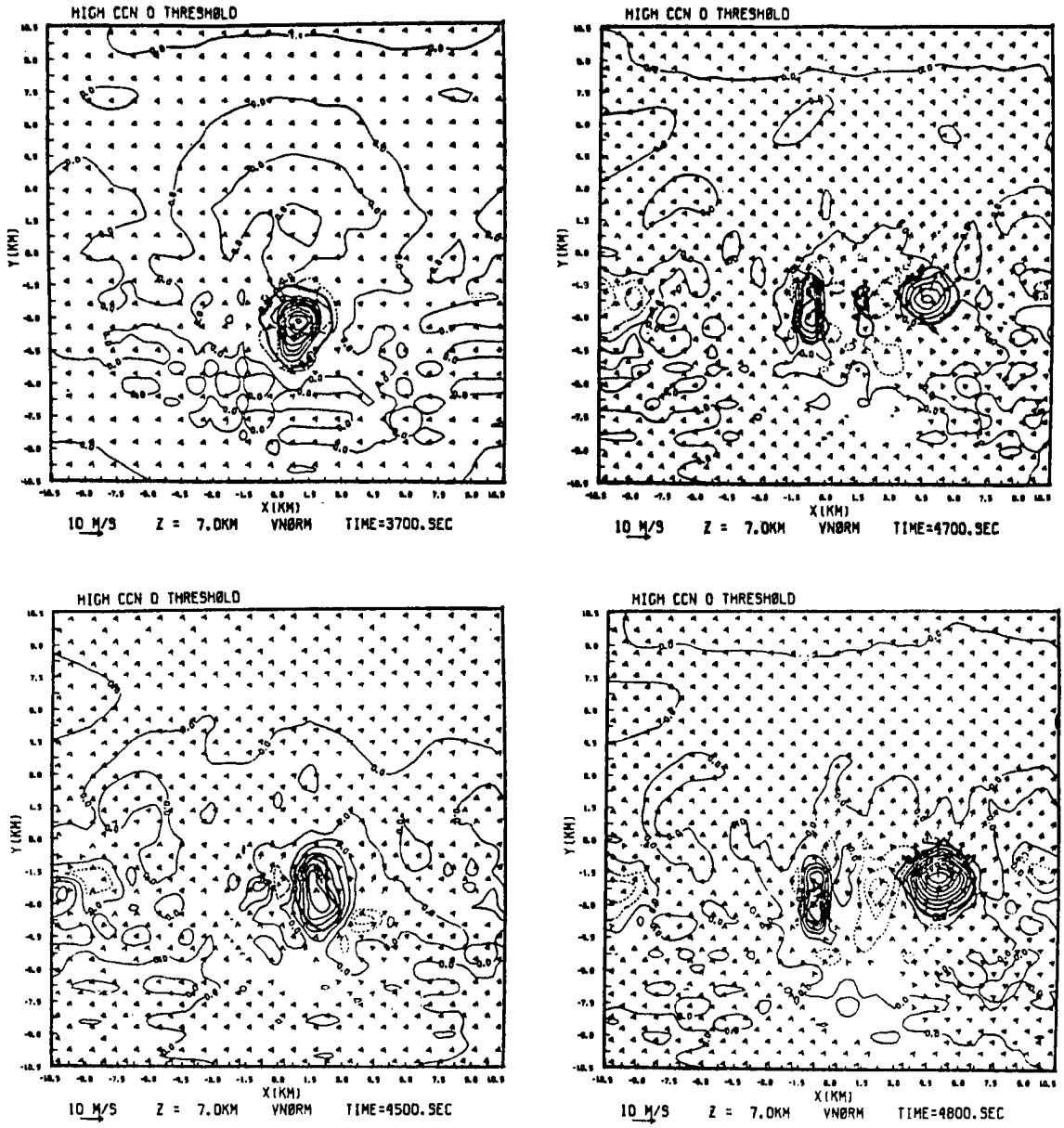

Fig. 5.28: Splitting of the main updraft for the modified high CCN case (B-3). Contouring as in Fig. 5.13.

The variations in CCN counts over south Florida reported by Sax et al. indicate that the initialization of a cloud with high CCN is at least as realistic as initialization with low CCN. The modified high CCN cloud of Set B also has rain water mixing ratios that are higher than the measured ones but the sporadic distribution of high liquid water pockets seems to be in agreement with those measurements (Hindman, personal communication).

b. Run B-3S - the seeding response

Starting at 3600 s and until 4200 s the cloud was seeded by 100 ℓ^{-1} IN. The changes described here are in the properties at the lowest seeded level (height of 6624 m) 300 s and 600 s after seeding started. The potential temperature rose by up to 1.74°C right at the center of the seeded volume at 3900 s, but only by 0.08°C when averaged over the seeded volume. By 4200 s most liquid water had glaciated and entrainment below the updraft began. The average potential temperature at the seeded volume dropped by 0.15°C and the air at that level and at that time was negatively buoyant. The vertical velocity associated with the temperature buoyancy was higher by 2.7 ms^{-1} (at 4100 s) reaching a value of 25.9 ms^{-1} at a height of 10.3 km. The overall maximum vertical velocity was higher in the seeded case by 0.3 ms^{-1}, however. A seedability of 300 m was simulated. The eddy kinetic energy constantly rose in both the reference and seeded runs. After seeding the energy rose slightly by less than 1%. From 4600 s and until the end of the simulation at 5000 s the kinetic energy rises faster as illustrated in Fig. 5.29.

Until seeding stopped at 4200 s the downdrafts of the seeded run are about the same or slightly weaker (0.1 ms^{-1}) than those of the

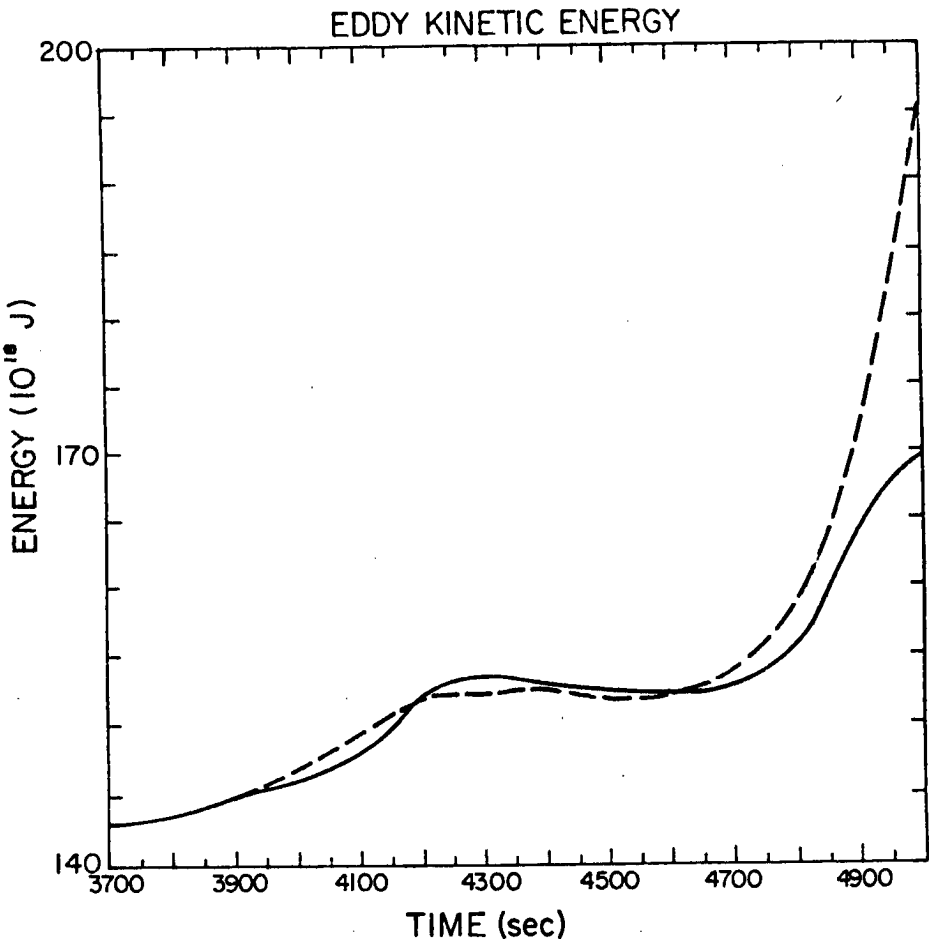

Fig. 5.29: Eddy kinetic energy for the modified high CCN cloud.
solid line - reference B-3R
dashed line - seeded B-3S

reference run. At 4200 s the entrainment below the growing tower was manifested as a downdraft, stronger by 1.4 ms^{-1} at a height of 3.5 km (9.9 ms^{-1}). Near the surface, however, the downdrafts of the seeded cloud was stronger by 0.1 ms^{-1} only. Starting at 4500 s downdrafts were stronger by 0.6 - 5.7 ms^{-1} at high levels and by 0.1 ms^{-1} near the surface. The maximum downdraft velocity was 21.2 ms^{-1} (at 4500 s) aloft (11.3 km), and 2.2 ms^{-1} (at 5000 s) near the surface.

The most pronounced seeding response was simulated in the water mass field. The average mixing ratio for cloud water in the reference run at the area chosen for seeding was 0.65 g kg^{-1} at 3900 s. After seeding, it diminished by 0.12 g kg^{-1} to an average of 0.53 g kg^{-1}, reflecting conversion of cloud water to ice. The rain water, averaging 0.46 g kg^{-1} in the reference run was almost completely converted to graupel and the mixing ratio at that time in the seeded run was only 0.05 g kg^{-1}. The average mixing ratio of graupel rose in the seeded cloud from 0.4 g kg^{-1} to 2.73 g kg^{-1}. At the end of seeding (4200 s), glaciation had already taken place, the availability of liquid water was scarce and changes were less than 0.1 g kg^{-1}. Seeding at that stage was therefore, not beneficial.

The cloud pressure at the levels of seeding started dropping below the reference run's pressure only 300 s after seeding started. The highest drop was 0.06 mb at the highest level of seeding, while at the lowest level of seeding the drop was only half that much. This low started filling immediately and at 4100 s the seeded run's pressure field was higher by 0.05 mb than the pressure of the reference run. The average surface pressure field dropped only by 0.01 mb at 3900 s and 4000 s. After seeding ended (4300 s and on), the pressure

field at the surface under the seeded cloud rose by up to 0.09 mb. The total precipitation from the treated system was lower by 14% than that from the untreated system at the end of 5000 s of simulation as shown in Fig. 5.30. However, both systems were still very active at that time and the slopes of the curves suggest intersection at a later time.

After seeding stopped, at 4000 s an increase of 2.0×10^{-4} s^{-1} in the mesoscale average convergence at a height of 2.6 km was simulated. This is a value which is 25% of the convergence increase measured by Cunning and DeMaria and is simulated at a higher level and not at the surface.

In summary, the introduction of rain water at the level of seeding in B-3S intensified significantly the dynamical response to seeding of that cloud. The freezing of more liquid water resulted in stronger updrafts, more warming and release of latent heat, more entrainment and intensification of mid- and upper levels downdrafts. Pressure response remained weak and convergence was enhanced at low levels above cloud base. The downdraft intensification communicated very weakly to the surface.

5.3.4 The exaggerated seeding case: Run B-2R vs. B-3S

The possibility exists that due to the perturbation needed to initiate clouds, a marginal cloud cannot form at all. In a sense, then, natural clouds were already "naturally seeded" clouds. To account for that possibility a comparison between the dynamic features of the high CCN case vs. those of the modified high CCN case is done. This represents an exaggerated case of seeding in which a non-precipitating cloud containing only cloud droplets is forced to precipitate and

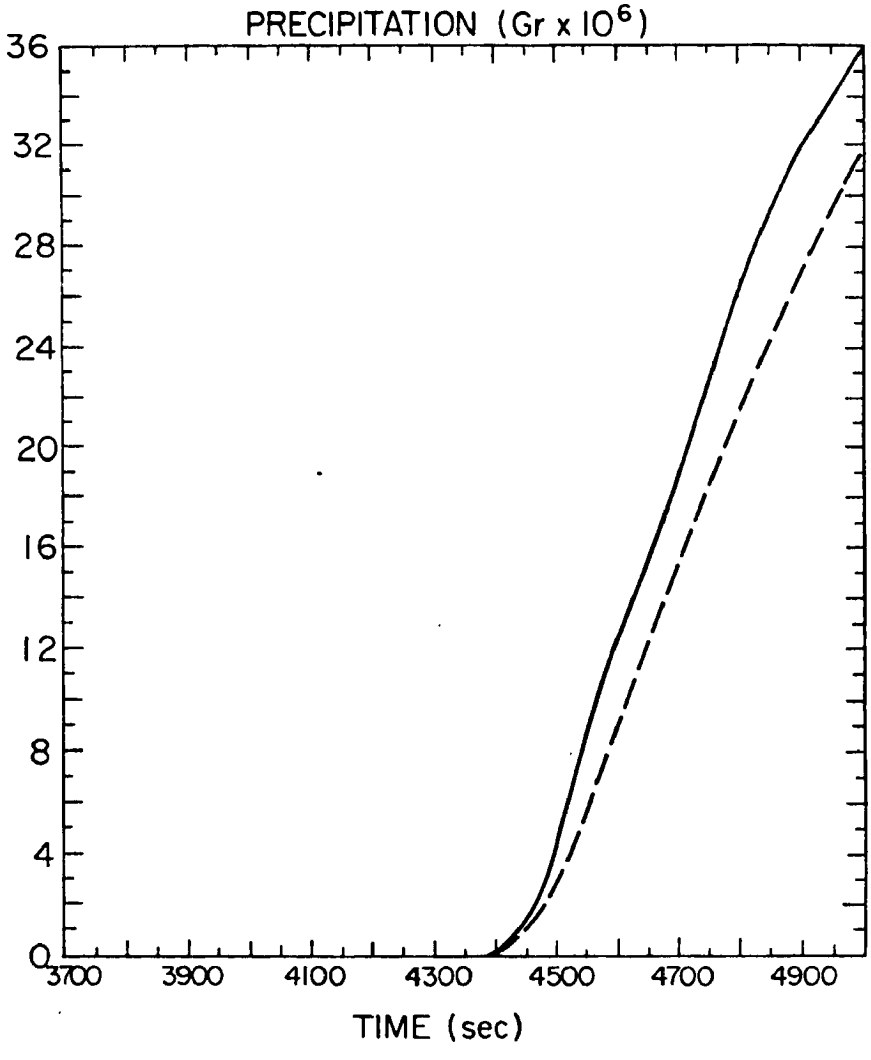

Fig. 5.30: Total precipitation falling from the modified high CCN systems.
solid line - reference B-3R
dashed line - seeded B-3S

produce graupel and vigorous ice phase processes. Comparing those extreme cases, the maximum updraft velocity for B-3S exceeded B-2R by 8.8 ms^{-1} aloft and by 0.2 ms^{-1} near the surface. The maximum downdraft was weaker by 4 ms^{-1} aloft, but stronger by 0.6 ms^{-1} near the surface in the modified cloud. The minimum cloud pressure dropped by 0.26 mb in the modified cloud above cloud base and by 0.16 mb near the surface. This is the same surface value arrived at by "conventional" seeding of that case though the time needed to get that response was longer by 15 min in the "conventional seeding" case. The maximum temperature buoyancy due to the modification was 2.13°C. The seedability between those two cases was 750 m. The exaggerated seeding resulted, then, in low seedability, but in strong modification of vertical acceleration and temperature buoyancy. The pressure dropped moderately at the seeding level. The communication of pressure falls and modified downdrafts to the surface remained on the same order of magnitude, but were faster in the modified case.

5.4 August 13, 1975: Set C, experiments C-1R, C-1S

This case study day was chosen as one dimensional model simulations predicted high seedability on that day for a narrow range of clouds. It is important to mention that the cloud observed that day was a large cumulunimbus that evolved from a pre-existing convection and the simulated cloud (C-1R), resembels the observed one. However, no marginal cloud was simulated. The experiments are designed, therefore to test the importance of mesoscale moisture modification and to reinforce results from previous numerical experiments concerning cummunication mechanisms.

5.4.1 Experiment C-1: The reference run

The simulated cloud grew at the perturbation site on the convergence line. At low levels lateral growth took place around cloud base. At higher levels the wind shear (see Fig. 4.7) influenced the tower growth resulting in a sheared tower. Fig. 5.31 shows the general three-dimensional evolution of the cloud. It bears a strong resemblance to the actual observed cloud as recorded on the time lapse taken at FOS. At the early stages the predicted cloud growth rate was approximately 2.0 ms^{-1}. At 1000 s this rate doubled and growth accelerated gradually. At 2100 s, with ice first forming, the growth rate further accelerated. The simulated maximum updraft velocity was 17.3 ms^{-1} at 3300 s. The first formation of rain drops was noted at 1600 s at a height of 4.5 km (near cloud top at that time). It is not before 2200 s, however, that rain first hit the ground. The cloud became seedable at 2000 s with graupel first appearing naturally at 2300 s (see Fig. 5.32). Weak descending motion was evident from the early stages of the cloud lifetime with maximum values (2.0 - 5.0 ms^{-1} between 1200 s and 1600 s) at a height of 4.0 km. This is just below the level of minimum equivalent potential temperature (Fig. 5.33). Near the surface downdraft values are 0.5 ms^{-1}. At 2000 s with increasing rainwater and water loading the downdraft magnitude simulated aloft was 7.5 ms^{-1} with no change in surface values. With rain first hitting the ground, near surface downdrafts at the precipitation flank became stronger approaching values of 3.0 ms^{-1} at 3600 s and 3.5 ms^{-1} at 3700 s. The overall maximum downdraft velocity aloft was 12.0 ms^{-1} at a height of 3.5 km at 3500 s. The precipitation flank on the surface was associated with

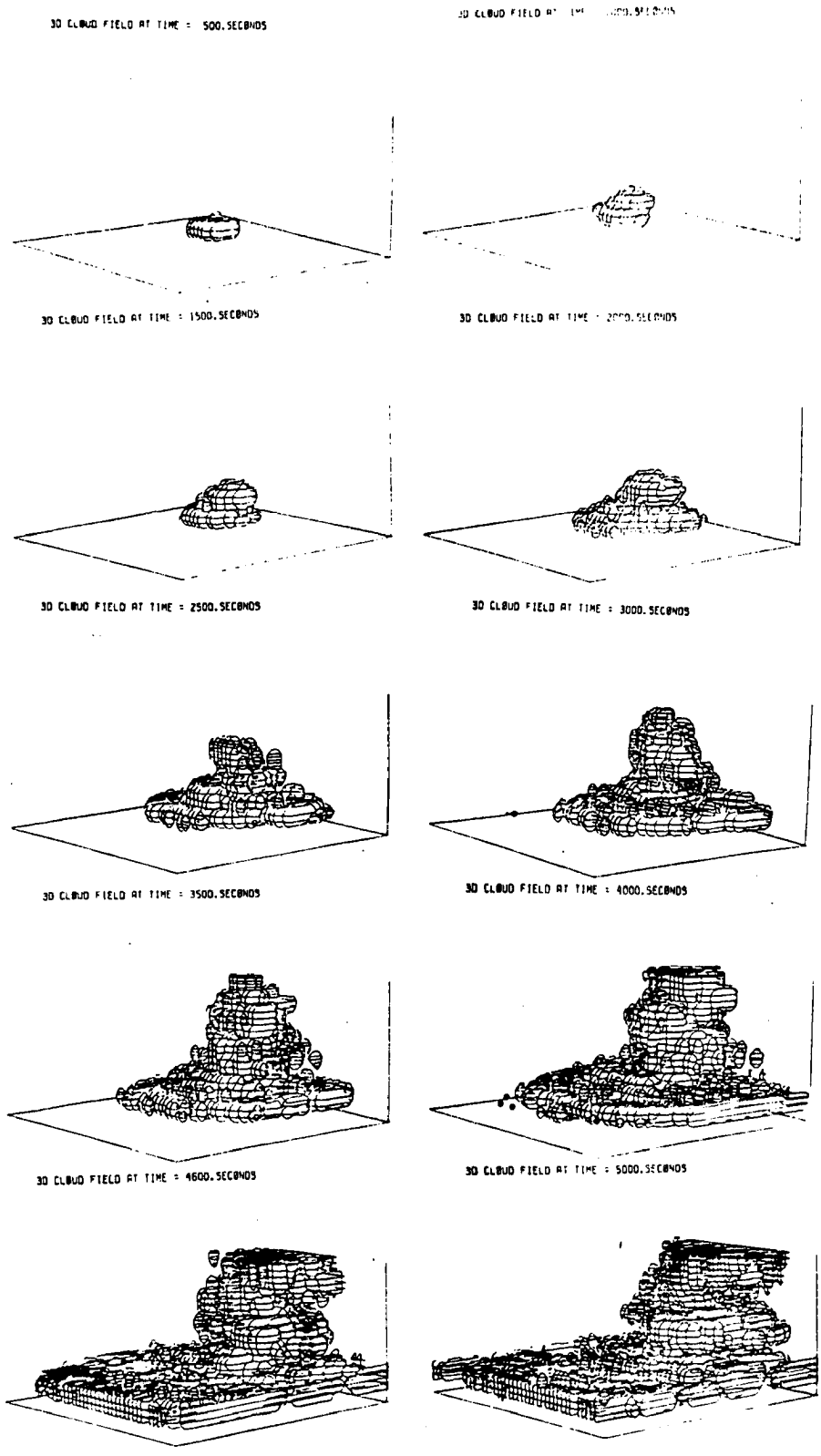

Fig. 5.31: 3-D cloud field for 8.13.75 C-1R.

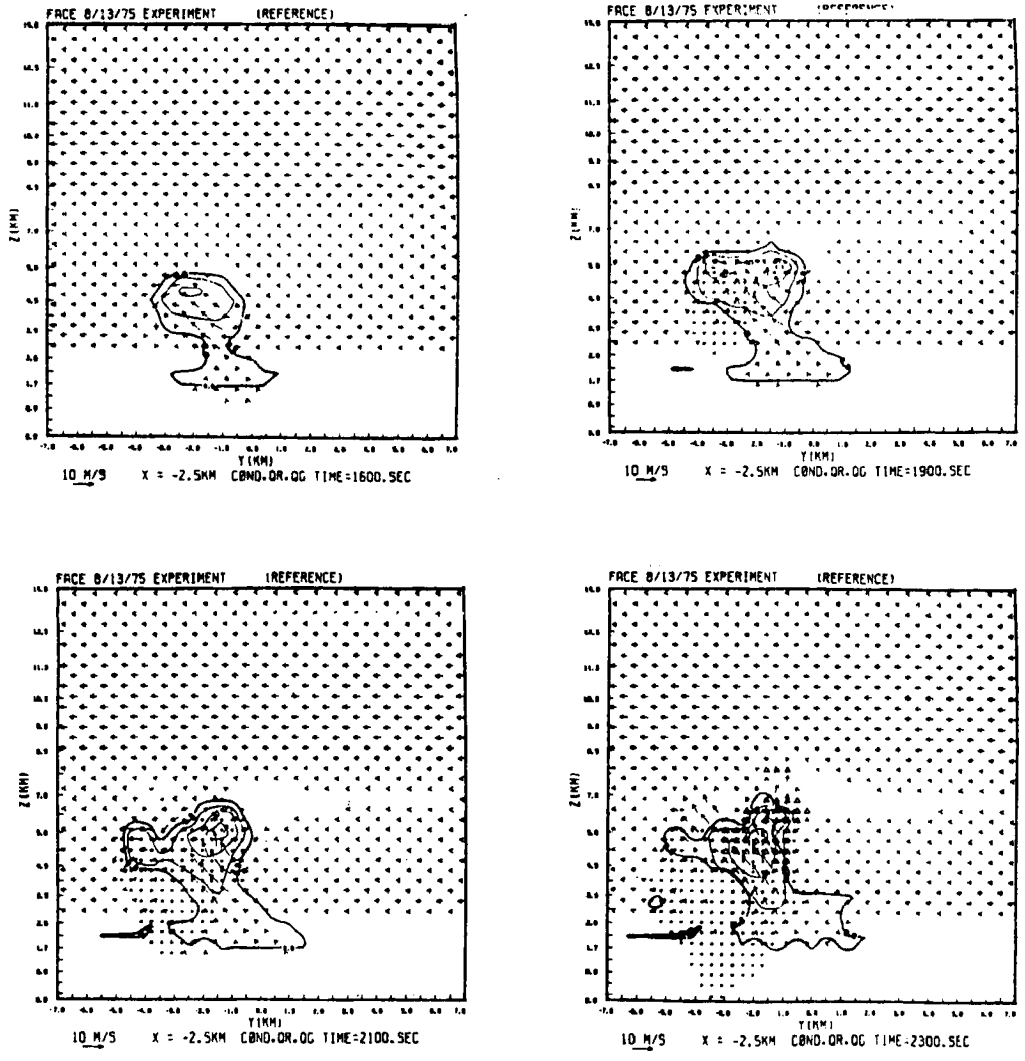

Fig. 5.32: Vertical cross sections showing the 8.13.75 cloud B-3R growth from the time first rain appears till the time first rain hits the ground and first graupel appears. Contours as in Fig. 5.6.

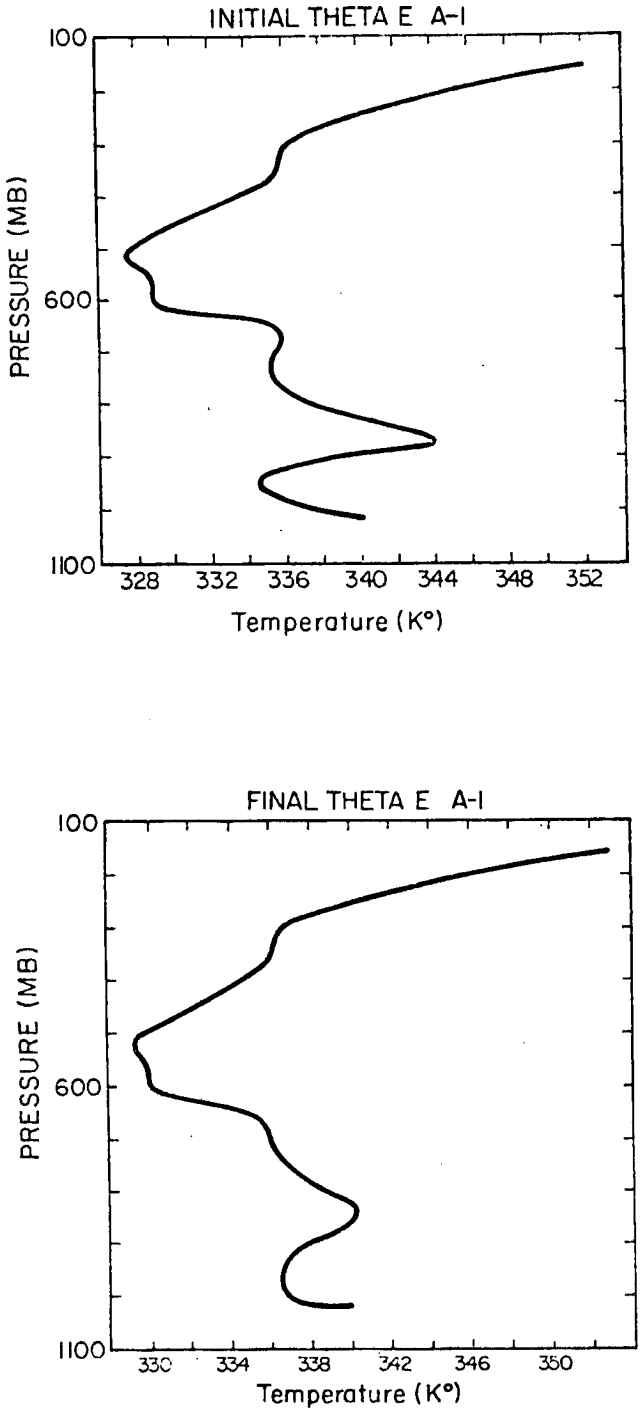

Figure 5.33: Equivalent potential temperature for 8.13.75. Upper: Initial - at the beginning of simulation. Lower: Final - an hour and a half later.

horizontal divergence, negative potential temperature perturbation and local positive pressure perturbation (up to 0.25 mb), as can be seen in Fig. 5.34. Fig. 5.35 shows vertical cross sections at x = -2.5 km at 2800 s and 2900 s in which the cloud outflow circulation is seen to force upward motion into the cloud upon arriving at the surface. Top entrainment as well as side entrainment with both environmental and return flow air were simulated. The structure of updrafts and downdrafts at mid- and upper levels changed with time from a unicore to a multicore updraft with surrounding downdrafts (see Fig. 5.36).

From cloud formation, a slight positive pressure perturbation was established near cloud top associated with cloud top diverging flow. This perturbation had a highest value of 0.19 mb. The lower part of the averaged cloud pressure field had perturbation values of -0.02 mb to -0.2 mb, with strongest perturbations near cloud base, and at mid-levels. The simulated sucloud surface pressure was predominantely low. An average negative perburbation smaller than 0.02 mb was simulated over the domain until 2200 s. At 2300 s, after ice phase processes started, this slight average low deepened by 0.01 mb. The lowest average negative perturbation near the surface was 0.08 mb at 3600 s. The peak negative perturbation at the surface was 0.25 mb at 3600 s and the peak positive perturbation at the surface was 0.53 mb at the same time in the center of the precipitation flank. The shear structure and the storm-induced circulation prevented the fall of precipitation on the inflow flank and helped maintain a long living system.

The simulated cloud (C-1R) resembles very much in shape and evolution the cloud observed on FACE 8.13.75 and its initialization

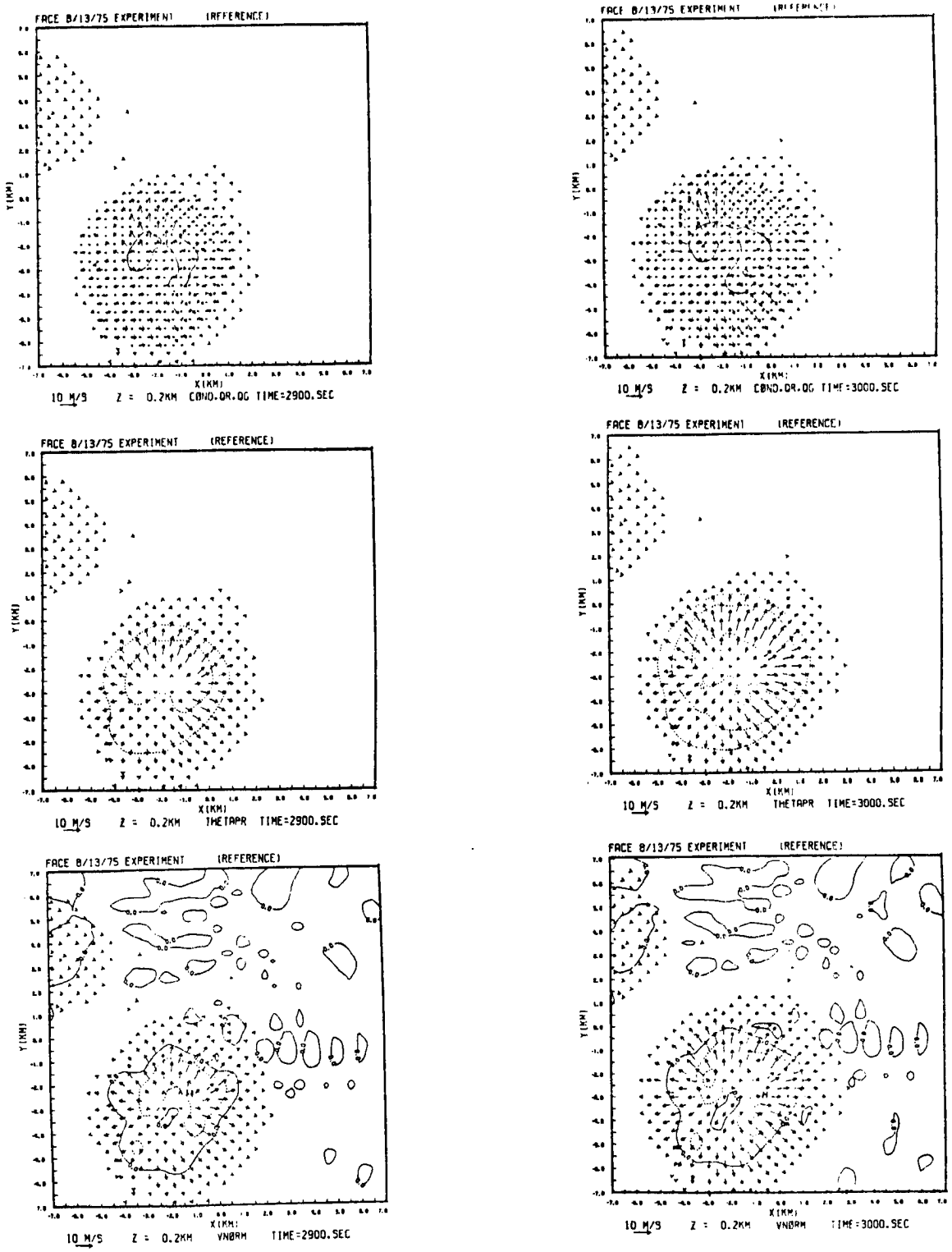

Fig. 5.34: Surface precipitation flank associated with diverging flow downdraft maxima positive pressure perturbation and negative termperature perturbation (for C-1R). Contours as in Figs. 5.6, 5.21 and 5.13.

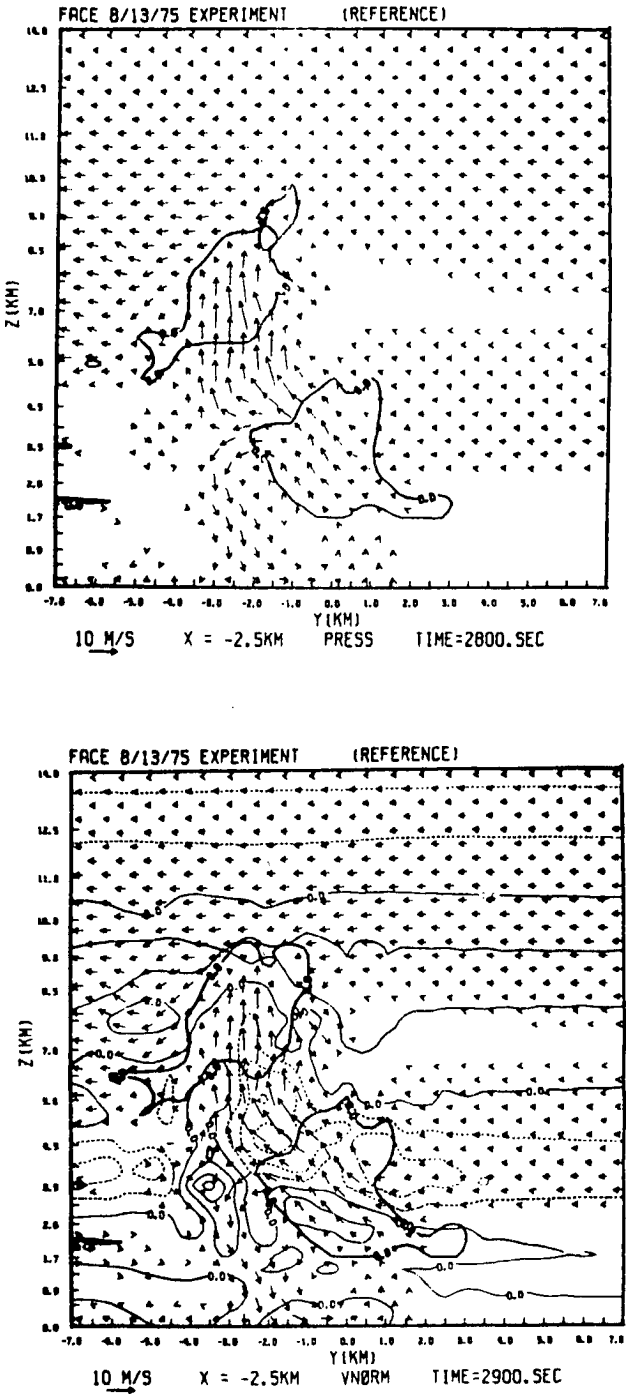

Fig. 5.35: Downdrafts forcing vertical motion upon arriving at the surface.

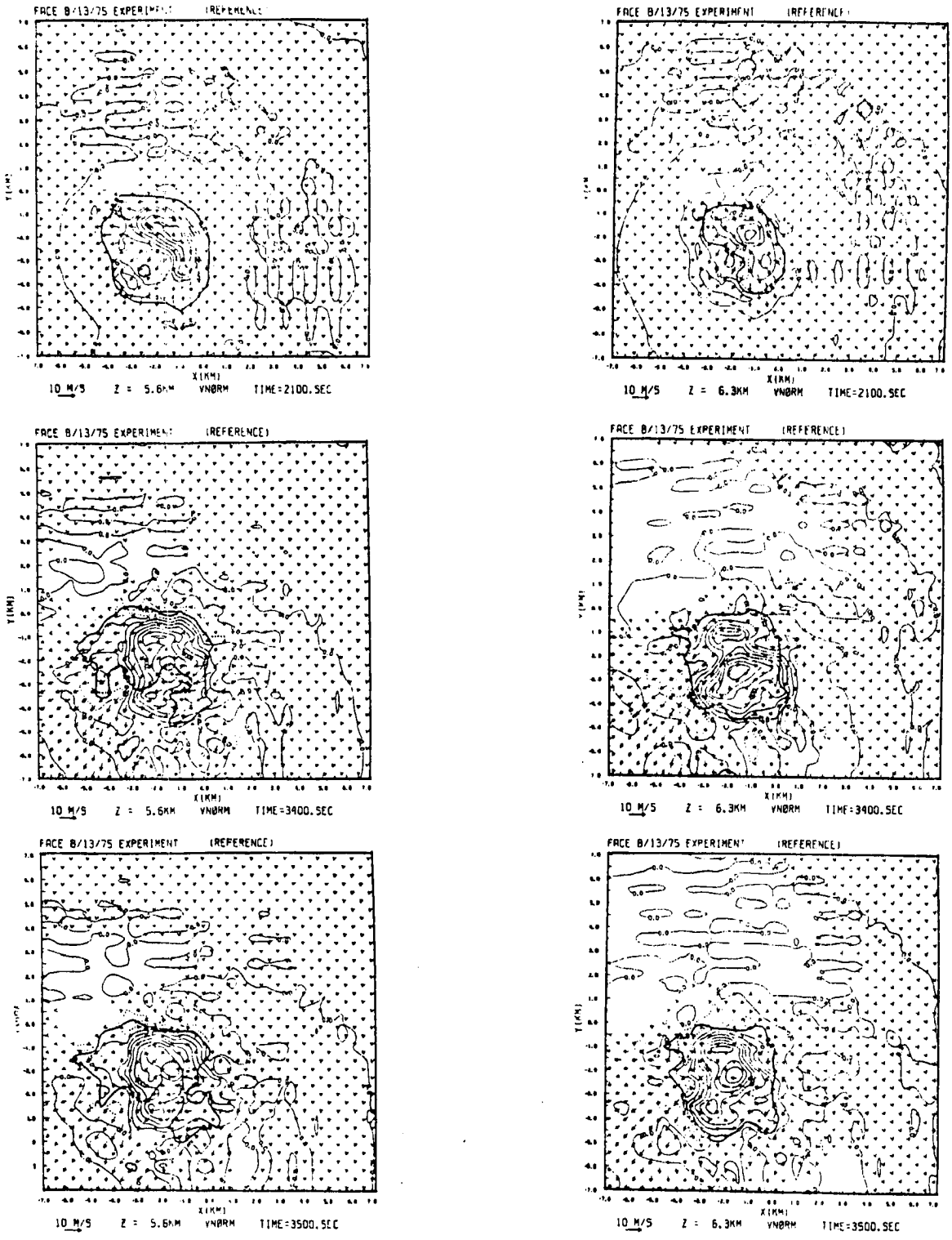

Fig. 5.36: Up and down draft structure for 8.13.75 storm at levels Z = 5.6 km and Z = 6.3 km. Contours as in Fig. 5.13.

procedure indicates that the local sounding is actually being built up by earlier phases of convection of fair weather cumuli that act to moisten and bring the air closer to saturation. It was occasionally observed (Cunning, personal communication), that at preferred locations and times during FACE a system grew explosively following phases of weak non-precipitating convection.

5.4.2 Experiment C-2S: The seeded run

Though cloud C-1R grew to a cumulunimbus cloud seeding was performed between 2000 - 2700 s in order to look at the communication mechanisms and reinforce results of previous experiments.

The seeding resulted in a pulse of temperature, vertical velocity and kinetic energy enhancement (see Fig. 5.37, 5.38). This pulse was not very strong: the kinetic energy rose by less than 0.5% and the vertical velocity by 1.1 ms^{-1} only. Following that episode, from 2100 s and on, entrainment and evaporation were simulated and actually caused the temperature to drop by 0.1^{o}C on the average (see Fig. 5.38). Depletion of cloud ice water and increase in cloud liquid and vapor water were simulated as is illustrated in Fig. 5.39. The total precipitation, as can be seen in Fig. 5.40, was slightly enhanced at first, but by the end of one hour's simulation the treated cloud yields 23.4% less rain than the untreated one. This could reflect enhanced entrainment and possibly overseeding.

Cloud C-1 showed, in general, a strong negative response to seeding. It was, however, a cloud that would not have been classified as a seedable one.

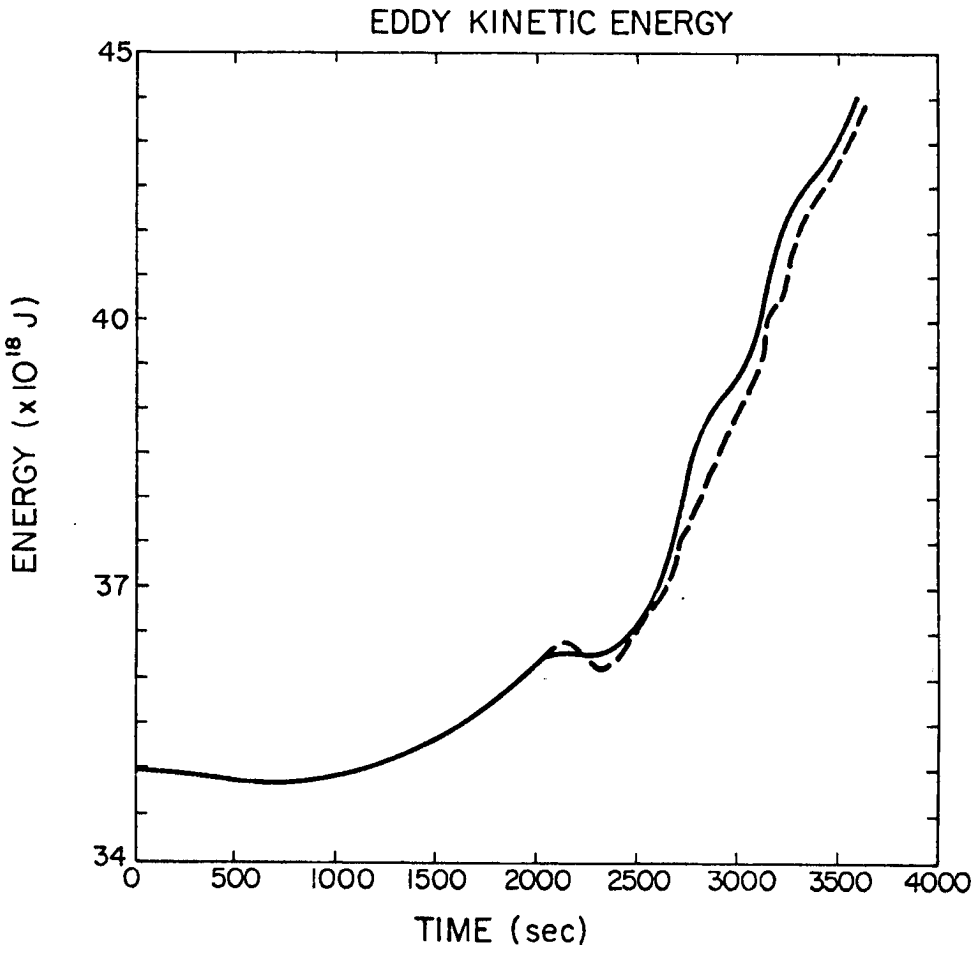

Figure 5.37: Eddy kinetic energy for set C: Solid line C-1R. Dashed line C-1S (seeded).

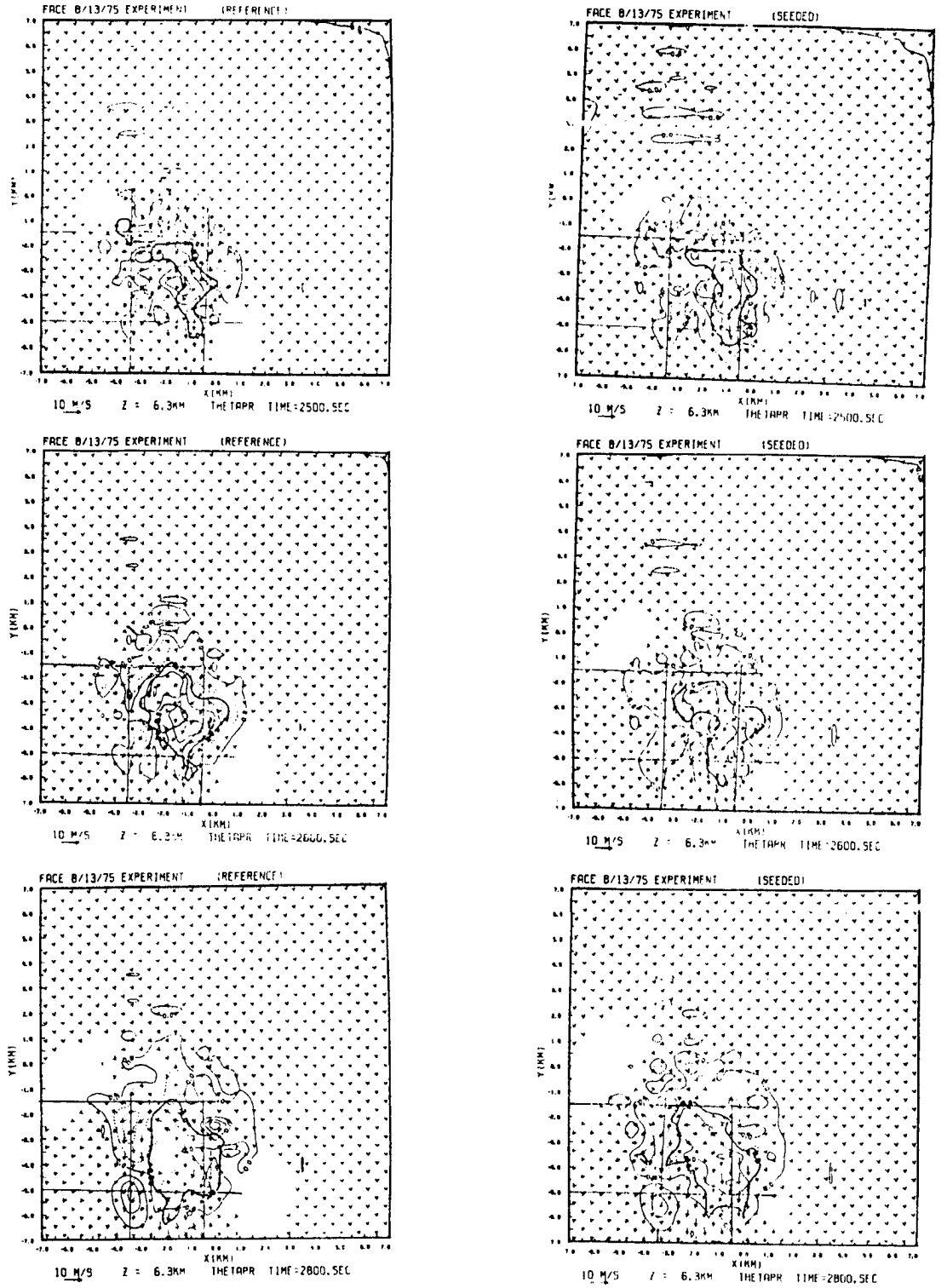

Fig. 5.38: Temperature perturbation field of C-1R vs. C-1S at 2500 sec, 2600 sec, and 2800 sec. The seeded area is in the inner square. Contours as in Fig. 5.21.

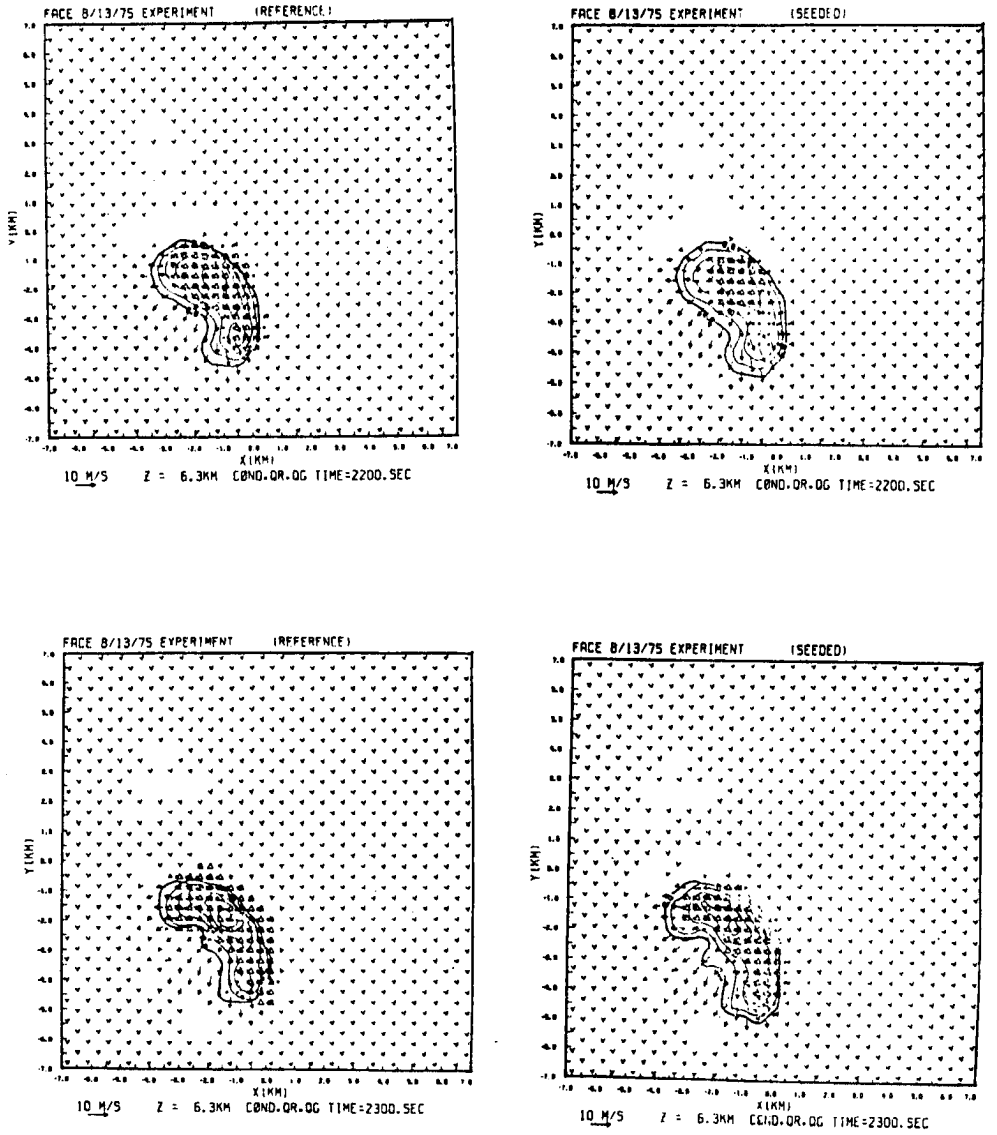

Fig. 5.39: Liquid and graupel water at Z = 6.3 km for C-1R vs. C-1S In the seeded case (C-1S) mixing ratios are actually lower and evaporation took place following seeding.

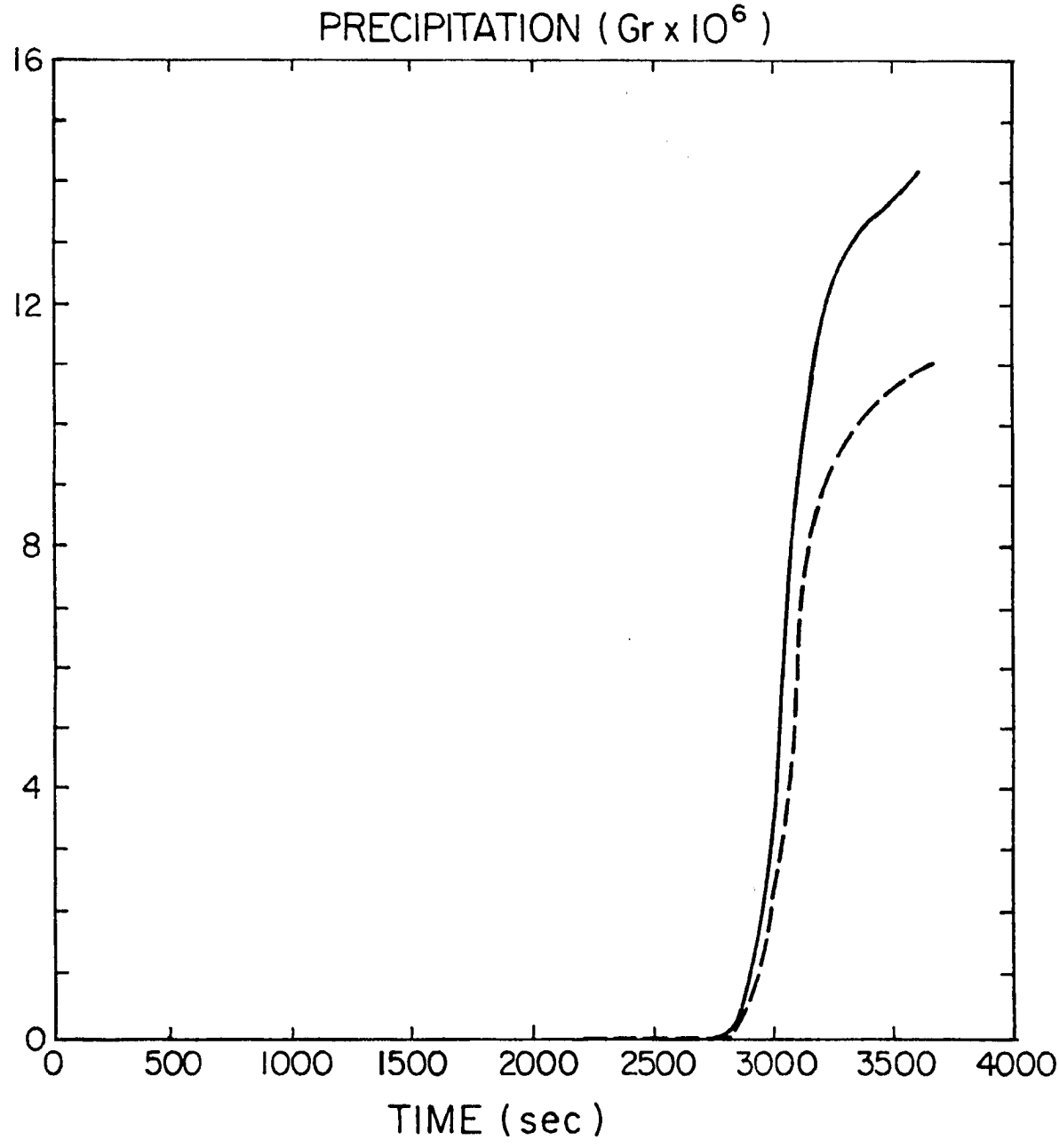

Figure 5.40: Total precipitation from set C at the end of one hour. Solid line C-1 reference; dashed line C-1 seeded.

5.5 Synthesis of Results

All the numerical experiments and the simulated clouds exhibited features in common. Those common features are briefly discussed here. A general vertical distribution of pressure perturbation in the cloud itself with positive perturbations opposing buoyancy near cloud top, and negative perturbations at lower levels, was simulated in all clouds. Local and transitory modifications to this general cloud pressure field were superimposed at times (i.e., when a tower cut off). This cloud pressure field is in agreement with previous estimates and simulations (Barnes, 1970; Schlesinger, 1980; Nehrkorn, 1981; and others).

The subcloud surface layer is more difficult to generalize as it is very sensitive to precipitation falling into it. In all cases there was a positive pressure perturbation right at the precipitation flank. The average subcloud pressure field, however, ranged from meso-highs to mesolows in different cases. Perturbation values of -0.35 mb as measured by Cunning and DeMaria were simulated. However, the contribution of enhanced ice phase processes aloft to those mesolows was small. Seeding was weakly communicated to the surface as a pressure drop. The total precipitation was reduced by seeding due to enhanced entrainment and possible over seeding reaction. Even in the cases where seeding caused more convergence, the excessive moisture was inefficiently processed. Exceptions to that were the cases in which radical changes in the ice phase were introduced (B-1R vs. B-1NI and the exaggerated seeding experiment). In those cases the introduction of ice phase to a system that had no or very little ice resulted in a very large change in precipitation.

In most cases mean temperature increases of 0.5°C to 1.0°C were simulated at the seeding volume due to seeding. The enhanced entrainment was manifested as temperature drops of 0.1°C to 0.3°C below the seeding level. The temperature buoyancy reflected on the updrafts, intensifying them by 0.4 - 2.5 ms^{-1} at the seeding level. The entrainment intensified downdrafts by 1.4 - 2.0 ms^{-1}. Intensification that was cummunicated to the near surface downdrafts weakly (0.1 ms^{-1} at the most). A water phase change from water to ice was simulated after seeding in all seeded cases.

6.0 SUMMARY AND CONCLUSIONS

Based on all the numerical experiments, several conclusions can be drawn. In order to try and generalize the conclusions a scale analysis of the vertical equation of motion is done.

6.1 Scale Analysis of the Vertical Equation of Motion

Consider the vertical equation of motion 2.1 neglecting the coriolis force and the vertical component of friction with the relations 2.2 - 2.7 substituted in

$$\frac{dw}{dt} = -\frac{1}{\rho_o}\frac{\partial p'}{\partial z} + g\left(\frac{\theta'}{\theta_o} + .61\, r_v' - \frac{1}{\gamma}\frac{p'}{p_o}\right) - g r_\ell \qquad (6.1)$$

where primed quantities are perturbation values and $\frac{d}{dt} = \frac{\partial}{\partial t} + V_i \frac{\partial}{\partial x_i}$ is the substantial derivative.

Separate the individual derivative into its local components (in two dimensions) and rearrange:

$$\underset{(1)}{\frac{\partial w}{\partial t}} = \underset{(2)}{-U\frac{\partial w}{\partial x}} \underset{(3)}{- W\frac{\partial w}{\partial z}} \underset{(4)}{- \frac{1}{\rho_o}\frac{\partial p'}{\partial z}} + \underset{(5)\ (6)\ (7)}{g\left(\frac{\theta'}{\theta_o} + .61\, r_v' - \frac{1}{\gamma}\frac{p'}{p_o}\right)} \underset{(8)}{- g r_\ell} \qquad (6.2)$$

terms (2) and (3) are called the horizontal and vertical dynamic parts, term (4) is the hydrostatic part, terms (5), (6), and (7) are the temperature, water vapor and pressure buoyancy parts (which are also hydrostatic) and term (8) is the drag or loading part. Note that the pressure buoyancy and the loading effect act opposite to the thermal and vapor buoyancies.

The following scales will be used in the analysis and are taken directly from the model simulations as typical values:

ρ_o - density of dry air ~ 10^{-3} g cm^{-3}

T - time scale = $\frac{L}{u}$ ~ 10^2 s

p' - pressure perturbation ~ 1 mb = 10^3 dyne cm^{-2}

L - horizontal length scale ~ 10^5 cm (scale on which seeding is done)

H - vertical length scale ~ 10^6 cm

U - horizontal wind speed ~ 10^3 cm s^{-1}

W - vertical wind speed ~ 10^3 cm s^{-1}

g - gravity ~ 10^3 cm s^{-2}

$\frac{\theta'}{\theta_o}$ - thermal buoyancy ~ 10^{-2}

r_v' - vapor mixing ratio ~ 10^{-2}

r_ℓ - liquid water mixing ratio ~ 10^{-2}

$\frac{1}{\gamma}\frac{p'}{p_o}$ - pressure boyancy ~ 10^{-3} ($\gamma = \frac{c_p}{c_v} = 1.4$ is neglected)

The above values are substituted into (6.2) to yield orders of magnitude of the forces as shown in Table 8.

Table 8: Scale analysis of the vertical equation of motion.

(1)	(2)	(3)	(4)	(5)	(6)	(7)	(8)
$\frac{UW}{L}$	$\frac{UW}{L}$	$\frac{W^2}{H}$	$\frac{p'}{\rho_o H}$	$\frac{g\,\theta'}{\theta_o}$	$g\ .61\ q_v'$	$g\frac{p'}{p_o}$	gq_ℓ
10^1	10^1	10^0	10^0	10^1	10^1	10^0	10^1

It can be seen that to 10% accuracy the dominant terms are the vertical

acceleration the horizontal dynamic part, the thermal and vapor buoyancies and the drag term. The non-buoyant hydrostatic part, the pressure buoyancy and the vertical dynamic parts are an order of magnitude smaller. If the horizontal length scale was ~ 10 km instead of ~ 1 km the only terms effected would be (1) and (2), and approximate equilibrium between thermal and vapor buoyancy and the drag force would prevail while the acceleration the dynamic and hydrostatic terms as well as the pressure buoyancy would be smaller. In shallow convection when H becomes smaller, the hydrostatic part becomes compatible to the buoyancy parts, and the dynamic parts are small.

An alternative way of showing the above is by combining 6.1 with the horizontal equation of motion (neglecting the coriolis, viscous and turbulent terms)

$$\frac{du}{dt} = -\frac{1}{\rho_o}\frac{\partial p'}{\partial x} \tag{6.3}$$

differentiating (6.1) with respect to x and (6.3) with respect to z and combining with the two dimensional anelastic continuity equation:

$$\frac{\partial \rho_o u}{\partial x} + \frac{\partial \rho_o w}{\partial z} = 0 \tag{6.4}$$

to yield a diagnostic equation in p':

$$\underset{(a)}{\frac{\partial^2 p'}{\partial x^2}} + \underset{(b)}{\frac{\partial^2 p'}{\partial z^2}} = \underset{(c)}{\rho_o \frac{\partial}{\partial x}(\bar{V}\cdot\nabla U)} + \underset{(d)}{\rho_o \frac{\partial}{\partial z}(\bar{V}\cdot\nabla W)} + \tag{6.5}$$

$$+ \underset{(e)}{\rho_o g \frac{\partial}{\partial z}\left(\frac{\theta'}{\theta_o} + .61\, {}_v - \frac{1}{\gamma}\frac{p'}{p_o}\right)} - \underset{(f)}{\rho_o g \frac{\partial}{\partial z}\, \ell} \qquad \underset{(g)}{} \qquad \underset{(h)}{}$$

in a way similar to Wilhelmson and Ogura (1972).

The advantage of (6.5) is that p' can be diagnosed in its dynamic, buoyant and drag components separately by solving the elliptic equation. Scaling arguments and results remain the same as can be seen in Table 9.

Table 9: Scale analysis of the pressure perturbation diagnostic equation.

a	b	c	d	e	f	g	h
$\frac{p'}{L^2}$	$\frac{p'}{H^2}$	$\rho_o \frac{U^2}{L^2}$	$\rho_o \frac{UW}{HL}$	$\rho_o g \frac{1}{H} \frac{\theta'}{\theta_o}$	$\rho_o g \frac{q_v}{H}$	$\rho_o g \frac{p'}{Hp_o}$	$\rho_o g \frac{q_\ell}{H}$
10^{-7}	10^{-9}	10^{-8}	10^{-9}	10^{-8}	10^{-8}	10^{-9}	10^{-8}

6.2 Summary and Conclusions

The numerical experiments that were performed focused on the communication mechanisms between cumulus clouds and their subcloud layer, on their dynamic response to seeding, mesoscale flow and moisture modifications and increased loading.

Based on the experiments and the foregoing scaling analysis several conclusions can be drawn. In drawing conclusions deficiencies and limitations of the model and the observations must be accounted for. Most simulated clouds were very vigorous due to the difficulty in introducing a perturbation which is strong enough to start a cloud and yet keep it from explosive growth. The procedure is to form a cloud by perturbing the sounding. The ideal cloud is a cloud that grows to the seeding level, but does not grow any farther. It has, therefore, a lot of supercooled water without much ice. The seeding of such a cloud causes rapid glaciation. The simulated clouds may have been, therefore

naturally seeded, and the effect gained by their seeding was actually the effect of overseeding. For that reason, B-1NI was simulated without ice and the modifications in CCN concentrations were done. The simulated microphysical reaction of the high CCN clouds to seeding does not simulate aggregation, which in the right temperature range can rapidly form precipitation size particles from ice crystals. The lack of such a process eliminates the possibility of rain forming from cloud ice in short time scales. In the presence of supercooled rain droplets this process is negligible, but in the absence of raindrops it can be a major precipitation formation mechanism. In the case of seeded clouds the high concentration of crystals may rapidly aggregate to form graupel. Without such a process some water is evaporated out the tops of clouds as nonprecipitating ice, thereby lowering precipitation efficiency. The exaggerated seeding experiments B-1NI, B-2R and B-3S exhibited very strong microphysical response in enhancing precipitation and showed the importance of the ice phase for the production of precipitation. The over-sensitivity of the model to microphysics raises some doubts in the reliability of the ice microphysical predictions. The ice parameterization assumes some arbitrary constants and distributions that are not checked against experimental measurements and yet the model's microphysical scheme is very sensitive to changes in them. The warm rain is parameterized by activating cloud base CCN without allowing activation of CCN at higher levels and without modeling CCN sources and sinks (such as mixing, scavaging, etc.).

There is a principle difference between the way seeding is performed in the actual experiments and the way it was simulated. In the real world, pyrotechnics are released in actively growing towers affecting

a specific part of the tower. This corresponds to a limited area or point seeding. In the model ice crystals were assumed to seed the whole tower's area. Moreover in a multiple cloud environment, the enhanced entrainment can entrain cloudy air or moistened air, whereas it always entrained dry environmental air in the numerical experiments. For the above mentioned reason the concluding remarks focus mainly on the dynamic response and communication mechanisms.

The east flow clouds represent cases of cumuli forming east to the sea breeze convergence line. This location helps maintain a longer living efficient storm. Practical modification of the mesoscale single storm environment, which, no doubt, would enhance rainfall and intensify storm circulation in a beneficial way, is nonetheless not feasible. In general, the lack of local meso- and convective scale data and the poor quality of some of the measurements make it very difficult to initiate and simulate the real observed clouds. Clouds are very sensitive to initial conditions such as the amount and vertical distribution of convergence and the cloud-scale structure of that convergence. The initial circulation and sounding at the local site are not well known, nor is it likely that they would be better resolved in the future. The initialization of C-1 showed that even the field observation site soundings is not very well representative of the exact conditions. Matching of such soundings with upper level available Miami sounding on the convective scale, as is often done in a very crude approximation. The resemblance of cloud C-1 to the observed cloud tends to convince one that the speculated conditions really existed at the time. It is possible, however, that other conditions not depicted by the network (e.g., a weak meso front) would have produced a similar storm.

Bearing in mind all the above reservations, communication mechanisms and other physical processes can be studied from the results. Some results and conclusions are limited to specific clouds and conditions in South Florida. Others reinforced by theoretical consideration and observations are more conclusive. It is important to mention that though the values used for scaling are quoted from the model results, the values are widely accepted as representing deep convection.

The following conclusions are therefore made:

1. The cloud pressure field is in agreement with previous estimates. A general distribution of pressure perturbations with positive perturbations opposing buoyancy near cloud top and low pressure at low levels is evident in all cases. The subcloud pressure field is sensitive to rain falling into it. This is communicated down mainly through the thermodynamic (evaporative), moisture and drag mechanisms (terms (5), (6), (8) and (e), (f), (h) in equations (6.2) and (6.5) respectively). At any level these effects contributed mainly to the horizontal pressure gradients. The vertical communication mechanism by pressure can be divided into hydrostatic (term 4 in 6.2) and pressure buoyancy (terms (7) or (g) in 6.2 and 6.5) parts—both much smaller than all other communication mechanisms at the mature stage of the convection. Those pressure mechanisms exist, nonetheless, and are simulated. In one case the filling of a weak low was even associated with convergence enhancement of 2×10^{-4} s^{-1} at the 900 m level. Part 3 in the dynamic

seeding hypothesis (Table 2) is then weaker than suggested by Cunning and DeMaria (1981).

2. The loading effect is an important vertical communication mechanism. It is acting to reduce updraft velocities by 35% and invigorate downdrafts by 50%. It confined vertical cloud growth by 4.5 km in the high CCN case. Most liquid water stays below the freezing level and hence no practical gain in enhancing buoyancy is achieved by CCN seeding.
3. The downdrafts are indeed invigorated by entrainment due to seeding (parts 3 and 4 in Table 2). This invigoration is communicated mainly through the horizontal dynamic force (term 2 in Eq. 6.2). It is therefore communicating mainly in the horizontal. The way it can communicate to the surface is via term d in Eq. 6.5—a term much smaller than the other terms. Indeed, downdrafts near the surface intensified due to seeding by 0.1 ms^{-1} at the most. A downdraft, though negatively buoyant, can still converge with the ambient flow and force air up (Fig. 5.35). Therefore in a deep moist boundary layer and a favorably organized system, invigorated downdrafts could still converge above the ground with other downdrafts or with ambient flow, and provided the level is moist enough, cause moisture convergence and maybe even merger of clouds. Identifying and seeding such a system in a beneficial way would be extremely difficult.
4. The thermal and vapor buoyancies (terms 5 and 6 in Eq. 6.2) are both major communication mechanisms to the boundary layer and results in acceleration of updrafts. Their con-

tribution to the perturbation pressure field is mainly on the horizontal (term a in Eq. 6.5). Realistic temperature increases of $0.5^{o}C$ - $1^{o}C$ due to seeding were simulated.

5. Three forms of entrainment were simulated: Top entrainment, lateral entrainment of return higher level air (intrusive), and lateral entrainment of environmental air (dynamic). Compensation for buoyancy enhancement is principly dynamic and horizontal acting to entrain more dry air. Even when more moisture converged into the clouds the clouds failed to process it into precipitation.

6. Precipitation can act both to inhibit or to enhance cloud development depending on the orientation of the precipitation flank with respect to the inflow. Modification of the mesoscale flow can alter significantly a single storm's circulation. Modification and seeding of a single cloud, on the other hand, had almost no influence on the mesoscale. The precipitation acts on the horizontal pressure field through evaporational cooling, causing negative buoyancy and high pressure. As the vertical pressure and downdraft communication mechanisms are weak and transitory, the precipitation is postulated as the main vertical cummunication mechanism, a mechanism that can influence both the subcloud pressure and the subcloud thermodynamic fields. Efforts to modify a cloud system's dynamics should be therefore aimed at increasing the rainfall from that system.

7. The dynamically seeded clouds reacted to seeding by decreasing precipitation due to entrainment and possibly static over-

seeding effects. As mentioned above, there is a major difference between the way clouds are actually seeded and the way seeding was simulated.

8. One dimensional predictions of seedability were not confirmed by the three dimensional simulations. The seedability predicted by the one dimensional model was for a narrow range of marginal clouds. The three dimensional model failed to simulate those marginal clouds.

The results of this study must be considered inconclusive as far as whether dynamic seeding of individual clouds increases or decreases surface rainfall. While the model predicted that dynamic seeding of individual clouds decreases rainfall this result cloud have been affected by the following:

i) significant dynamic seedability was never predicted by the model

ii) the enhancement of dynamic entrainment as a consequence of seeding could have been a result of the method of simulating seeding or a consequences of the model's inability to resolve smaller-scale mixing processes adquately

iii) the lack of an ice aggregation model could favor microphysical overseeding of the clouds.

6.3 Recommendations for Further Research

There are a number of areas into which this research could be extended. Run B-1 could be further modified by repeating it with latent heat of freezing set to be zero. This would help separate the dynamic from the microphysical effects, telling how much of the precipitation results from latent heat induced convergence.

To explore the potential of dynamic seeding in multicell systems, simulation of such systems is recommended. This would shed light on the interactions of downdrafts from different cells. It would be of interest to simulate limited cloud area seeding in order to reduce the drying of the seeded area by enhanced lateral entrainment. In addition, attempts to simulate a marginal cloud with the model can be continued. Such a cloud may be produced by turbulent eddies in a weakly buoyant atmosphere rather than by imposing a cloud-scale vertical velocity perturbation. Finally, some modifications and improvements could be applied to the model. An aggregation model could be important in some clouds and conditions and modeling the CCN evolution could result in a model with better microphysical predictions. An attempt to adjust arbitrary constants in the microphysical schemes to actual measured ones should be done. Initialization scheme allowing to initialize the model with two different soundings at two different parts of the simulated domain would make it possible to simulate systems along a front. Higher grid resolution and/or improved turbulence parameterization would better simulate subcloud features not resolved by the current model version. Having better measurements, denser mesonets and finer resolution in data would clear many uncertainties in initialization procedures and could pave the way to give modeling of that scale a predicative ability.

REFERENCES

Barnes, S.L., 1978a: Oklahoma thunderstorms on 29-30 April 1970. Part I: Morphology of a tornadic storm. Mon. Wea. Rev., 106, 673-684.

Barnes, S.L., 1978b: Oklahoma thunderstorms on 29-30 April 1970. Part II: Radar observed merger of twin hook echoes. Mon. Wea. Rev., 106, 685-696.

Barnes, S.L., 1970: Some aspects of a severe, right-moving thunderstorm deduced from mesonetwork rawinsonde observations. J. Atmos. Sci., 27, 634-648.

Betts, A.K., 1978: Convection in the tropics. Meterology Over the Tropical Oceans. Bracknell, England. Roy. Met. Soc., 105-132.

Braham, R.R., Jr., L.J. Battan and H.R. Byers, 1957: Artificial nucleation of cumulus clouds, Chapter IV in Meteor. Monogr., 2, No. 11, 47-85.

Brandes, E.A., 1977: Flow in severe thunderstorms observed by dual-Doppler radar. Mon. Wea. Rev., 105, 113-120.

Browning, K.A., 1964: Airflow and precipitation trajectories within severe local storms which travel to the right of the winds. J. Atmos. Sci., 21, 634-639.

Browning, K.A., and F.H. Ludlam, 1962: Airflow in convective storms. Quart. J. Roy. Meteor. Soc., 88, 117-135.

Byers, H.R. General Meteorology. 4th ed. New York, McGraw-Hill, 1974. Chapter 16.

Chen, J.M., 1981: A numerical study of cloud seeding effects, latent heat of fusion effects, and condensate loading effects on cloud dynamics and precipitation evolution. M.S. Thesis in Meteorology, South Dakota School of Mines and Technology, Rapid City, South Dakota.

Clark, T., 1979: Numerical simulations with a three-dimensional cloud model: Lateral boundary condition experiments and multicellular severe storm simulations. J. Atmos. Sci., 36, 2191-2215.

Cotton, W.R., and G. Tripoli, 1978: Cumulus convection in shear flow - three-dimensional numerical experiments. J. Atmos. Sci., 35, 1503-1521.

Cotton, W.R., M.S. Stephens, T. Nehrkorn, and G.J. Tripoli, 1982: The Colorado State University cloud/mesoscale model - 1982. Part II - An ice phase parameterization. Submitted for publication to J. de Rech. Atmos.

Cunning, J.B., and M. DeMaria, 1981: Comment on 'Downdrafts as linkages in dynamic cumulus seeding effects'. J. Appl. Meteor., 20, 1081-1088.

Cunning, J.B., R.I. Sax, R.L. Holle and H. Poor, 1979: Morphology of seed clouds as determined from triple-Doppler radar - A case study. Preprints: 7th Conf. on Inadvertent and Planned Weather Modification, Amer. Meteor. Soc., Boston, 142-143.

Das, P., 1964: Role of condensed water in the life cycle of a convective cloud. J. Atmos. Soc., 21, 404-418.

Dennis, A.S., J.R. Miller, E.I. Boyd, and D.E. Chan. Effects of cloud seeding on summertime precipitation in North Dakota, 1975. Final report. South Dakota School of Mines and Technology, Rapid City, South Dakota.

Dutton, J.A., and G.H. Fichtle, 1969: Approximate equations of motion for gases and liquids. J. Atmos. Sci., 26, 241-254.

Foote, G.B., and J.C. Fankhauser, 1973: Airflow and moisture budget beneath a northeast Colorado hailstorm. J. Appl. Meteor., 12, 1330-1353.

Fritsch, J.H., and C.F. Chappell, 1979: Three-dimensional numerical simulations of seeded and unseeded convective cloud complexes. Preprints 7th Conf. on Inadvertent and Planned Weather Modification, Amer. Meteor. Soc., Boston.

Gagin, A. and J. Neumann, 1974: Rain stimulation and cloud physics in Israel. Chapter 13 in Weather and Climate Modification, Edited by W.N. Hess, John Wiley and Sons, New York, 454-494.

Grant, L.O. and A.M. Kahan, 1974: Weather Modification for augmenting orographic precipitation. In Hess, W.D. (Editor), Weather Modification, Wiley, NY, 282-317.

Holton, J.R. An Introduction to Dynamic Meteorology, Chapter 2, Academic Press, 1972, 319 pp.

Houze, J.R., Jr., 1973: A climatological study of vertical transport by cumulus scale convection. J. Atmos. Sci., 33, 424-429.

Hsie, Eirh-Yu, 1978: Numerical simulation of ice-phase convective cloud seeding. M.S. Thesis, S.D. School of Mines and Technology, Rapid City, SD.

Klemp, J.B., and R.B. Wilhelmson, 1978: The simulation of three-dimensional convective storm dynamics. J. Atmos. Sci., 35, 1070-1096.

Koenig, L.R., and F.W. Murray, 1976: Ice-bearing cumulus cloud evolution: Numerical simulation and general comparison against observations. J. Appl. Meteor., 15, 747-762.

Kopp, F.J., E.-Y. Hsie, R.D. Farley, J.H. Hirsch, and H.D. Orville, 1979: Cloud seeding simulations. Preprints 7th Conf. on Inadvertent and Planned Weather Modification, A.M.S., Boston.

Kropfli, R.A., and L.J. Miller, 1976: Kinematic structure and flux quantities in a convective storm from dual-Doppler radar observations. J. Atmos. Sci., 33, 520-529.

Kurihara, Y., and J.L. Holloway, Jr., 1964: Numerical integration on a nine-level global primitive equations' model formulated by the box method. Mon. Wea. Rev., 95, 509-530.

Lemon, L.R., 1976: The flanking line, a severe thunderstorm intensification source. J. Atmos. Sci., 33, 686-694.

Levine, J., 1959: Spherical vortex theory of bubble-like motion in cumulus clouds. J. Meteor., 16, 653-662.

Malkus, J.S. Cumulus Dynamics. "Penetrative convection and an application to hurricane cumulonimbus towers." C.F. Anderson, Editor, New York, Pergamon, pp. 65-84.

Manton, M.J., and W.R. Cotton, 1977: Formulation of approximate equations for moist deep convection on the mesoscale. Atmos. Sci. Paper No. 26, Colorado State University, Fort Collins, CO.

Marwitz, J.D., R.E. Steward, T.S. Karacostas, and B.E. Martner, 1979. Cloud Physics Studies in SCPP During 1978-79. Report No. AS 123, U. of Wyoming, Laramie, WY.

Murray, F.W. and L. R. Koenig, 1972: Numerical experiments on the relation between microphysics and dynamics in cumulus convection. Mon. Wea. Rev., 100, 717-732.

Miller, M.J., 1978: The Hampstead storm: A numerical simulation of a quasi-stationary cumulonimbus system. Quart. J. Roy. Meteor. Soc., 104, 413-427.

Nehrkorn, Thomas, 1981: A three-dimensional simulation of the dynamic response of a Florida cumulus to seeding. M.S. thesis, Colorado State University, Dept. of Atmospheric Science, Fort Collins, Colorado, 99 pp.

Orlanski, I., 1976: A simple boundary condition for unbounded hyperbolic flow. J. Comp. Phys., 21, 251-269.

Parungo, F., and C. Hagamoto, 1982: Case studies of hydrometeors in Florida cumuli. NOAA Tech. Memorandum, ERL OWRM-16.

Sax, R.I., and J.G. Hudson, 1981: Continentality of the South Florida summertime CCN aerosol. J. Atmos. Sci., 38, 1467-1479.

Schlesinger, R.E., 1980: A three-dimensional model of an isolated thunderstorm. Part II: Dynamics of updraft splitting and mesovortex couplet evolution. J. Atmos. Sci., 37, 395-420.

Simpson, J., 1980: Downdrafts as linkages in dynamic cumulus seeding effects. J. Appl. Meteor., 19, 477-487.

Simpson, J., and V. Wiggert, 1969: Models of precipitating cumulus towers. Mon. Wea. Rev., 97, 471-489.

Simpson, J., and H.J. Cooper, 1981: Reply to Cunning and DeMaria: "Comment on 'Downdrafts as linkages in dynamic cumulus seeding effects'". J. Atmos. Sci., 20, 1089-1091.

Simpson, J., R.H. Simpson, D.A. Andrews, and M.A. Eaton, 1965: Experimental cumulus dynamics. Rev. Geophys., 3, 387-431.

Srivastava, R.C., 1967: A study on the effects of precipitation on cumulus dynamics. J. Atmos. Sci., 24, 36-45.

Stephens, M.A., 1979: A simple ice phase parameterization. M.S. Thesis, Atmos. Sci. Paper No. 319, Dept. of Atmos. Sci., Colorado State Univ., Fort Collins, CO.

Takahashi, T., 1981: Warm rain development in a 3-D cloud model. J. Atmos. Sci., 38, 1991-2013.

Takeda, T., 1965: The downdraft in convective shower cloud under the vertical shear and its significance for the maintenance of convective system. J. Meteor. Soc. of Japan, 43, 302-309.

Takeda, T., 1966a: The downdraft in convective cloud and raindrops: A numerical computation. J. Meteor. Soc. of Japan, 41, 1-11.

Takeda, T., 1966b: Effects of the prevailing wind with vertical shear on the convection accompanied with heavy rainfall. J. Meteor. Soc. of Japan, 44, 129-144.

Tripoli, G.J., and W.R. Cotton, 1980: A numerical investigation of several factors contributing to the observed variable intensity of deep convection over South Florida. J. Appl. Meteor., 19, 1037-1063.

Tripoli, G.J. and W.R. Cotton, 1982: The Colorado State University three-dimensional cloud/mesoscale model - 1982. Submitted for publication to J. de Rech. Atmos.

Weinstein, A.T. and L.G. Davis, 1968: A parameterized numerical model of cumulus convection. Rept. II, National Science Foundation GA-777, 43, Nat. Sci. Found., Washington, D.C.

Wilhelmson, R.B. and Y. Ogura, 1972: The pressure perturbation and numerical modeling of a cloud. J. Atmos. Sci., 29, 1295-1307.

Woodley, W.L. and R.I. Sax, 1976: The Florida area cumulus experiment: rationale, design, procedures, results, and future course. NOAA Technical Report, ERL 354-WMPO 6, 204 pp.

Zipser, E.J., 1969: The role of roganized unsaturated convective downdrafts in the structure and decay of an equatorial disturbance. J. Appl. Meteor., 8, 799-814.

Yau, M.K., 1980: The effects of evaporation water load and wind shear on cloud development in a 3-D numerical model. J. Atmos. Sci., 37, 488-494.

Yau, M.K., 1980: A two-cylinder model of cumulus cells and its application in computing cumulus transports. J. Atmos. Sci., 37, 2470-2485.

Yau, M.K., and M. Rejéan, 1982: Numerical simulation of a cumulus ensemble in three dimensions. To be published in J. Atmos. Sci.

APPENDIX: The Model Equations

The model is described in full detail by Tripoli and Cotton (1982, Part I) and Cotton, Stephens, Nehrkorn and Tripoli (1982, Part II). A brief summary of the equation is presented in this appendix.

A.1 The Coordinate System

To account for irregular terrain, a terrain following, sigma z' vertical coordinate is employed. The transformed coordinates are defined:

$$x^* = x$$

$$y^* = y$$

$$z^* = \frac{z - z_s}{H - z_s} H$$

where quantities with an asterisk represent the transformed coordinates and those without an asterisk are cartesian coordinates. The surface height above some reference level, usually taken to be sea level is given by z_s and the height of the model top at which the z* coordinate surface becomes horizontal is given by H. The transformations of derivaties of any given quantity are given in Clark (1977) and Tripoli and Cotton (1982). For Florida cases in this study z_s is taken to be identically zero and the transformed coordinate system is identitical to the cartesian one.

A.2 The Set of Equations

Following Dutton and Fichtl (1969), Cotton and Tripoli (1978) and Tripoli and Cotton (1982) any variable A may be decomposed as

$$A(x,y,z,t) = \overline{A}(x,y,z,t) + A''(x,y,z,t) = A_o(z) + \overline{A}'(x,y,z,t) + A''(x,y,z,t)$$

where the overbar represents an average over a time and space scale resolvable by the numerical model and double primes represent the deviations from that average. The subscript "o" refers to an arbitrary horizontally homogeneous reference state and the single primed quantity with an overbar is an average deviation over some volume from that reference state. It is assumed that this deviation is small compared to the reference state value when applied to dry air density, pressure and temperature estimates. The double primed quantity represents the turbulence deviation from the average. On velocity, θ_{il} and mixing ratio quantities, the basic state and average deviations are not routinely separated. The reference state is assumed to be dry and to obey the ideal gas low given by

$$p_o = \rho_o R T_o \tag{A1}$$

where p_o, ρ_o and T_o are the basic state pressure density and temperature. The basic state is also hydrostatic obeying the relation

$$\frac{\partial p_o}{\partial z} = -\rho_o g \tag{A2}$$

combining the gas low for dry air and vapor, Dalton's law of partial pressure and Poisson's equation, expanding the gas low about the dry

reference state, taking logrithms, expanding on a series approximation and neglecting higher order terms yield the linearized gas equation

$$\frac{1}{\gamma}\,\frac{\overline{p'}}{p_o} = \frac{\overline{\rho'_a}}{\rho_o} + \frac{\overline{\theta'}}{\theta_o} + 1.61\,\overline{r_r} \tag{A3}$$

where $\gamma = \frac{cp}{cv}$

the total mass density is given by

$$\rho = \rho_a + r_T\,\rho_a \tag{A4}$$

where r_T is the total mixing ratio of water substance and subscript "a" refers to dry air.

The equation of motion using the tensor notation are given by

$$\frac{\partial(\rho_o \overline{U}_i)}{\partial t} + \frac{\partial \overline{p'}}{\partial x_i} + \rho'_a\, g\, \delta_{i3} = \rho_o\, \mathrm{ADV}\,(\overline{U}_i) + \rho_o\, \mathrm{TURB}\,(\overline{U}_i) \tag{A5}$$

$$- \overline{r}_T\, g\, \delta_{i3} + \varepsilon_{ijk}\, f_j\, \overline{U}'_k$$

where ADV is an advective operator and TURB is a turbulence operator. δ_{i3} is the Kronecker delta function and ε_{ijk} is the permutation symbol (or Levi-Civita density). The coriolis parameter is affected only by the perturbation velocity and horizontal variations in p_o due to coriolis effects are neglected.

The fully elastic continuity equation is given by

$$\frac{\partial \overline{\rho'_a}}{\partial t} + \frac{\partial}{\partial x_j}(\rho_o U_j) = 0 \tag{A6}$$

where the momentum divergence has been linearized. This form has been found to be very good approximation to the nonlinear form experi-

mentally and can also be justified by scaling arguments presented by Dutton and Fichtl (1969).

The thermodynamic energy equation using $\theta_{i\ell}$ which is conservative over all water phase changes, and assuming precipitation does not influence θ', can be written:

$$\frac{\partial \theta_{i\ell}}{\partial t} = ADV\ (\overline{\theta}_{i\ell}) + TURB\ (\overline{\theta}_{i\ell}) - \frac{\overline{\theta}''_{i\ell}}{\overline{\theta}} \quad \frac{L_{\ell v} PR_r + L_{iv}(PR_i + PR_g)}{c_p Max(T,\ 253)} \qquad (A7)$$

where $\theta_{i\ell}$ is the ice-liquid potential temperature described by Tripoli and Cotton (1980b) and defined as:

$$\theta_{i\ell} = \theta \left[1 + \frac{L_{\ell v} r_r + L_{iv}(r_i + r_g)}{c_p MAX(T,\ 253)}\right]^{-1} \qquad (A8)$$

The sources and sinks for $\theta_{i\ell}$ are only due to losses or gains in liquid and ice water due to hydrometeor settling.

For any dependent variable A, the advective operator is given by:

$$ADV(\overline{A}) = -\frac{1}{\rho_o} \left[\frac{\partial(\rho_o \overline{U}_j \overline{A})}{\partial x_j} - A \frac{\partial(\rho_o U_j)}{\partial x_j}\right]$$

The turbulent operator is given by:

$$TURB(\overline{A}) = \frac{\partial \overline{A'' U''_j}}{\partial x_j}$$

where the turbulent flux term $\overline{A''U''_j}$ is parameterized using an eddy viscosity closure.

A.3 Microphysics

Total water is divided into vapor (r_v), liquid (r_ℓ) and ice water (r_{ice}). Liquid water is assumed to consist of cloud droplets

having a mixing ratio r_c and raindrops having a mixing ratio r_r. Cloud droplets are assumed to have negligible terminal velocity and evaporate and condense instantaneously maintaining zero supersaturation. The cloud droplet distribution is not specified, yet they are assumed to exist in concentrations which are constant and characteristic of the environment modeled. Raindrops, having a mixing ratio r_r, on the other hand, are much larger and are assumed to exist in a Marshal Palmer distribution with a constant slope.

The mixing ratio of rain droplets is initially converted to raindrops by a parameterization of cloud droplet collection described by Tripoli and Cotton (1980). Once formed, raindrops can accrete cloud droplets, evaporate, precipitate or interact with ice particles. The ice phase is partitioned into ice crystals having mixing ratio $\bar{r}_i$ and graupel having mixing ratio $\bar{r}_g$. Ice crystals are considered pristine individual crystals which are not highly rimed. They are initiated from a specified concentration of activated ice nuclei which are assumed to occur naturally or by seeding. Graupel particles on the other hand, are highly rimed ice crystals that have lost their crystalline identity, or are frozen raindrops. They are much larger and have particle density as high as .9 g cm^{-3}. As graupel mixing ratios increase, the assumed mass of individual graupel particles may reach a large enough size to be considered hail. The ice phase parameterization also provides an average terminal velocity for both ice crystals and graupel. Unlike raindrops, graupel particles are assumed to have a variable particle density and the distribution slope varies. Hence, fall rates change considerably with temperature and ice mixing ratio.

The ice parameterization predicts the changes in ice crystal mixing ratio $\overline{r}_i$ by vapor deposition and riming growth of ice crystals, as well as melting. The parameterization also predicts the changes in graupel mixing ratio $(\overline{r}_g)$ due to vapor deposition, conversion of ice crystal into graupel supercooled raindrops collecting ice crystals and freezing, graupel particles collecting supercooled raindrops, melting of graupel, and precipitation.

The total $\overline{r}_T$ of the cloud is given by:

$$\overline{r}_T = \overline{r}_v + \overline{r}_c + \overline{r}_r + \overline{r}_i + \overline{r}_g = \overline{r}_v + \overline{r}_\ell + \overline{r}_{ice} \tag{A9}$$

where $\overline{r}_\ell = \overline{r}_c + \overline{r}_r$

and $\overline{r}_{ice} = \overline{r}_i + \overline{r}_g$

At temperature warmer than the assumed homogeneous ice nucleation temperature ($T_H = 233.16\ K^o$), zero supersaturation with respect to liquid water is required. As a result cloud water and vapor are uniquely determined from temperature, total water, rain, cloud ice and graupel contents. When the temperature becomes colder than T_H, all cloud water is assumed to be frozen. Hence at the nucleation temperature, all cloud water must freeze, but the air may remain supersaturated with respect to ice. This supersaturation is more slowly removed by the process of vapor deposition. Cloud water and ice are, then, diagnosed from the relations

$$r_c = \begin{cases} \text{MAX}\ (\overline{r}_T - \overline{r}_r - \overline{r}_i^* - \overline{r}_g - \overline{r}_{vs}, 0); & T > T_H \\ 0 & ;\ T \le T_H \end{cases} \tag{A10}$$

$$r_i = \begin{cases} r_i^* & ; \quad T > T_H \\ r_i^* + \text{MAX}\ (\bar{r}_T - \bar{r}_i^* - \bar{r}_g - \bar{r}_{vs},\ 0) & ; \quad T \leq T_H \end{cases} \tag{A11}$$

where $\bar{r}_i^*$ is the predicted value of ice mixing ratio and $\bar{r}_{vs}$ is the saturation vapor mixing ratio with respect to liquid water. The mass continuity equations for time dependent water variables are

$$\frac{\partial \bar{r}_T}{\partial t} = \text{ADV}(\bar{r}_T) + \text{TURB}(\bar{r}_T) - \text{PR}_r - \text{PR}_g - \text{PR}_i \tag{A12}$$

$$\frac{\partial \bar{r}_r}{\partial t} = \text{ADV}(\bar{r}_r) + \text{TURB}(\bar{r}_r) + \text{AC}_{cr} + \text{CN}_{cr} + \text{VD}_{rv} - \text{ML}_{gr} - \text{FR}_{rg} - \text{CL}_{rg} - \text{PR}_r \tag{A13}$$

$$\frac{\partial \bar{r}_i}{\partial t} = \text{ADV}(\bar{r}_i) + \text{TURB}(\bar{r}_i) - \text{ML}_{ic} + \text{VD}_{vi} - \text{CN}_{ig} + \text{RM}_{ci} + \text{NU}_{vi} - \text{PR}_i \tag{A14}$$

$$\frac{\partial \bar{r}_g}{\partial t} = \text{ADV}(\bar{r}_g) + \text{TURB}(\bar{r}_g) - \text{ML}_{gr} + \text{VD}_{gv} + \text{CN}_{ig} + \text{RM}_{cg} + \text{CL}_{rg} + \text{FR}_{rg} - \text{PR}_g \tag{A15}$$

The sources and sinks are defined as AC for accretion, CN for auto-conversion, NU for nucleation, ML for melting, FR for freezing, VD for vapor deposition/evaporation, RM for riming and PR for precipitation. Each term includes a double subscript, where the first subscript is the water phase being depleted and the second is the water phase which is growing. The subscripts v, c, r, i and g refer to vapor, cloud, rain, ice crystal and graupel water respectively. For ecample, AC_{cr} is the accretion of cloud water by rain water. The single subscript

associated with precipitation refers to the phase of water that is being precipitated. The precipitation tendency for rain is given by

$$PR_r = \frac{1}{\rho_o} \frac{\partial(\rho_o \bar{v}_r \bar{r}_r)}{\partial x_3} \tag{A16}$$

where $\bar{v}_r$ is the terminal velocity of rain. Similar relations are used for ice crystals and graupel. The microphysical parameterization are described in detail in Tripoli and Cotton (1980) and Cotton et al. (1982, Part II).

Equations (A3), (A4) and (A8 - A11) with the Poisson equation form a set of diagnostic equations that with the prognostic set (A5 - A7) and (A12 - A15) make up a closed system of equations which can be solved numerically, given proper boundary and initial conditions.